Solitary electron density waves in a magnetized plasma-loaded waveguide

Lynov, Jens-Peter

Publication date:
1980

Document Version
Publisher's PDF, also known as Version of record

Risø-R-432

RISØ

Risø-R-432

Solitary Electron Density Waves in a Magnetized, Plasma-loaded Waveguide

Jens-Peter Lynov

Risø National Laboratory, DK-4000 Roskilde Denmark
August 1980

RISØ-R-432

SOLITARY ELECTRON DENSITY WAVES IN A MAGNETIZED, PLASMA-LOADED WAVEGUIDE

Jens-Peter Lynov

Abstract. Investigations of two different types of nonlinear, solitary electron density waves in a magnetized, plasma-loaded waveguide are presented. One of the wavetypes is a localized, compressional pulse identified as a Trivelpiece-Gould soliton. The modification of this soliton by the resonant electrons is studied theoretically, by direct numerical solution of the model equation, experimentally, and by numerical simulation of the experiment. The other wave is a localized, rarefactive pulse called an electron hole. It is a positive pulse consisting of a large number of trapped electrons and is a purely kinetic phenomenon. A simple waterbag model for the electron hole is derived and compared with the results from the experiment and the numerical simulation. Finally, interactions between the solitary waves are investigated.

UDC 533.951

August 1980
Risø National Laboratory, DK-4000 Roskilde, Denmark

This thesis has been accepted by the Technical University of Denmark in connection with the conferment of the lic.techn. (Ph.D.) degree.

ISBN 87-550-0733-3
ISSN 0106-2840

Risø Repro 1981

CONTENTS

Page

APPENDICES

PREFACE

This report is written in order to meet part of the requirements for obtaining the Danish Ph.D. degree of "teknisk licentiat" (in Latin: licentiatus technices). My post-graduate studies were connected to the Institute of Electrophysics at the Technical University of Denmark and the work was performed during the period from autumn 1977 to summer 1980, while I was attached to the Group of Plasma Physics in the Department of Physics at Risø National Laboratory. During this period, the group consisted of P. Michelsen, H.L. Pécseli, J. Juul Rasmussen and myself. My supervising professor has been P.L. Ølgaard from the Technical University, and as co-supervisors I have had V.O. Jensen and P. Michelsen, both from Risø National Laboratory. My work was financially supported by the Association EURATOM-Risø National Laboratory.

As seen from the references used in the following sections, much of the work presented in this report has been published previously. In some cases, where a previous publication has been very detailed, for example in connection with long theoretical calculations, I will outline only the procedure used and write down the main results. On the other hand, I will give supplementary information on points where the previous papers have been somewhat summary, and I will present some new results obtained after the publication of the papers. In any case, the present report is intended to serve as a self-contained description of the investigations.

1. INTRODUCTION

Although the linear properties of a plasma by no means can be said to be absolutely well understood at present, there has been an increasing interest over the last few decades to begin to investigate fundamental nonlinear plasma behaviour. This growing interest has, partially, been stimulated by fusion-orientated plasma physics, since many basic phenomena in this field, such as anomalous diffusion, anomalous resistivity, and high power plasma heating cannot be described in terms of linear plasma properties. However, the major impetus to study nonlinear phenomena in plasmas may be sought in the development and refinement of theoretical methods and experimental techniques in many different branches of physics, in addition to the appearance of fundamentally new results in pure and applied mathematics and numerical analysis. A famous example (which may serve as a brief, historical background for the present report) of such an impulse from the field of mathematics and numerical analysis to investigations of nonlinear phenomena in plasmas, as well as other physical systems, is the discovery of the so-called "soliton" solutions to the Korteweg-de Vries (KdV) equation by Zabusky and Kruskal (1965).

Late in the nineteenth century, Korteweg and de Vries (1895) derived an equation to describe the evolution of surface waves on shallow water. This KdV equation is the simplest model equation for wave propagation which includes both nonlinear and dispersive effects but ignores dissipation. Korteweg and de Vries showed that their equation possessed localized wave solutions which propagate without any change in shape and velocity. These special solutions were called solitary waves and their remarkable ability to maintain their original form is due to the exact balance of nonlinearity and dispersion. For many years these solitary waves were not considered of great importance, and it was generally believed that if two solitary waves were

to collide, the nonlinear interaction during the collision would completely destroy the identity of the individual wave. Since there excisted no analytical method by which the exact evolution of a nonlinear wave equation could be described in detail, it was not until the appearance of the digital computer that this assumption could be tested by direct calculation.

In 1965 such a numerical computation of the evolution of the KdV equation was performed by Zabusky and Kruskal, and they surprisingly found that two colliding solitary waves, although interacting strongly during the collision, indeed did preserve their identity and emerged from the region of collision regaining their original form. Zabusky and Kruskal gave the name soliton to such a solitary wave which preserves its shape and velocity upon collision with other solitary waves.

These astonishing results immediately triggered a large number of intense investigations of systems which could demonstrate soliton-like behaviour, and gave impulse to a widespread search for other nonlinear equations possessing soliton solutions. An excellent review paper on the birth and the early, rapid development of "soliton physics" was written by Scott, Chu and McLaughlin (1973).

In the field of plasma physics, Ikezi et al. (1970) and Ikezi (1973) observed soliton effects in ion-acoustic wave experiments which can be described by the KdV equation (Washimi and Taniuti, 1966). Later, Ikezi et al. (1971) found that nonlinear, compressional electron pulses in a strongly magnetized, plasma-filled waveguide also are well described as KdV solitons.

The present paper describes the investigations performed at Risø of two different types of solitary electron waves. One of these is the compressional soliton just mentioned, while the other is a positive pulse, indicating a deficit of electrons, which is called an "electron hole".

Since the system under consideration cannot be considered lossless (indeed, a major part of this paper is devoted to a de-

tailed description of the effect of dissipation) it is necessary to relax the definitions of a solitary wave and a soliton given by Scott et al. (1973). In this paper a solitary wave is a localized wave that propagates with an almost fixed velocity and with a shape that is almost unchanged. The nonlinear effects are essential for the wave evolution and the effect of dissipation is to produce only minor, but detectable, changes in the shape and velocity of the wave. A soliton is then a solitary wave which preserves its identity upon collision with other solitary waves. Some authors call such "imperfect" solitons "quasi-solitons". In order to distinguish the physical electron soliton from the idealized KdV soliton it is denoted a Trivelpiece-Gould soliton, referring to the dispersion relation derived by Trivelpiece and Gould (1959) for linear electron waves in a magnetized, plasma-filled waveguide.

This paper is organized in the following way: in Section 2 the experimental set-up is described and the basic experimental observations are presented. Section 3 contains a description of a numerical simulation code, which was constructed in order to obtain better information on the experimental results, and general results from this code, for parameters similar to those in the experiment, are shown. A more detailed investigation of the Trivelpiece-Gould soliton is presented in Section 4, with special attention given to the interaction between the soliton and the resonant electrons, moving in the background plasma with velocities near the soliton velocity. Section 5 is devoted to the electron hole, while Section 6 describes interactions between the solitary structures, i.e. hole-hole and soliton-hole collisions. Finally, a conclusion is presented in Section 7.

2. EXPERIMENTAL OBSERVATIONS

The experimental part of this work was initiated whilst Dr. K. Saeki from Tohoku University, Sendai, Japan was a summer guest at Risø in 1977. Saeki proposed an experimental set-up, described in Section 2.1, similar to one he had previously used for investigating electron plasma wave shocks. In a paper on these shocks, Saeki (1973) anticipated the formation of socalled "electron holes", which should appear as nonlinear pulses of positive potential, containing a large number of trapped electrons. The main purpose of our experiment was to excite such electron holes and to investigate their characteristic behaviour. However, since our experimental set-up also excited Trivelpiece-Gould solitons, a large part of the experimental work was concerned with investigations of the propagation of these solitons and, in particular, the modifying effect on the solitons of dissipation, due to the resonant electrons.

2.1. Experimental set-up

The experiment was conducted in Risø's large Q-machine (Andersen, 1970; Motley, 1975) which was operated in the single-ended mode, i.e. only a plasma source in one end of the machine was used. The experimental set-up is shown schematically in Fig. 1. A cesium plasma was produced by surface ionization on a hot 3-cm diameter tantalum cathode (~ 2000 K). A homogeneous magnetic field of approximately 0.4 T confined the plasma radially. The length of the entire plasma column was 120 cm. Electron temperatures were approximately 0.2 eV determined by the hot plate, and the ratio of electron-to-ion temperature was close to unity. Plasma densities were in the range 10^6-10^7 cm^{-3} and the neutral background pressure was 10^{-6} mm Hg. Since the different (electron-neutral, electron-ion, etc.) collisional mean free paths are all longer than the length of the machine, collisions are entirely unimportant for the wave propagation. It should be

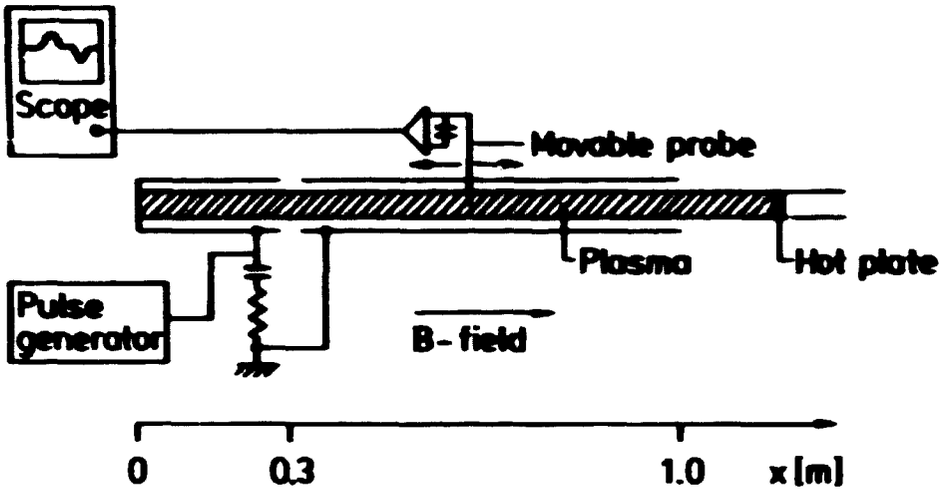

Fig. 1. Experimental set-up.

noted that $\omega_p << \omega_c$ (ω_p and ω_c are the electron plasma and electron cyclotron frequencies, respectively). This means that the magnetic field may be considered infinitely strong, so that wave propagation can be described as a one-dimensional problem.

In order to ensure well-defined radial boundary conditions for the electric field in the plasma waves, the plasma was surrounded by a 4-cm i.d. grounded cylindrical brass tube acting as a waveguide. Pulses or waves were excited by means of a 30-cm long terminating brass tube. The potential of this tube could be varied, and thereby an electric field was applied across the gap separating the exciter tube from the main waveguide. For negative applied potentials, this electric field injected electrons into the main plasma. The exciter tube thus acts as an electron reservoir and is, at large applied amplitudes, a much more effective exciter than a simple probe. Potential variations in the plasma were detected by a Langmuir probe connected directly to a high-impedance capacitive amplifier (1 MΩ, 2 pF) located outside the plasma. A slot in the waveguide surrounding the plasma allowed an 85-cm axial movement of the detecting probe.

2.2. Basic observations

By applying small amplitude potential oscillations to the exciter, we were able to measure the linear dispersion relation for the high-frequency electron oscillations in our system, as shown in Fig. 2. The positive wave-numbers, k, correspond to waves propagating in the "upstream" direction from the exciter tube towards the hot plate. The "downstream measurements were performed by exciting the waves by means of an extra probe inserted in the plasma close to the end of the waveguide near the hot plate.

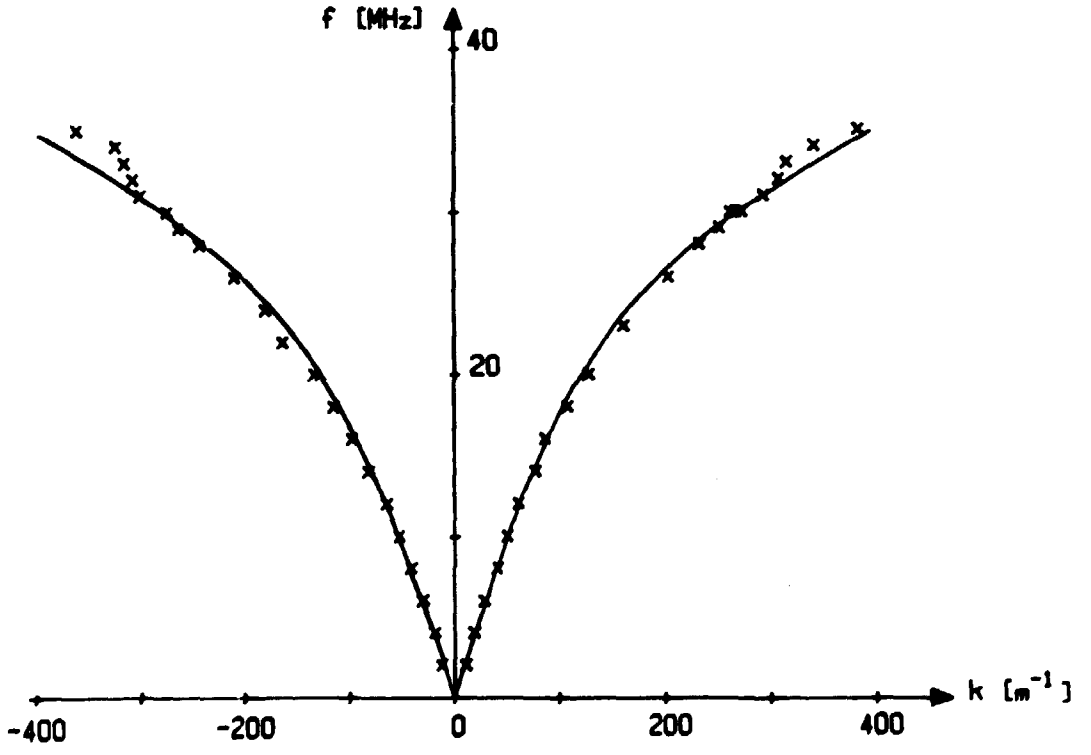

Fig. 2. Experimental and calculated small-amplitude dispersion relation.

The solid line in Fig. 2 represents the theoretical dispersion relation named after Trivelpiece and Gould (1959). This Trivelpiece-Gould dispersion relation assumes a constant radial plasma density from r = 0 to the waveguide boundary at r = r_o. When considering only the lowest-order radial mode for the perturba-

tions introduced by a wave and including the effect of finite electron temperature, the dispersion relation takes the form

$$\omega^2 = \omega_p^2 \frac{(ka)^2}{1 + (ka)^2} + 3v_e^2k^2 \qquad (1)$$

where $a = r_o/2.404$ originates from the radial boundary condition, $v_e = (T_e m)^{\frac{1}{2}}$, and T_e and m are the electron temperature and mass, respectively. In order to calculate the relation corresponding to the solid line in Fig. 2, we determined v_e from the hot plate temperature and fitted the values of a and ω_p.

The result for a was 0.65 cm, which is smaller than the value a = 0.83 cm obtained by using the actual r_o = 2 cm, but this is to be expected, since the hot plate is only 1.5 cm in radius so the experimental plasma density does not have a constant radial profile. From (1) it is seen that the phase velocities of the waves are always greater than v_e, and since the ratio of electron-to-ion thermal velocity, v_e/v_i, was of the order of 500, the ions in the following may be considered as an immobile background of positive charge.

Applying a short negative pulse with a time duration of the order of $\tau_p = 2\pi/\omega_p$ (the plasma period) to the exciter, plasma responses were obtained as those shown in Fig. 3. In this figure, oscilloscope traces at a fixed probe position are shown for different amplitudes of the applied pulse, ϕ_a. When ϕ_a was small $(e\phi_a/m(\omega_p a)^2 < 0.05)$ the plasma response was linear (trace a), which was checked by changing the polarity of the applied pulse and obtaining the same, but inverted, plasma response. It should be noted that here and in the following the wave potential, ϕ, is drawn with negative values on the positive y-axis, so that the first pulse (to the left) corresponds to a compressional electron wave. The second pulse is due to a rarefaction wave, which initially was moving in the negative x-direction, but was reflected by the end plate of the exciter tube (see also Fig. 7).

When increasing ϕ_a, the plasma response became nonlinear (an example is shown on trace b in Fig. 3) and as a result the vel-

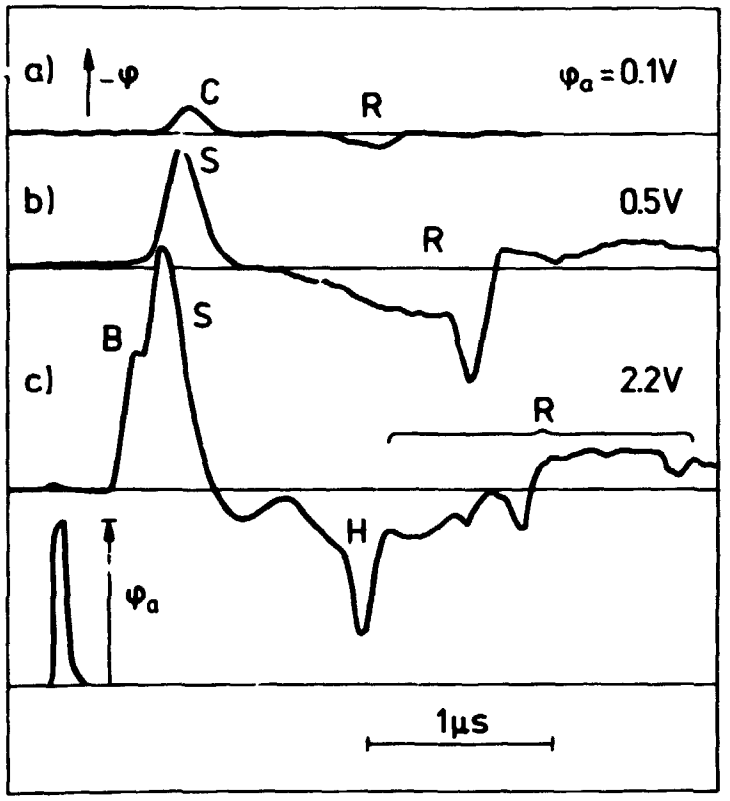

Fig. 3. Oscilloscope traces showing the plasma response at a fixed position (x = 0.8 m) for different amplitudes of the applied pulse. ϕ_a. The letters denote: C) the linear compressional wave, R) the linear rarefaction wave, S) the soliton, B) the burst, and H) the hole. The values of $e\phi_a/\frac{1}{2}m(\omega_p a)^2$ are 0.08, 0.4, and 1.8 in traces a), b) and c), respectively. The potentials are shown in arbitrary units.

ocity of the compressional pulse became dependent on the amplitude of the potential of the plasma pulse, ϕ_o. This is shown in Fig. 4, where the Mach number, M, is defined as the ratio of the pulse velocity to the linear velocity, C_o. The straight solid line shows that M increases linearly with ϕ_o, indicating that the compressional pulse was a Trivelpiece-Gould soliton previously investigated by Ikezi et al. (1971).

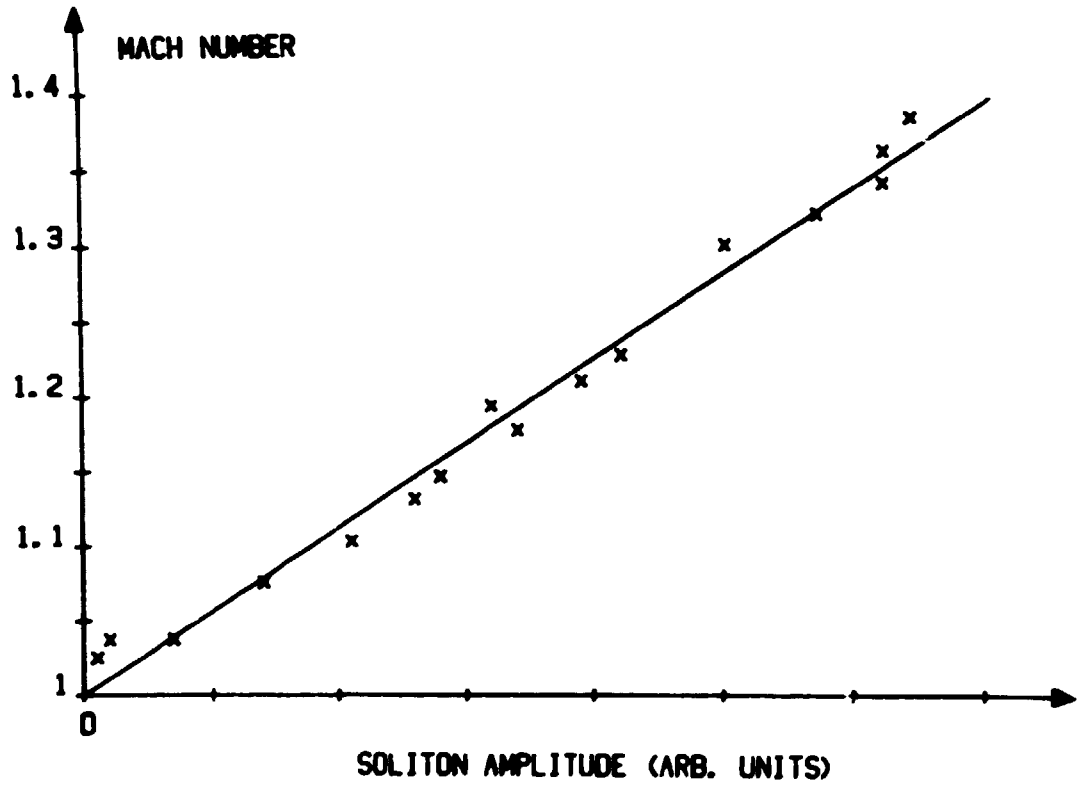

Fig. 4. Experimental results for the Mach-number ($M = v/C_0$) versus the soliton amplitude.

If ϕ_a exceeded a critical value, ϕ_c, which in our experiment was found to be $\phi_c \cong 1$ v (corresponding to approximately $\frac{1}{2}(m/e)(\omega_p a)^2$), a new pulse was created after the soliton (see trace c in Fig. 3). This new pulse had a positive potential indicating a deficit of electrons and was, actually, the object of primary interest of our first experiments, called the "electron hole". We also noted that an additional negative pulse appeared in front of the soliton. This pulse was due to a burst of free-streaming electrons which was generated by the excitation mechanism (Ikezi et al. 1971). The velocity of the leading edge of the burst versus the amplitude of the applied pulse is plotted in Fig. 5. We may imagine that the burst was generated in the region of the external electrical field, which had a width approximately equal to a, by the local acceleration of the initially almost resting electrons. The resulting velocity of electrons then was due partly to the acceleration through the applied potential and

partly to the initial movement of the potential generated inside the plasma. In order to test this hypothesis we fitted the expression

$$\tfrac{1}{2} m v_b^2 = C_1(\tfrac{1}{2} m v_{ph}^2) + C_2(e \phi_a) , \qquad (2)$$

where v_b = the burst velocity and v_{ph} = the initial velocity of the plasma wave, the value of which is taken from the linear measurements. The result is shown by the solid line in Fig. 5, where the values of the fitted parameters C_1 and C_2 are C_1 = 1.2 and C_2 = 0.95. It should be noted that Ikezi et al. (1971) predict an expression for the burst velocity that differs

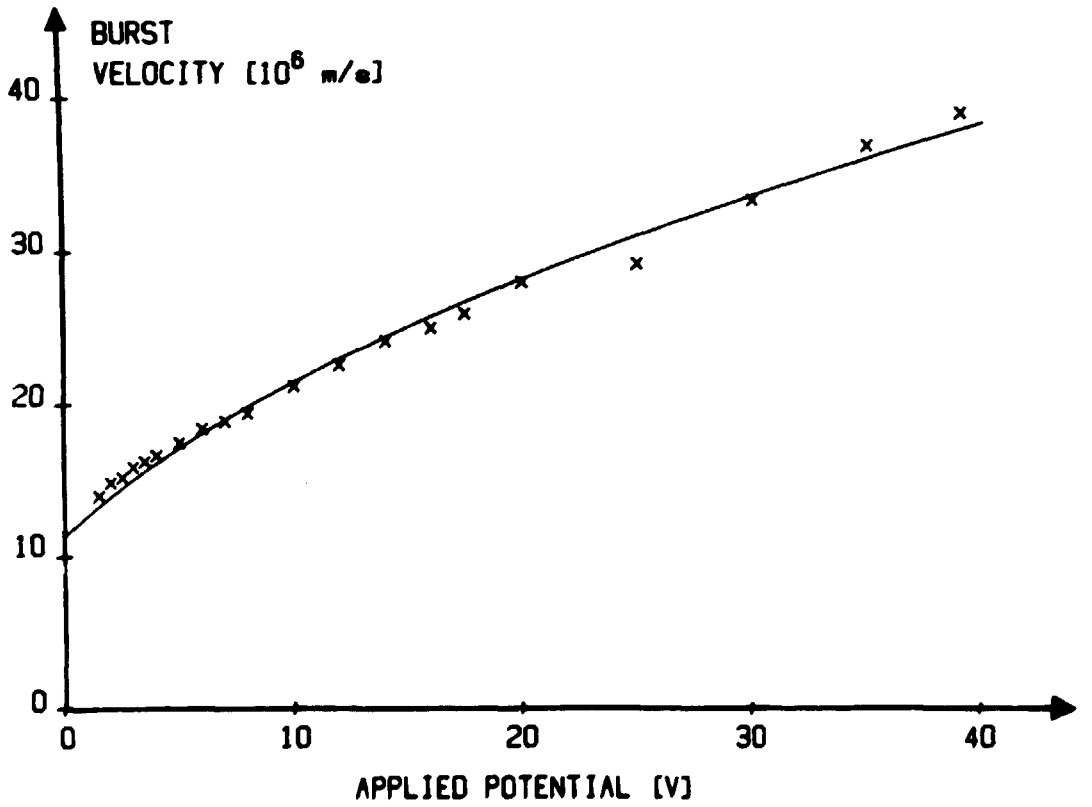

Fig. 5. Velocity of the electron burst v_b versus the applied potential ϕ_a. The solid line is fitted according to Eq. (2).

slightly from (2), since they use $v_t = (2T_e/m)^{\frac{1}{2}}$ instead of v_{ph}. However, the excitation method that they employ is not the same as we have used.

In Fig. 6, oscilloscope traces at different probe positions are shown, and the evolution of the burst, soliton and hole, can be seen. We note that the soliton was damped, while the electron hole, when fully developed, propagated virtually without a

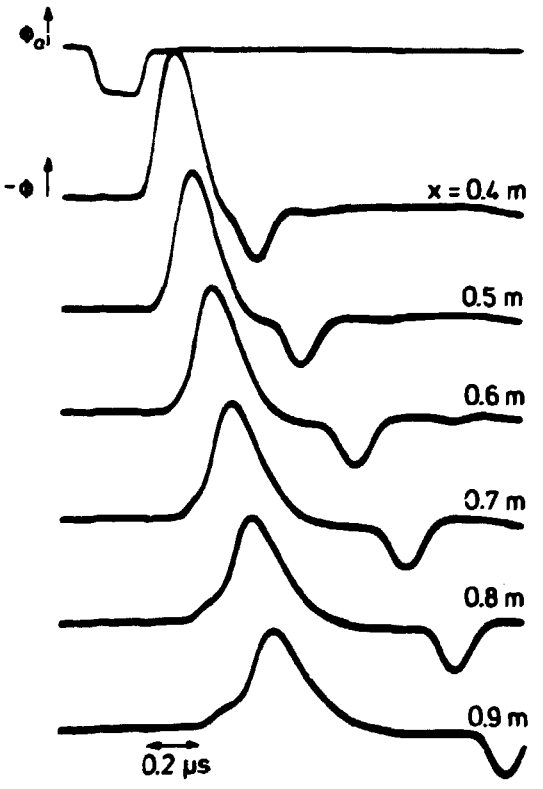

Fig. 6. Time pictures of soliton, burst, and hole at different positions. The applied potential ϕ_a and the measured potential ϕ are in arbitrary units.

change of shape. This shows that the electron hole is, indeed, a solitary wave. In Fig. 7, the trajectories of the soliton, the electron hole, and the rarefaction wave are shown in an (x-t)-diagram. The characteristic velocities of the soliton and the rarefaction wave is $\omega_p a$, which should be expected from (1)

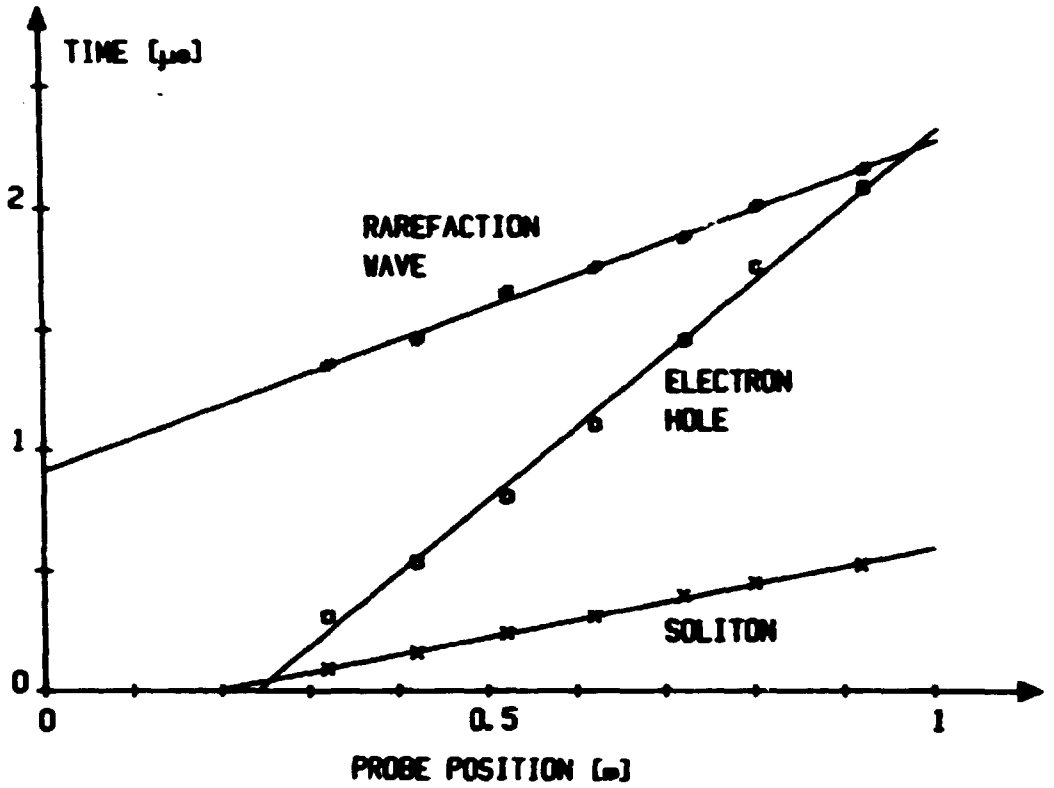

Fig. 7. (x-t)-diagram with soliton, electron hole, and rarefaction wave.

since these waves have $ka << 1$ and since $\omega_p a > v_e$. On the other hand, the characteristic velocity of the electron hole is smaller, namely, on the order of v_e. In our experiment $\omega_p a/v_e$ is 2-6.

The more detailed properties of the Trivelpiece-Gould soliton and the electron hole will be given in Sections 4-6, but first, the next section will give a description of the computer simulation scheme and the basic results of simulating the experiment.

3. NUMERICAL SIMULATION

In order to obtain a better insight into the features of the experimental observations, numerical simulations of the experiment were performed. The computer code was written by Dr. V.A. Turikov from the Patrice Lumumba University, Moscow, U.S.S.R., while he visited Risø for ten months in 1977-78.

3.1. Numerical scheme

The cloud-in-cell method was employed in the simulations. Actually, the method in our previous publications was called a "particle-in-cell" method. However, the scheme, in order to reduce the "shot noise" inherent in the usual particle-in-cell method, calculates the self-consistent electrical field by making use of a reverse linear interpolation to distribute the charge of each simulation particle between the two nearest grid points. This feature is typical of the cloud-in-cell method (Birdsall et al. 1969) when each simulation particle is described by a "cloud" with a uniform density inside the cloud boundaries, which have a separation equal to the grid distance.

Each simulation particle was moved according to Newton's 2nd law, where the force term is proportional to the sum of the external and the self-consistent electrical fields. For the calculation of the temporal evolution of the equations of motion a leap-frog scheme was applied, apart from the first step that was realized by Euler's method. The self-consistent electrical potential was calculated from Poisson's equation in the form

$$\frac{\partial^2 \phi}{\partial x^2} - \frac{\phi}{a^2} = \frac{e}{\varepsilon_o} (n-n_o) \ , \qquad (3)$$

appropriate for a strongly magnetized plasma with immobile ions

in a waveguide where only the lowest radial mode is considered (Saeki et al., 1979b, Lynov et al., 1979a).

In all the simulations shown in this paper the space step, or grid distance, was set equal to the Debye length, λ_D, while a time step was taken to be 0.315 ω_p^{-1}. The initial number of simulation particles in a Debye cell was 50, corresponding to a maximum number of particles of 50,000 with a total plasma length of 1000 λ_D. In the experiment the system length was 1 m corresponding to 1000 λ_D for $n_o = 10^7$ cm^{-3} and $T_e = 0.2$ eV. The initial electron velocity distribution was generated randomly with Gaussian statistics in velocity space and uniformly in real space. Reflecting boundary conditions for the simulation particles were assumed at both ends of the plasma, these being the most appropriate for simulating the experimental situation. Correspondingly, $\partial\phi/\partial x = 0$ was used as boundary conditions for the potential. The accuracy of the code was checked by calculating the total energy at each time step. Energy conservation was found to be better than 3% within the maximum 25 plasma periods ($\tau_p = 2\pi/\omega_p$) that the plasma was simulated. The excitation was represented by applying an external (negative) potential at one end of the system, giving rise to a perturbing electric field around $x = 400\ \lambda_D$ with the shape of one-half period of sin (x/r_o) where r_o is the plasma radius. The time dependence of the external field was taken to be a full period of $1-\cos(\pi t/\Delta T)$, where the width ΔT usually was chosen to be τ_p. For a more detailed description of the simulation code see Turikov (1978a,b).

3.2. General results

An example of the results from a run of the simulation code is shown in Fig. 8. The values of the parameters used in this example correspond to those in the experiment and are $n_o = 10^7$ cm^{-3}, $T_e = 0.2$ eV, $r_o = 2$ cm, and $\phi_a = m(\omega_p a)^2/e$. Figure 8a shows the evolution of the potential, and we clearly recognize the soliton, the electron hole, and the rarefaction wave. In Fig. 8b, the evolution of the particle distribution function in

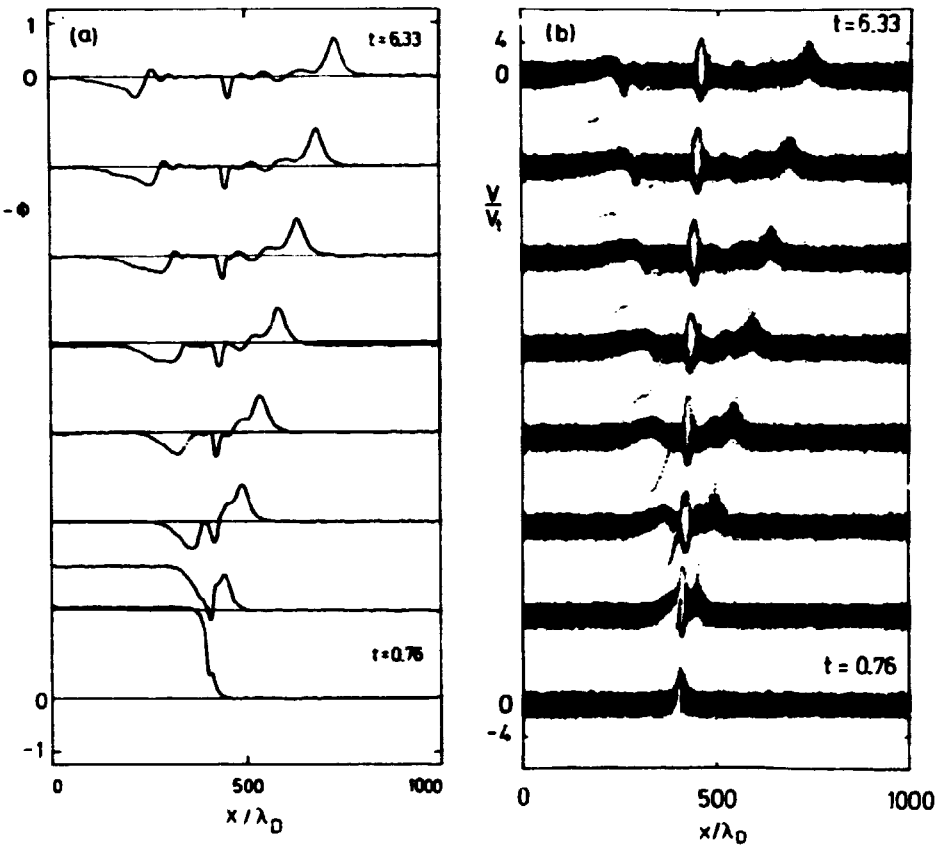

Fig. 8. Numerical simulation results for $\omega_p a/v_t = 5.59$ and $\phi_a = m(\omega_p a)^2/e$. (a) The potential for increasing time and (b) the corresponding phase space pictures. The plotted potential ϕ is normalized with $\frac{1}{2}m(\omega_p a)^2/e$ and t is in units of τ_p.

the phase space is shown at instants corresponding to the potential plots in Fig. 8a. In the phase space pictures the instantaneous x- and v-coordinates of each simulation particle are indicated by a small black dot.

In the phase space plots we observe that the rarefaction wave as well as the soliton must be well-described as fluid phenomena. However, the distinct vortex in the distribution function, which has given the name to the electron hole, indicates that this structure is a purely kinetic phenomenon, consisting of a large number of trapped electrons.

After this short presentation of the basic experimental and numerical simulation results, we shall, separately, turn to the more detailed investigations of the Trivelpiece-Gould soliton and the electron hole.

4. THE TRIVELPIECE-GOULD SOLITON

As mentioned in Sec. 2, the primary interest of our first experiments (Saeki et al., 1979b; Lynov et al., 1979a) was to investigate the electron hole. However, at the Chalmers Symposium on Solitons in Physics, 1978 in Gothenburg, Sweden, we became aquainted with the theory by Karpman and Maslov (1977, 1978) on the evolution of solitons in the presence of a perturbation. By comparing the general results of this theory, presented by Karpman (1979a), with our results from the initial experiments and simulations (Lynov et al., 1979a), we found some interesting characteristic behaviour, e.g. the formation of a tail after the soliton that gave an impulse to a collaboration on the modification of Trivelpiece-Gould solitons by the resonant electrons (Karpman et al. 1979, 1980). In this way the investigations of the soliton, though originally a "by-product" of the electron hole experiments, became the subject of the most attention, due to the availability of Karpman's very detailed theory.

4.1. Theory

In the following, a description will be given of the basic equations and the derivation from them, in the fluid approximation, of the Korteweg-de Vries (KdV) equation. Furthermore, the inclusion of the kinetic effects due to the resonant electrons will be outlined and the modification of the KdV soliton by these resonant particles will be stated. For this theoretical section, a general reference, containing a more detailed de-

scription of Karpman's calculations, is Karpman, Lynov, Michelsen, Pécseli, Rasmussen and Turikov (1980).

4.1.1. Basic fluid behaviour

The fundamental equations describing the experimental system, namely a plasma that is contained in a cylindrical waveguide (with radius r_o) placed in a strong magnetic field ($\omega_c >> \omega_p$) directed along the axis of the cylinder, is the Vlasov equation, in the form (Lynov et al. 1979a)

$$\frac{\partial \tilde{f}}{\partial t} + v \frac{\partial \tilde{f}}{\partial x} + \alpha \cdot \frac{e}{m} \frac{\partial \phi}{\partial x} \frac{\partial \tilde{f}}{\partial v} + \frac{e}{m} \frac{\partial \phi}{\partial x} f_o'(v) = 0 \ , \qquad (4)$$

and the Poisson equation, in the form (Saeki et al., 1979)

$$\frac{\partial^2 \phi}{\partial x^2} - \frac{\phi}{a^2} = \frac{e}{\varepsilon_o} \int_{-\infty}^{\infty} \tilde{f}(x,v,t)\, dv \ . \qquad (5)$$

In these equations $\tilde{f}(x,v,t) + f_o(v)$ is the total velocity distribution function, $f_o(v)$ being the unperturbed part; the constant $\alpha = 0.72$ (Rasmussen, 1977) originates from the consideration of only the lowest-order radial mode. The coupling to higher-order radial modes can safely be ignored (Laval et al., 1969; Franklin et al., 1975) in the long wavelength limit appropriate for our investigations.

By introducing the "effective distribution function"

$$f(x,v,t) \equiv \alpha \cdot (\tilde{f}(x,v,t) + f_o(v)/\alpha), \qquad (6a)$$

and the variable

$$U \equiv -\frac{\alpha e \phi}{m} \ , \qquad (6b)$$

we can write Eqs. (4) and (5) as

$$\frac{\partial f}{\partial t} + v \frac{\partial f}{\partial x} - \frac{\partial U}{\partial x} \frac{\partial f}{\partial v} = 0 \ , \tag{7}$$

and

$$\frac{\partial^2 U}{\partial x^2} - \frac{1}{a^2} U = - \frac{\omega_p^2}{n_o} \int_{-\infty}^{\infty} [f(x,v,t) - f_o(v)] \ dv \ , \tag{8}$$

where the unperturbed electron density

$$n_o = \int_{-\infty}^{\infty} f_o(v) \ dv \ . \tag{9}$$

In principle, Eqs. (7) and (8) form a complete system from which all results can be derived. However, it is convenient to use (7) only for the investigation of the resonant wave-particle interaction. As for the fluid effects, it is more convenient to use the fluid equations which can be derived from (7) as the moment equations. Introducing the linear, long wavelength ($ka << 1$) phase velocity, C_o, which, from the dispersion relation (1), is

$$C_o = \omega_p a \left(1 + \frac{3}{2} \frac{v_t^2}{\omega_p^2 a^2}\right)^{1/2} \ , \tag{10}$$

and by assuming that the thermal velocity $v_t << C_o$, one may, with sufficient accuracy, separate the motion of resonant and non-resonant particles. The resonant particles are those that have velocities in a region (to be defined later) near the phase velocity of the wave and therefore interact strongly with the wave's potential.

By neglecting the contribution from the resonant electrons, we may write Poisson's equation (8) in the fluid approximation as

$$\frac{\partial^2 U}{\partial x^2} - \frac{1}{a^2} U = - \omega_p^2 N \ , \tag{11}$$

where the relative density variation of the non-resonant electrons

$$N = \frac{n-n_o}{n_o} \ , \quad n(x,t) = \int_{-\infty}^{\infty} f(x,v,t)\, dv \ . \tag{12}$$

Here, $\int_{-\infty}^{\infty}$ denotes integration over the non-resonant region in velocity space (in the linear approximation it corresponds to the principal value integral).

From the first two moment equations of (7), a complete system of Boussinesq equations can be derived by assuming that $U/C_o^2 << 1$. Then, following a general method by Karpman (1975), we can derive the nonlinear fluid equation for wave propagation in the positive x-direction:

$$\frac{\partial U}{\partial t} + (C_o + \frac{3}{2C_o} U) \frac{\partial U}{\partial x} + \beta \frac{\partial^3 U}{\partial x^3} = 0 \ , \tag{13}$$

where

$$\beta = \frac{a^2 C_o}{2} = \frac{C_o^3}{2\omega_p^2} \ . \tag{14}$$

Equation (13) is readily identified as the KdV equation. A general solution to the localized initial value problem of the KdV equation can be found by use of the inverse scattering scheme (Gardner, Green, Kruskal, and Miura, 1967), but in this paper we shall be concerned only with the one-soliton solution to (13):

$$U(x,t) = U_o \, \mathrm{sech}^2[(x-x_o(t))/\delta] \ , \tag{15}$$

where the soliton velocity

$$\frac{dx_o}{dt} = C_o + \frac{U_o}{2C_o} , \tag{16}$$

and the soliton width

$$\delta = \frac{2C_o}{\omega_p U_o^{\frac{1}{2}}} . \tag{17}$$

4.1.2. Modifying effects by the resonant electrons

In order to include the effect of wave-particle interaction, we consider, instead of (11), the more accurate equation

$$\frac{\partial^2 U}{\partial x^2} + \frac{1}{a^2} U = - \omega_p^2 (N+N_r) , \tag{18}$$

where N_r is the relative density of resonant particles

$$N_r = \frac{1}{n_o} \int_r [f(x,v,t) - f_o(v)] \, dv , \tag{19}$$

and $\int_r$ indicates the integration over the resonant region of velocity space (we point out that this region is not included in the definition of N in (12)).

By assuming that N_r is smaller than the second-order terms (i.e., the dispersive and nonlinear terms) we find the following change in the KdV equation (13):

$$\frac{\partial U}{\partial t} + (C_o + \frac{3}{2C_o} U) \frac{\partial U}{\partial x} + \beta \frac{\partial^3 U}{\partial x^3} = - \frac{C_o^3}{2} \frac{\partial N_r}{\partial x} . \tag{20}$$

An equation similar to (20) was obtained by Van Dam and Taniuti (1973) (see also Taniuti, 1974) for the case of nonlinear ion acoustic waves, by means of the reductive perturbation method. However, the method which has just been outlined (Karpman et al., 1980) is simpler, based on physical arguments, and it could easily be used for the ion acoustic waves (Karpman, 1979b) as well as in other cases.

Considering the term on the right hand side of (20) as a small perturbation, it is possible to apply the general perturbation scheme by Karpman and Maslov (1977, 1978) based on the inverse scattering method (a similar perturbation scheme was independently developed by Kaup and Newell (1978)). As a result, the soliton solution (15) to the unperturbed KdV equation (13) is modified into the form

$$U(x,t) = U_o(t)\,\mathrm{sech}^2[(x-x_o(t))/\delta(t)] + U_o(t)w(x,t) \ . \quad (21)$$

In Eq. (21) the first term on the right-hand side is the time-dependent "soliton part" of the solution. Introducing the dimensionless variable

$$\nu(t) \equiv (2U_o(t)/v_t^2)^{\frac{1}{2}} \ , \quad (22)$$

the result of the perturbation analysis concerning the soliton growth rate can be expressed as

$$\frac{\partial \nu}{\partial t} = -\frac{\omega_p}{4\sqrt{2}}\frac{C_o}{v_t}\int_{-\infty}^{\infty}\frac{\partial N_r[\mathrm{sech}^2 z]}{\partial z}\,\mathrm{sech}^2 z\,dz \ . \quad (23)$$

It should be mentioned that the growth rate can be obtained directly from Eq. (20) in a simple way, considering the change rate of soliton "energy". The growth rate can also be explained in simple physical terms, without derivation of the detailed model equation (20), by use of energy arguments concerning the soliton and the reflected electrons (Lynov et al., 1979b). With either of these two methods it can be seen that the energy loss from the soliton due to the generation of the "tail", to be described soon, is not included in the perturbation scheme based on the inverse scattering method; this also has been pointed out by Ko and Kuehl (1980). Both of these methods are described further in Appendix A.

After determining $U_o(t)$ from (23), the soliton width may be expressed as

$$\delta(t) = \frac{2C_o^2}{\omega_p U_o^{\frac{1}{2}}(t)} \quad , \tag{24}$$

and the soliton velocity as

$$\frac{dx_o}{dt} = C_o + \frac{U_o(t)}{2C_o} - \frac{C_o^3}{4U_o(t)} \int_{-\infty}^{\infty} \frac{\partial N_r}{\partial z} (z\,\mathrm{sech}^2 z + \tanh z + \tanh^2 z)\, dz \; . \tag{25}$$

In most cases, the last term on the right-hand side of (25) gives only a small contribution, so, in the following equations we can use the soliton (or "phase") velocity, v_{ph}, determined by

$$v_{ph} = C_o \left(1 + \frac{U_o(t)}{2C_o^2}\right) \; . \tag{26}$$

The second term on the right-hand side of Eq. (21) is the "non-soliton part" of the solution, and theory predicts that this part has the form of a tail that develops after the soliton. The tail consists of a part called the plateau, with almost constant amplitude, U_-, which is nearest the soliton, followed by an oscillatory part. The plateau corresponds to what some authors call a "shelf" (e.g., Kaup and Newell, 1978; Fernandez, Reinisch, Bondeson, Weiland, 1978) or a "residue" (e.g., Maxon and Viecelli, 1974a,b), and the theoretical expression for the asymptotic value of its relative height in our case is

$$\frac{U_-(t)}{U_o(t)} = \frac{4}{v^4} \left(\frac{C_o}{v_t}\right)^4 \left[- \int_{-\infty}^{\infty} \frac{\partial N_r[\mathrm{sech}^2 z]}{\partial z} (1 - \mathrm{sech}^2 z)\, dz \right] . \tag{27}$$

Of course, utilization of Eqs. (23)-(27) requires a knowledge of N_r in a more explicit form, and this will be given in the next section.

4.1.3. Explicit expressions for the number of resonant particles

The expression for N_r in Eq. (19) has two unknown quantities, namely the distribution function, f(x,v,t), and the resonant region of velocity space, indicated by "r". In order to find explicit expressions for f(x,v,t) and "r", it is first necessary to determine the characteristic times of the problem. One of these is the "time of resonant interaction", τ_r, defined as the soliton width divided by the velocity, relative to phase velocity, of the fastest electrons that can be reflected by the soliton, in other words,

$$\tau_r = \delta/(2U_o)^{\frac{1}{2}} = \sqrt{2}\, C_o^2\, (\omega_p U_o)^{-1} \quad . \tag{28}$$

It is important to note that this time is much shorter than the "soliton time", τ_s, which is defined (Karpman and Maslov, 1977) as the time of soliton transition through a distance equal to the soliton width (in the reference system moving with velocity C_o),

$$\tau_s = \delta\left(\frac{8C_o}{U_o}\right) = \frac{16C_o^3}{\omega_p U_o^{3/2}} \quad . \tag{29}$$

It is possible to write explicit expressions for N_r in two different time limits. For small times ($t \ll \tau_r$) we may assume that the resonant particles have moved only a short distance compared to δ. It is then appropriate to use unperturbed orbits for the motion of the particles, and by making use, also, of the integral of motion,

$$E = \frac{(v-v_{ph})^2}{2} + U \quad , \tag{30}$$

we can apply Liouville's theorem in order to find f(x,v,t). The major contribution to N_r comes from particles with $E \gg U_o$ (U_o is the soliton maximum), so we can use $|v-v_{ph}| > (2U_o)^{\frac{1}{2}}$ as the resonant region "r". If we finally make the first-order Taylor expansion

$$f_o(v_{ph} + v) = f_o(v_{ph}) + v\, f_o'(v_{ph}) \ , \tag{31}$$

we find that

$$N_r(x) = \frac{f_o'(v_{ph})}{n_o} \fint_{-\infty}^{\infty} \frac{U(x',t)}{x'-x} dx' \ , \quad (t \ll \tau_r) \ . \tag{32}$$

This form of N_r was also obtained by Ott and Sudan (1969) for the case of Landau damping of nonlinear ion acoustic waves due to electrons. Since these authors did not restrict their expression for N_r to $t \ll \tau_r$, they had to assume some mechanism to scatter the resonant electrons (e.g., a small amount of noise) in order to avoid nonlinear orbits of the resonant particles, in their case due to trapping of the electrons.

Since we do not wish to rely on any scattering mechanism, we must take into account the nonlinear resonant electron orbits due to reflection from the soliton. This can be done for large t ($t \gg \tau_r$). In this case it is convenient to divide the unperturbed distribution function into the odd and even parts with respect to v_{ph},

$$f_1(v) = \tfrac{1}{2}[f_o(v_{ph} + v) - f_o(v_{ph} - v)] \ ,$$

$$f_2(v) = \tfrac{1}{2}[f_o(v_{ph} + v) + f_o(v_{ph} - v)] \ . \tag{33}$$

Accordingly, we define

$$N_r = N_1 + N_2 \ ,$$

$$N_1 = N_r[f_1] \ , \qquad N_2 = N_r[f_2] \ . \tag{34}$$

Again, we can make use of the integral of motion, E, and Liouville's theorem, in which we may assume, for the case of $t \gg \tau_r$, that the reflected electrons ($E < U_o$) for $x < x_o$ (x_o is, as usual, the position of the soliton maximum) all originate from $x = -\infty$, while the transient electrons ($E > U_o$) originate from $x = +\infty$; and vice versa for $x > x_o$. Due to the oddness of

f_1, the contributions from the transient electrons moving in the opposite directions are cancelled, so the only contribution to N_1 is from the reflected electrons

$$N_1(x) = -\frac{\sqrt{2}}{n_o}\int_{U(x)}^{U_o}\frac{f_1[(2E)^{1/2}]}{[E-U(x)]^{1/2}}\,dE\ \mathrm{sgn}(x-x_o)\ ,$$

$$(t \ll \tau_r)\ . \quad (35)$$

The result for N_2 based on the even part of the distribution function is

$$N_2(x) = \frac{\sqrt{2}}{n_o}\int_{U(x)}^{E_r}\frac{1}{[E-U]^{1/2}}\left\{f_2[(2E)^{1/2}]-f_2[\sqrt{2}(E-U)^{1/2}]\right\}dE,$$

$$(t \ll \tau_r)\ . \quad (36)$$

For most physical relevant distribution functions (such as Maxwellians) the contribution to N_2 from the interval $U_o < E < \infty$ is negligible compared to the contribution from $U < E < U_o$, so in the following we put the energy limit of the resonant particles, $E_r = U_o$ for convenience.

If we introduce a dimensionless distribution function, $F(\sigma)$, as

$$f_o(v+v_{ph}) = \frac{n_o}{v_t}F\left(\frac{v+v_{ph}}{v_t}\right), \quad (37)$$

and the dimensionless quantities

$$\mu = \frac{v_{ph}}{v_t} = \frac{C_o}{v_t}\left(1+\frac{\nu^2}{4}\frac{v_t^2}{C_o^2}\right), \text{ and } \chi = \frac{U(x)}{U_o}\ , \quad (38)$$

we have

$$N_1(v,\chi) = -v\int_0^{(1-\chi)^{1/2}} \left\{F[u + v(\omega^2+\chi)^{1/2}] - F[u - v(\omega^2+\chi)^{1/2}]\right\} d\omega \ \mathrm{sgn}(x-x_0) \ , \qquad (39)$$

and

$$N_2(v,\chi) = v\int_0^{(1-\chi)^{1/2}} \left\{F[u + v(\omega^2+\chi)^{1/2}] + F[u - v(\omega^2+\chi)^{1/2}]\right\} d\omega - \int_{u-v(1-\chi)^{1/2}}^{u+v(1-\chi)^{1/2}} F[\omega]d\omega \ . \qquad (40)$$

Expressions for N_1 and N_2 corresponding to Eqs. (39) and (40), when $F(u)$ is a single- or a double-humped Maxwellian, are given in Appendix B. Figures 9-10 show some examples of N_1 and N_2 for the two cases listed in Table 1. $N_1(v,\chi)$ and $N_2(v,\chi)$, corresponding to Eqs. (39) and (40), are shown in Fig. 9, and in Fig. 10 the form of N_1, N_2, N_r and $\partial N_r/\partial x$ when $U(x)$ is an unperturbed soliton are shown.

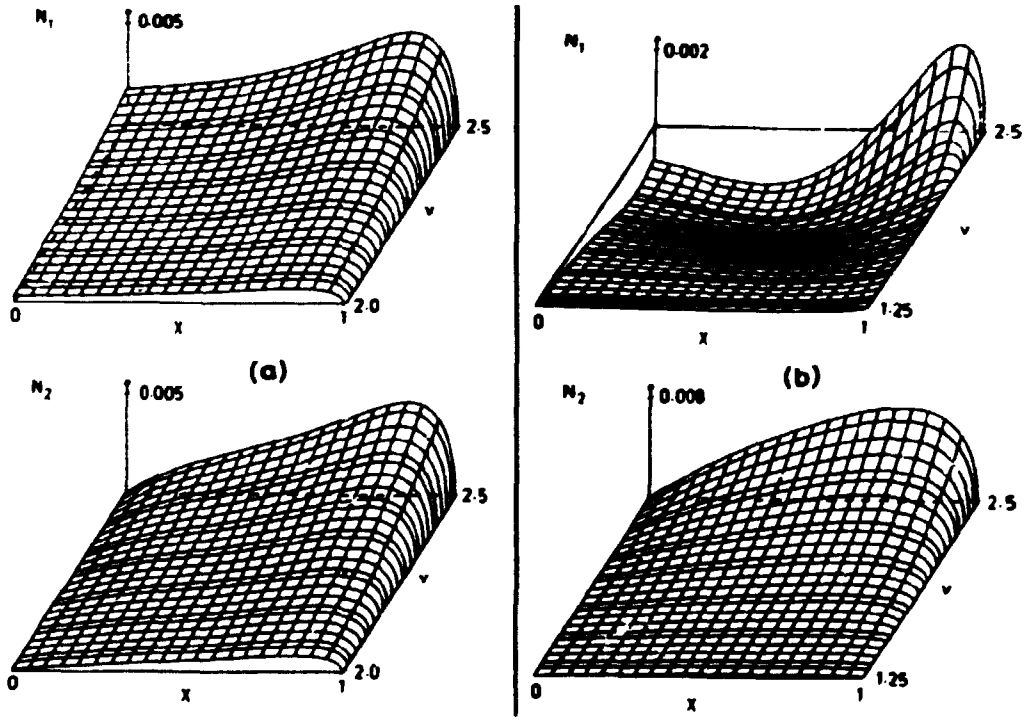

Fig. 9. The uneven and even part, $N_1(v,\chi)$ and $N_2(v,\chi)$, of the number of resonant electrons for (a) Case I and (b) Case II in Table 1. N_1 is shown for $x > x_0$.

Table 1. Parameters of the unperturbed plasma used in the examples, The unperturbed distribution consists of a main, non-drifting Maxwellian with a relative density (1-Δn) and a drifting Maxwellian with a relative density Δn, a drift velocity v_{db}, and the same temperature as the main Maxwellian (Δv_t = 1, see App. B).

Case	$\omega_p a/v_t$	f_o	(1-Δn)	Δn	v_{db}/v_t
I	4	single-humped	1	-	-
II	4	double-humped	0.995	0.005	7

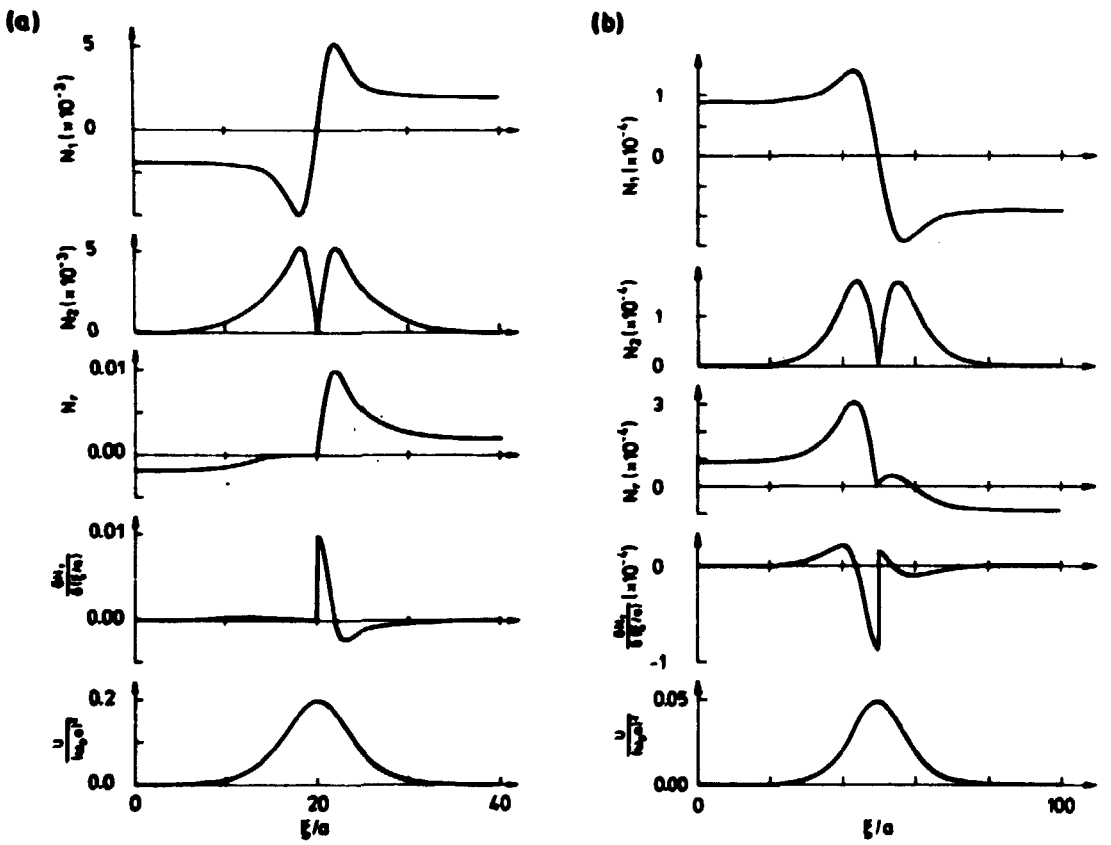

Fig. 10. The ξ dependence of N_1, N_2, N_r, and $\partial N_r/\partial \xi$ when $U(\xi)$ is an unperturbed soliton, for (a) Case I and (b) Case II in Table 1.

It should be pointed out that the expression for N_r given by (34), (39) and (40) is strictly valid only for single-humped, negative potentials (positive U), since multiple-humped potentials will give rise to trapping of some of the electrons, contrary to the assumption that all the reflected electrons originate from x = +∞ or x = -∞.

From (28) and (29) we have

$$\tau_r/\tau_s = (U_o/C_o^2)^{\frac{1}{2}}/8\sqrt{2}\ , \tag{41}$$

and since $U_o/C_o^2 < 1$ (U_o/C_o^2 is the basic small parameter guaranteeing the validity of the unperturbed KdV equation (13)), we see, as already mentioned, that $\tau_r \ll \tau_s$. In order to observe any change of the soliton, we are interested in $t > \tau_s$, so that the only expression for N_r of any practical relevance is given by (34), (39) and (40) for $t \gg \tau_r$. Insertion of these expressions into Eqs. (23) and (27) gives

$$\frac{d\nu}{dt} = \frac{\omega_p}{\sqrt{2}}\frac{C_o}{v_t}\frac{1}{\nu^2}\left[\int_{\mu}^{\mu+\nu}(\sigma-\mu)^2F(\sigma)d\sigma + \int_{\mu}^{\mu-\nu}(\sigma-\mu)^2F(\sigma)d\sigma\right], \tag{42}$$

$$\frac{U_-}{U_o} = \frac{8}{\nu^4}\left(\frac{C_o}{v_t}\right)^4\left\{\left[\int_{\mu}^{\mu+\nu}F(\sigma)d\sigma + \int_{\mu}^{\mu-\nu}F(\sigma)d\sigma\right] - \right.$$

$$\left.\frac{2}{\nu^2}\left[\int_{\mu}^{\mu+\nu}(\sigma-\mu)^2\,F(\sigma)d\sigma + \int_{\mu}^{\mu-\nu}(\sigma-\mu)^2\,F(\sigma)d\sigma\right]\right\}\ . \tag{43}$$

In the case of small ν, it can be shown (Karpman et al., 1980) that (42) takes the form previously obtained by Krivoruchko et al. (1974). Expressions for the soliton growth rate and the relative plateau height corresponding to Eqs. (42) and (43) when F(σ) is a single- or double-humped Maxwellian are given in Appendix B.

It should be noted that due to the oddness of $N_1(x)$ and the evenness of $N_2(x)$, only N_1 gives a contribution to (42) and (43). N_2 gives a contribution to the modification of the soliton velocity (25), which for $t >> \tau_r$ may be transformed to

$$\frac{dx_o}{dt} = C_o + \frac{U_o}{2C_o} + \frac{U_-}{4C_o} + \frac{C_o^3}{2U_o} \int_{-\infty}^{\infty} N_2(z) \frac{\cosh z - \sinh z}{\cosh^3 z} dz \ . \qquad (44)$$

However, for most cases the last two terms in (44) give only a very small contribution, so it is seen that the odd function N_1 is far more important for the soliton modification than the even function N_2, even though N_1 and N_2 may have comparable magnitudes.

As an important consequence of this fact, the direct numerical solutions to be presented in Sec. 4.2 of the model equation (20) also may be considered as solutions of the problem of modification of ion-acoustic solitons by resonant particles. In the case of ion-acoustic solitons, Karpman (1979b) has shown that the effect of resonant particles can be modelled by an equation identical to Eq. (20) (as mentioned previously, Van Dam and Taniuti (1973) arrived at the same result). Karpman also presented explicit expressions for the number of resonant particles, which consist of both ions reflected by the soliton and electrons trapped inside the soliton. As a result, the expression for N_r for $t >> \tau_r$ can be written as a sum of N_1, which is exactly equal to Eq. (35), and N_2, which is different from Eq. (36) due to the trapped electrons. But, since N_1 is more dominant than N_2, the effect of trapped electrons on the evolution of ion-acoustic solitons in most cases is negligible (for further details see Karpman, 1979b).

In order that the perturbation theory be applicable, the "perturbation time", τ_p, must fulfil the requirement (Karpman and Maslov, 1977, 1978)

$$\tau_p >> \tau_s \ , \qquad (45)$$

since the ratio $\varepsilon = \tau_s/\tau_p$ is the basic small parameter of the perturbation theory. It then turns out that the domain of applicability of the perturbation theory is limited in time by the condition (Karpman and Maslov, 1978)

$$t << \tau_p(\tau_p/\tau_s)^{\frac{1}{2}} = t_{max} \ . \tag{46}$$

An appropriate value for τ_p can be found (Karpman, 1979b) from the expression for the soliton growth rate (23) so that

$$\tau_p^{-1} = \frac{1}{\nu}\frac{\omega_p}{4\sqrt{2}}\frac{C_o}{v_t}\int_{-\infty}^{\infty}\frac{\partial N_r[\mathrm{sech}^2 z]}{\partial z}\,\mathrm{sech}^2 z\,dz \ . \tag{47}$$

In Fig. 11 we show τ_s/τ_p for $f_o(v)$ being a single Maxwellian and for different values of $\omega_p a/v_t$. We see that $\tau_s/\tau_p < 1$ requires $\omega_p a/v_t > 3$ and, furthermore, the value of ν must be larger than 0.1 and smaller than 0.5-1 times the value of $\omega_p a/v_t$. In order to make use of the unperturbed soliton solution to the KdV equation (13) based on the fluid approximations, U_o/C_o^2 must, as mentioned previously, be smaller than 1, so that ν in any case must be smaller than $\sqrt{2}\,C_o/v_t \sim \sqrt{2}\,\omega_p a/v_t$.

4.1.4. Direct potential contribution from the resonant electrons

At the end of this theoretical section, it should be pointed out that the model equation (20) for the soliton evolution correctly takes into account the modifying effects on the fluid potential due to the resonant electrons, but it does not include the direct contribution to the potential from the resonant electrons themselves. For example, N_r is a non-zero constant in front of the soliton where $U(x) \sim 0$ (see Fig. 10a), but due to the differentiation on the left-hand side of (20) there is no perturbation of the potential. This means that a "precursor" (Kato et al., 1972), which has a potential corresponding to the reflected electrons in front of the soliton, is not included in our description. However, it is possible to calculate the size of the potential of the precursor from Poisson's equation (18), where we may neglect N (since the potential due to the fluid effects

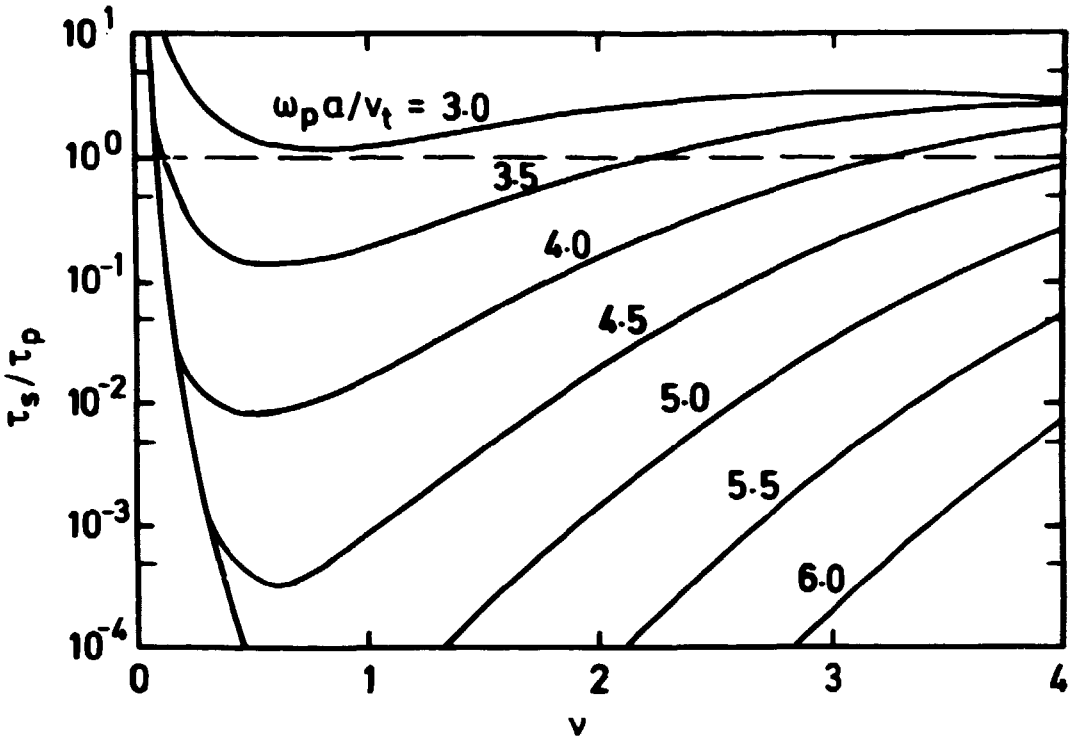

Fig. 11. The ratio of soliton time to perturbation time τ_s/τ_p versus v for different values of $\omega_p a/v_t$.

is approximately 0) and $\partial^2 U/\partial x^2$ (since $N_r(x) \sim$ constant), so that the precursor potential,

$$U_p = (\omega_p a)^2 \, N_r(\chi = 0, \, x > x_o) \, . \tag{48}$$

By using (39) for the calculation of N_r ($N_2(\chi = 0) = 0$) for a single Maxwellian distribution, we obtain the results shown in Fig. 12 for U_-/U_p. Here we have used three different values for $\omega_p a/v_t$, and have stopped the calculations when τ_s/τ_p became larger than 1 (see Fig. 11). It is clearly seen that the amplitude of the precursor is always smaller than the plateau amplitude, although for large soliton amplitudes, U_p becomes comparable to U_-. If one relaxes the requirements that $\tau_s/\tau_p < 1$, then for small values of $\omega_p a/v_t$ the precursor becomes very pronounced, but in this case the soliton itself suffers a strong distortion (see Fig. 16) and may no longer appear as merely a "perturbed" KdV soliton. In this way, it should be stressed

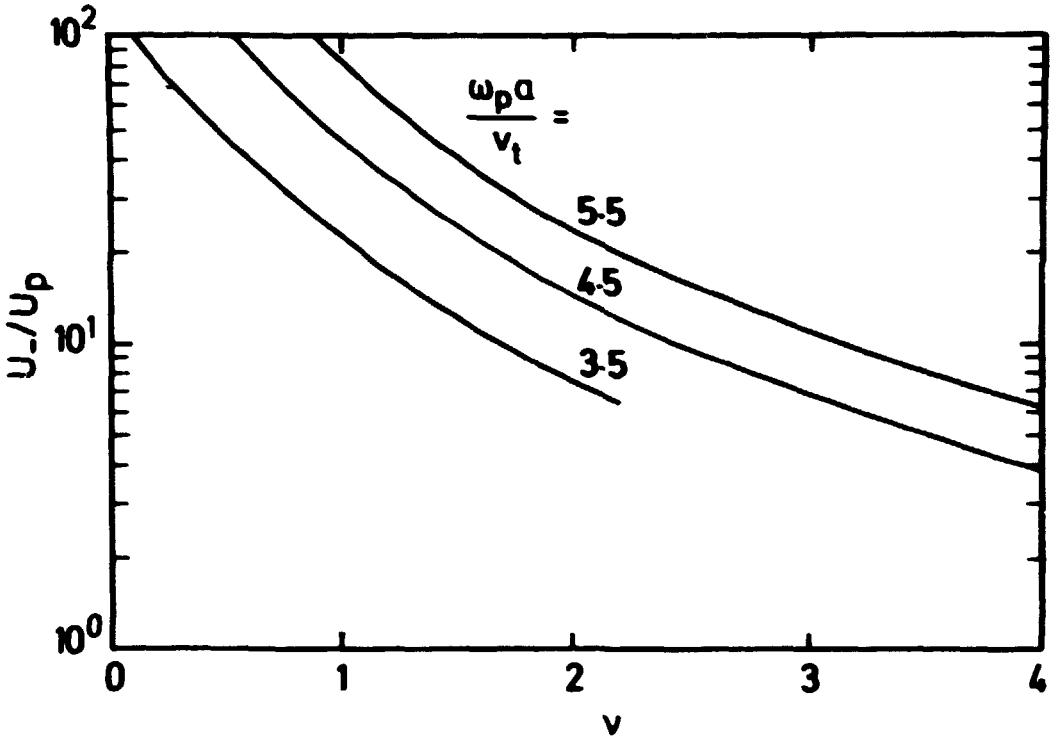

Fig. 12. The ratio of plateau height to precursor amplitude U_-/U_p versus v for different values of $\omega_p a/v_t$.

that it is the plateau behind the soliton, and not the precursor in front of the soliton that is the most characteristic modifying effect of the soliton due to the resonant electrons.

Finally, it may be appropriate to point out that the precursor can clearly be distinguished from the electron burst that was seen in the experiment and described in Sec. 2.2. Although both the precursor and the burst appear as negative potentials in front of the soliton, the former has a velocity approximately twice that of the soliton, while the latter has a velocity that depends upon the applied potential, as predicted by Eq. (2) and confirmed in Fig. 5. In any case, if one has either a precursor or a burst in an experiment, one should be careful in determining the relative height of this fast signal to the soliton, since the measuring probe may not only detect the instantaneous potential but also, to some extent, the instantaneous current or electron flux. This will, naturally, give rise to a measured

value of the relative height of the fast signal to the soliton that is too high.

4.2. Direct numerical solution of the model equation

In order to investigate the detailed behaviour of the model equation (20) directly and to compare the evolution of a soliton with the results of the perturbation analysis described in Sec. 4.1, Eq. (20) was put in a finite difference form suitable for numerical solution (Lynov, 1980). The number of resonant particles, N_r, was calculated for all $t > 0$ from the expressions (34), (39) and (40), which are strictly valid only for $t \gg \tau_r$, but, as we have seen in Sec. 4.1.3, $\tau_r \ll \tau_s$, so the solutions may be considered valid for all $t > 0$. In the numerical solution of (20) we chose to work in the reference system moving with the initial soliton velocity, so that the coordinate, ξ, is defined as

$$\xi = x - C_o\left(1 - \frac{U_o(t=0)}{2C_o^2}\right)t \ . \tag{49}$$

In this way we can see immediately if the soliton is accelerated, since an unperturbed soliton will be stationary in the ξ reference system.

The left-hand side of (20) was put on the finite difference form of the KdV equation first used by Zabusky and Kruskal (1965). The value of $\partial N_r/\partial\xi$ is determined at the same ξ positions where U is found and at the intermediate time steps of the three-level scheme of the left-hand side. In an attempt to minimize the effects of the boundaries of the finite system from $\xi = 0$ to L on the solution we chose to put

$$\left.\frac{\partial^2 U}{\partial\xi^2}\right|_{\xi=0,L} = \left.\frac{\partial^3 U}{\partial\xi^3}\right|_{\xi=0,L} = 0 \ . \tag{50}$$

Further details on the applied numerical method are given in Appendix C.

As an initial value we, naturally, used the soliton solution to the unperturbed KdV equation (13),

$$U(t=0) = U_o(0)\ \mathrm{sech}^2\left\{(\xi-\xi_0)\omega_p[U_o(0)]^{\frac{1}{2}}/2C_o^2\right\} . \qquad (51)$$

In order to check the accuracy of the program, the two quantities

$$Q_1(t) = \int_0^L U\ d\xi \quad \text{and} \quad Q_2(t) = \int_0^L \frac{1}{2} U^2\ d\xi , \qquad (52)$$

were calculated at each time step and compared with their theoretical values obtained directly by integration of Eq. (20) (see Appendix A).

In Fig. 13a we show the results for $U_o(0)/(\omega_p a)^2 = 0.2$; $f_o(v)$ is a single Maxwellian, and $\omega_p a/v_t = 4$. The values of τ_s/τ_p, $\omega_p t_{max}$, the space and time step, the system length, and the maximum relative difference between the calculated and the theoretical values of $Q_1(t)$ and $Q_2(t)$ are given in Table 2, where the values for the other examples in this section are also listed.

We immediately see that the solution develops in full qualitative agreement with the results of Sec. 4.1 since the soliton damps while generating a plateau region and a damped oscillatory tail behind it. It was found that the oscillatory part of the tail propagates in agreement with the linear dispersion relation corresponding to the unperturbed KdV equation (13).

The theoretical position of the soliton maximum, $\xi_o(t)$, is calculated by integration of Eq. (25) (see Appendix C for details) and by transformation according to (49). The result for $\xi_o(t)$ is shown by a solid vertical line on each curve of $U(\xi,t)$, where the dotted vertical line shows $\xi_o(t)$ when calculated from (25) by use of only the two first terms on the right-hand side corresponding to the usual soliton fluid velocity (16). The difference between these two values of $\xi_o(t)$ is due partly to the plateau and partly to N_2, as seen by inspection of (25).

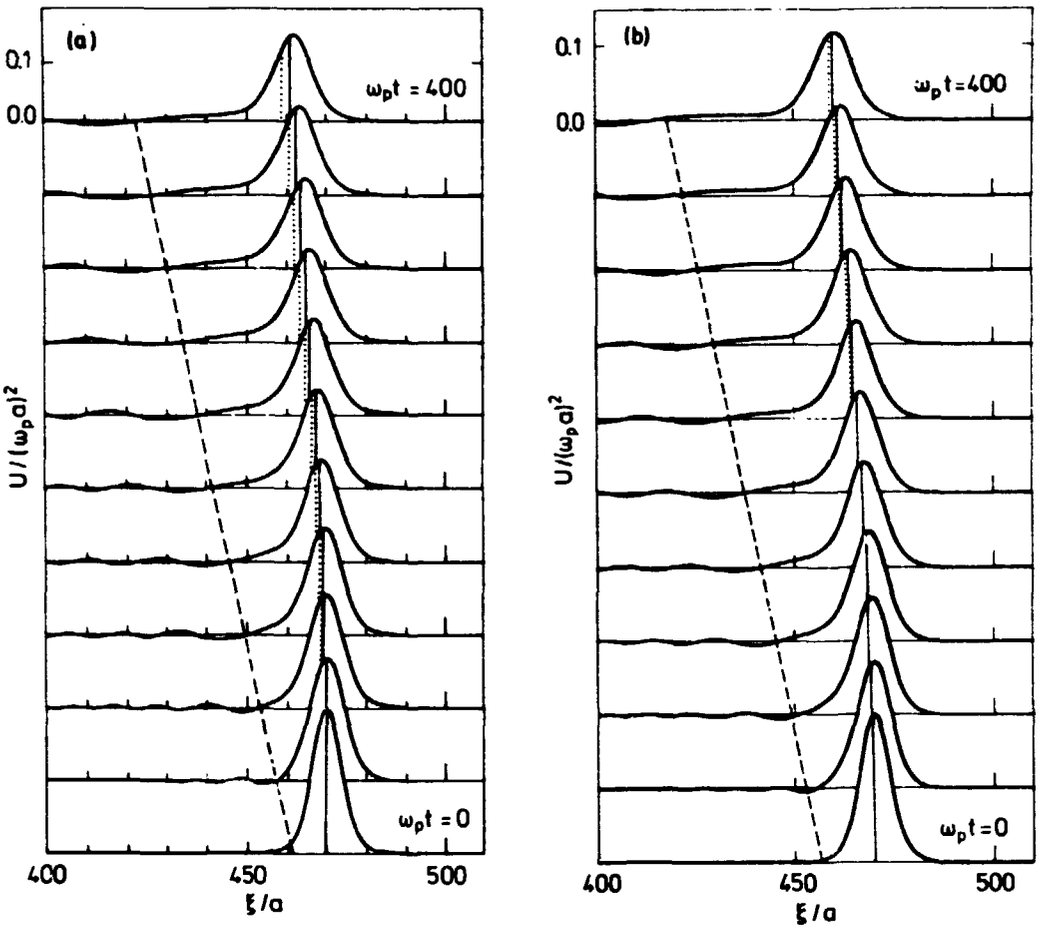

Fig. 13. Direct numerical solution of the model equation for $\omega_p a/v_t = 4$ and $U_o(t=0) = 0.2$. N_r consists of (a) N_1 and N_2, (b) only N_1. The vertical, dotted and solid lines at each time level indicate the predicted position of the soliton maximum corresponding to the fluid velocity and the complete perturbed velocity (25), respectively. The slanted, dashed line corresponds to the linear phase velocity C_o.

The dashed line indicates the position of a point moving with the velocity C_o relative to the laboratory frame, so we see that the transition point from the oscillatory to the plateau-shaped tail propagates with the linear phase velocity as predicted by Karpman and Maslov (1978).

Table 2. Values of various quantities in the examples in Sec. 4.2. The basic small perturbation parameter τ_s/τ_p is determined by use of Eqs. (47) and (29), and $\omega_p t_{max}$ by use of Eq. (46). h and k denote the space and time step, respectively (see App. C), L is the total system length, and ΔQ_1 and ΔQ_2 are the maximum values, during the numerical solution, of the relative differences between the theoretical and the actual values of Q_1 and Q_2, respectively (see App. A)

Figure	τ_s/τ_p	$\omega_p t_{max}$	h	k	L/a	ΔQ_1	ΔQ_2
13a	0.4	321	0.5	0.05	600	$5 \cdot 10^{-4}$	$2 \cdot 10^{-4}$
13b	0.4	321	0.5	0.05	600	$4 \cdot 10^{-4}$	$5 \cdot 10^{-5}$
15	0.03	9536	1	0.4	400	10^{-4}	$6 \cdot 10^{-5}$
16	1.4	96	0.5	0.05	400	$9 \cdot 10^{-3}$	$3 \cdot 10^{-3}$
17	0.3	~1000	1	0.4	800	$2 \cdot 10^{-3}$	$2 \cdot 10^{-2}$

In Fig. 13b we show the evolution of a soliton for the same parameters as in Fig. 13a, but in this case only the effect of N_1 is included. By comparing Figs. 13a and 13b, it is clearly seen that the effect of N_2 is vanishing, as predicted in Sec. 4.1.3, since the soliton damping and the soliton tail are almost exactly the same in the two cases, while the only difference is a slightly different soliton velocity. The influence of N_2 on the velocity is seen to be of the same order as the influence of the plateau, where the latter effect can be directly observed as the difference between the dotted and solid vertical lines in Fig. 13b. The plateau in this case serves to increase the soliton velocity , and the effect may be described as either a recoil effect on the soliton due to the ejection of the tail, or a repulsion effect between the plateau and soliton which have the same sign of charge. In the following examples both N_1 and N_2 are included, since the purpose of this section is to investigate the complete model equation for the Trivelpiece-Gould solitons.

The time dependence of v for the case shown in Fig. 13a (which has the same results as the case shown in Fig. 13b) is presented by a solid line in Fig. 14a, where the dashed line corresponds to the theoretical expression (42). The ratio of the plateau height to the soliton maximum, U_-/U_o, is shown in Fig. 14b where the shaded area corresponds to the estimated value of U_-/U_o found from the case shown in Fig. 13a (again almost the same results are found for the case in Fig. 13b). The solid line represents the value of U_-/U_o calculated from the theoretical expression (43), and it is seen that the theory predicts a somewhat lower value of U_-/U_o than is found by the numerical solution. However, the value of the upper limit for the perturbation theory (46) in this case is $\omega_p t_{max} = 320$, so that we cannot expect the theoretical prediction to be valid for U_-/U_o, which we first can begin to measure at $\omega_p t = 250$. The horizontal dashed line in Fig. 14b designates the value of U_-/U_o for $U_o =$

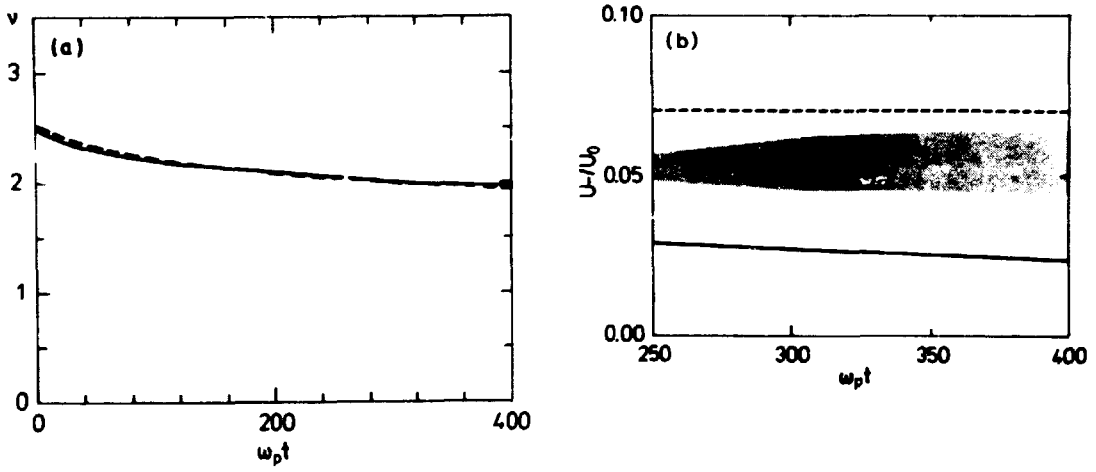

Fig. 14. (a) The solid line shows $v(t)$ found from the direct numerical solution shown in Fig. 13a while the dashed line corresponds to the theoretical expression in Eq. (42). (b) The shaded area shows the estimated value of the ratio of plateau height to soliton maximum, U_-/U_o, found from the numerical solution in Fig. 13a. The solid line is calculated from the theoretical expression (43) and the dashed line shows U_-/U_o for $U_o = U_o(t=0)$.

$U_o(t=0)$, so we see that the observed values of U_-/U_o at least lie between the theoretical predictions obtained from the actual $U_o(t)$ and from the initial $U_o(t=0)$.

In order to investigate the soliton modification for a case where the requirements for application of the perturbation theory are more accurately fulfilled, a numerical calculation was performed for a case similar to that shown in Fig. 13a, but with $U_o(0)/(\omega_p a)^2 = 0.05$, so that $\tau_s/\tau_p = 0.03$ and $\omega_p t_{max} = 9000$. The results are shown in Fig. 15 for $0 < \omega_p t < 5000$. We see that it is not possible to distinguish between the value of $v(t)$ obtained by the

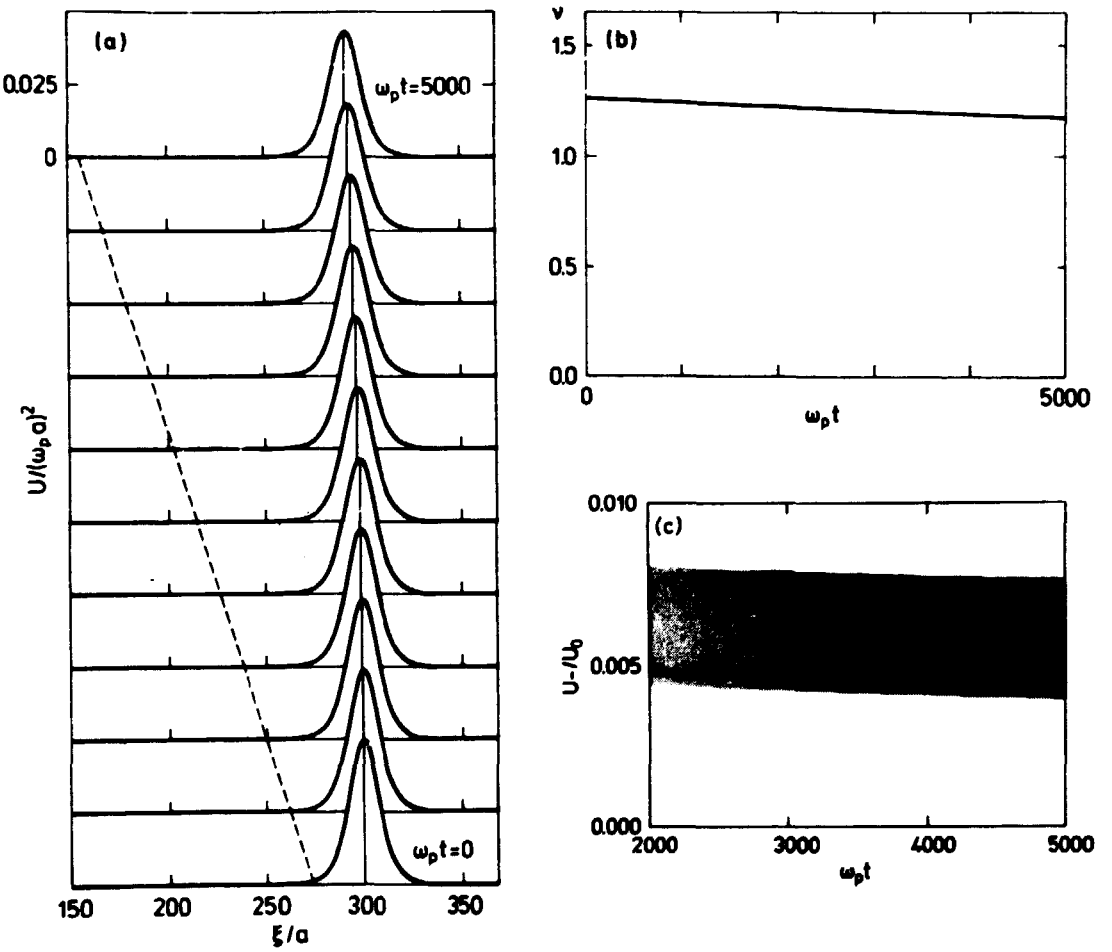

Fig. 15. Direct numerical solution for $\omega_p a/v_t = 4$ and $U_o(t=0) = 0.05$. (a) Similar to Fig. 13, (b) similar to Fig. 14a, and (c) similar to Fig. 14b.

direct numerical soliton of (20) and by the perturbation theory. Furthermore, the theoretical curve for U_-/U_o falls inside the measured region (even though close to the bottom), but now the value of U_-/U_o is so small that the plateau cannot be distinguished in Fig. 15a.

Figure 16 shows a case where the basic assumption for using the perturbation theory is violated, since $U_o(0)/(\omega_p a)^2 = 0.3$ and $\omega_p a/v_t = 3.6$, so that $\tau_s/\tau_p = 1.4$. In this case the soliton is so distorted that it is difficult to distinguish between the soliton body and the plateau. Nevertheless, the result from the perturbation theory concerning the soliton damping is in fairly good agreement with the observed $\nu(t)$, and also the theoretical prediction of U_-/U_o is at least within a factor of 2 of the estimated value.

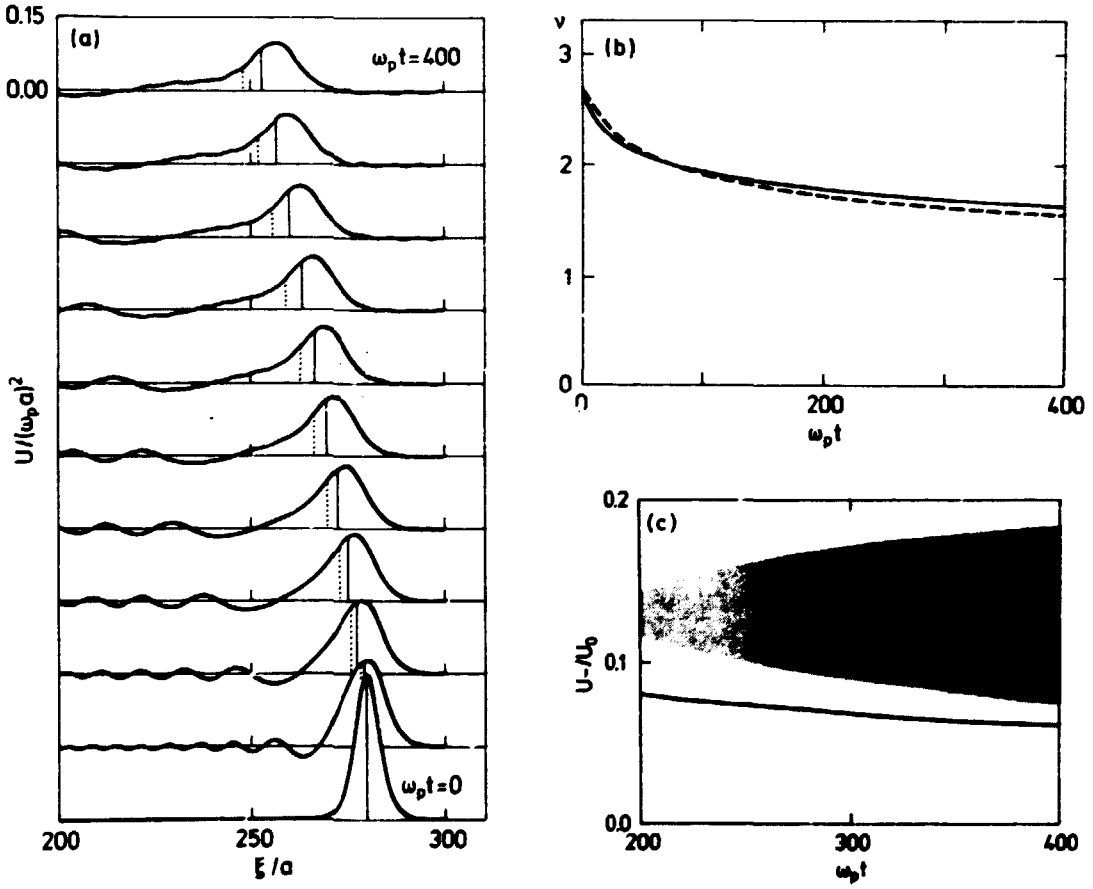

Fig. 16. Direct numerical solution for $\omega_p a/v_t = 3.6$ and $U_o(t=0) = 0.3$ shown as in Fig. 15.

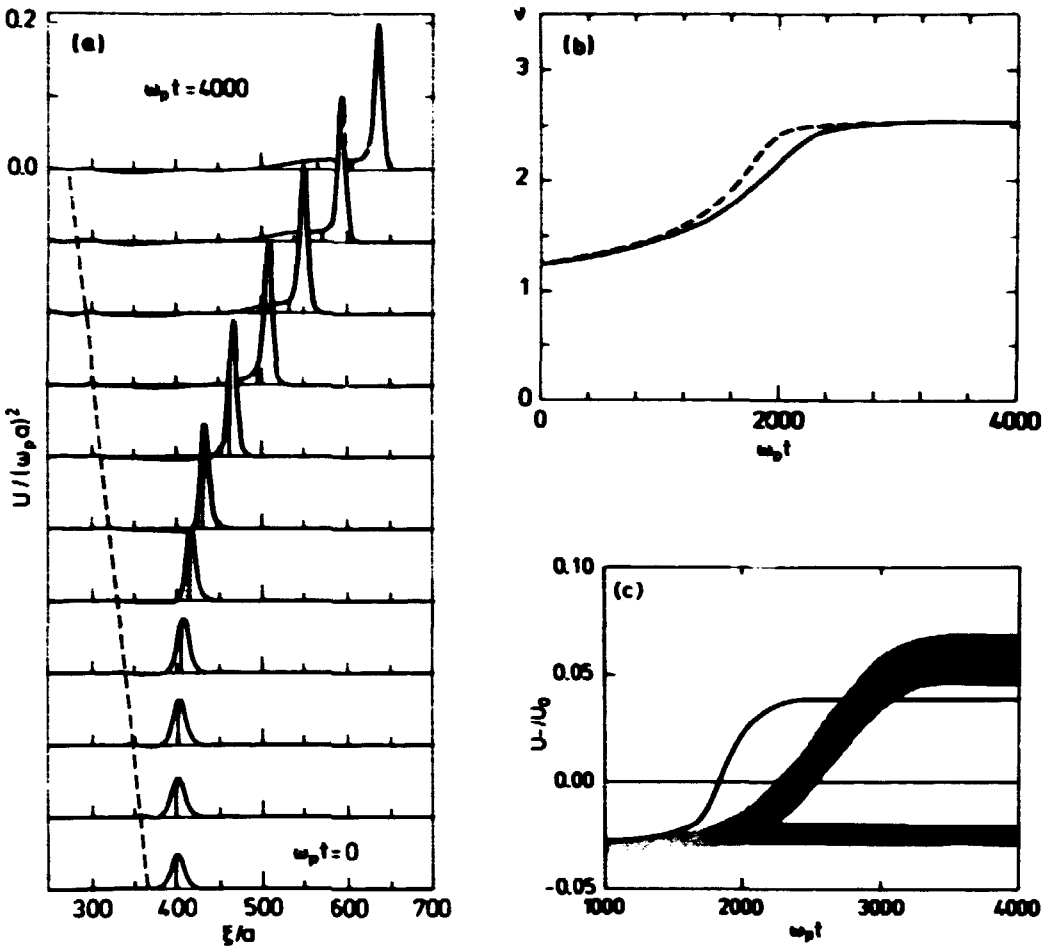

Fig. 17. Direct numerical solution for the double-humped velocity distribution function Case II in Table 1, with $U_0(t=0) = 0.05$. The results are shown in Fig. 15.

An example of soliton growth due to a double-humped $f_0(v)$ distribution is shown in Fig. 17 for parameters equal to Case II in Table 1 and with $U_0(0)/(\omega_p a)^2 = 0.05$. It is seen that the soliton starts to grow with a growth rate that is a little smaller than the theoretical, but reaches a maximum amplitude very close to the theoretical saturation level. The physical mechanism of the saturation is very simple, since it occurs when the soliton has reached a height and velocity, so that the electrons that are reflected in front of the soliton receive a total power equal to the total power given up by the electrons reflected from the back of the soliton (see also the theoretical expression (42)).

The soliton velocity also increases and reaches a saturation level, but the observed saturation velocity is approximately 20% larger than the theoretical value, when the velocities are measured relative to the ξ reference system, which corresponds to approximately a 6% larger value if the velocities are measured relative to a frame of reference moving with C_o. For $\omega_p t < 2000$ the plateau has the opposite sign of the soliton, in agreement with the perturbation theory, and, a little later than predicted by theory, the plateau turns to the same sign as the soliton. However, part of the plateau remains negative, and while the transition point from this negative plateau area to the oscillatory tail propagates, as usual, with the linear velocity C_o relative to the laboratory frame, the transition region between the positive and negative plateau is more or less stationary in the ξ reference system and becoming more and more wide. The saturation level of the positive plateau is a little higher than the theoretical value.

Experiments on soliton amplification in plasmas with double-humped velocity distribution have been performed by Krivoruchko et al. (1974), for the case of electron soliton amplification by an electron beam. It has been pointed out (Wainberg, 1959) that the interaction of an electron density solitary wave with an electron beam makes it possible to accelerate ions trapped in the potential well produced by the wave. The amplification of ion-acoustic solitons by a beam of charged particles has been investigated theoretically by Ostroskii et al. (1975) and experimentally by Okutsu et al. (1978).

It can be concluded from the numerical investigations of the model equation (20) that the modification of a soliton evolves in full qualitative agreement with the predictions of the perturbation theory, and, furthermore, if the requirements by the theory are strictly fulfilled, the quantitative agreement between the numerical solution and the theoretical results for the soliton growth rate, velocity, and the plateau amplitude, is very high. However, the requirements for application of the perturbation theory are rather restrictive, so that in order to be allowed to use the theoretical value of U_-/U_o in the case of

a single Maxwellian $f_o(v)$ distribution, the plateau must be so small that it scarcely can be detected. On the other hand, the theoretical values may be used as good estimates of the soliton modification also in cases where the perturbation is not extremely small, since these estimates are seldom more than a factor of 2 from the results obtained by the direct solution of the model equation.

4.3. Experiment

The experimental set-up and the general experimental results have already been presented in Sec. 2. In Fig. 4 we saw that the velocity of the compressional electron pulse was proportional to the amplitude of the pulse, confirming the basic fluid behaviour of a KdV soliton. It is seen that quite high Mach numbers can be obtained; however, $M > 1.2$ was accompanied by a pronounced distortion of the soliton, similar to the case of a high soliton amplitude in the model equation (Fig. 16). Using the theoretical expression for the unmodified soliton velocity (26) and the values of a and ω_p determined from the experimental dispersion relation (see Sec. 2.2) it is possible to make an absolute calibration of the measured potential with good accuracy by determining the amplitude of a soliton from its experimental Mach number.

Fig. 18 shows the plasma response for an applied amplitude, ϕ_a, smaller than the critical potential, ϕ_c, so that the electron hole was not excited (see Sec. 2.2). We note the overall similarity of the experimental results to the direct numerical solutions of Eq. (20). We thus observe that the pulse damps as a trailing plateau develops with a length proportional to t, followed by an oscillatory, rapidly damped tail, in full agreement with the theoretical results in Sec. 4.1 and the numerical solutions in Sec. 4.2.

The spatial damping of the soliton is shown in Fig. 19 for three different initial soliton amplitudes. The ordinate is given in units of v^2, where the absolute value of the poten-

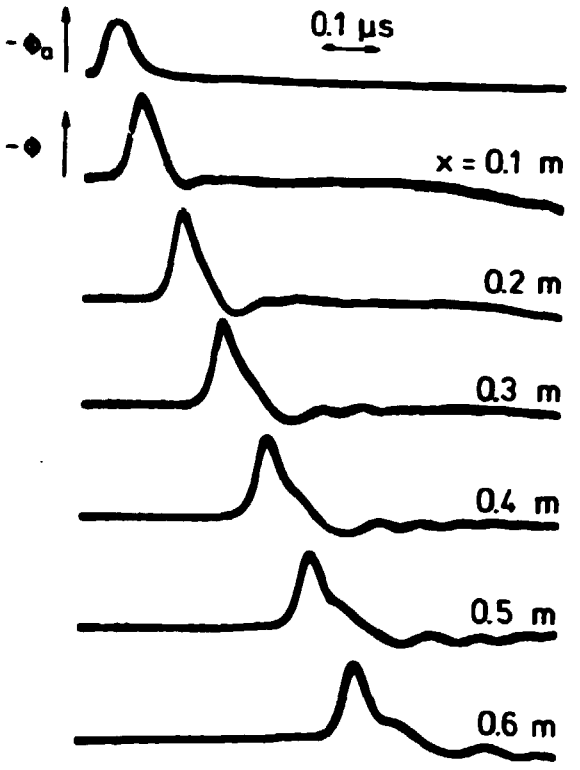

Fig. 18. Oscilloscope traces showing the soliton damping and the development of the plateau and the oscillatory tail. The applied potential, ϕ_a, and the measured potential, ϕ, are in arbitrary units.

tial was determined by the procedure mentioned above. Since $C_o/v_t \sim 2.7$ corresponding to $\omega_p a/v_t \sim 2.4$ the condition $\tau_s/\tau_p << 1$ for application of the perturbation theory is not fulfilled (see Fig. 11). Nevertheless, an illustrative theoretical damping is calculated and plotted assuming $f_o(v)$ to be a single Maxwellian with $T_e = 0.2$ eV corresponding to the hot plate temparature. It should, however, be noted that the soliton is travelling "upstream", and although the "downstream" part of the electron distribution is well-approximated by this assumption, we have to rely on specular reflection at the exciter to form a full Maxwellian distribution. (Obviously, it is not possible to measure the actual form of the upstream part of the electron velocity distribution). Contrary to all these imperfections we see that the agreement between theory and experi-

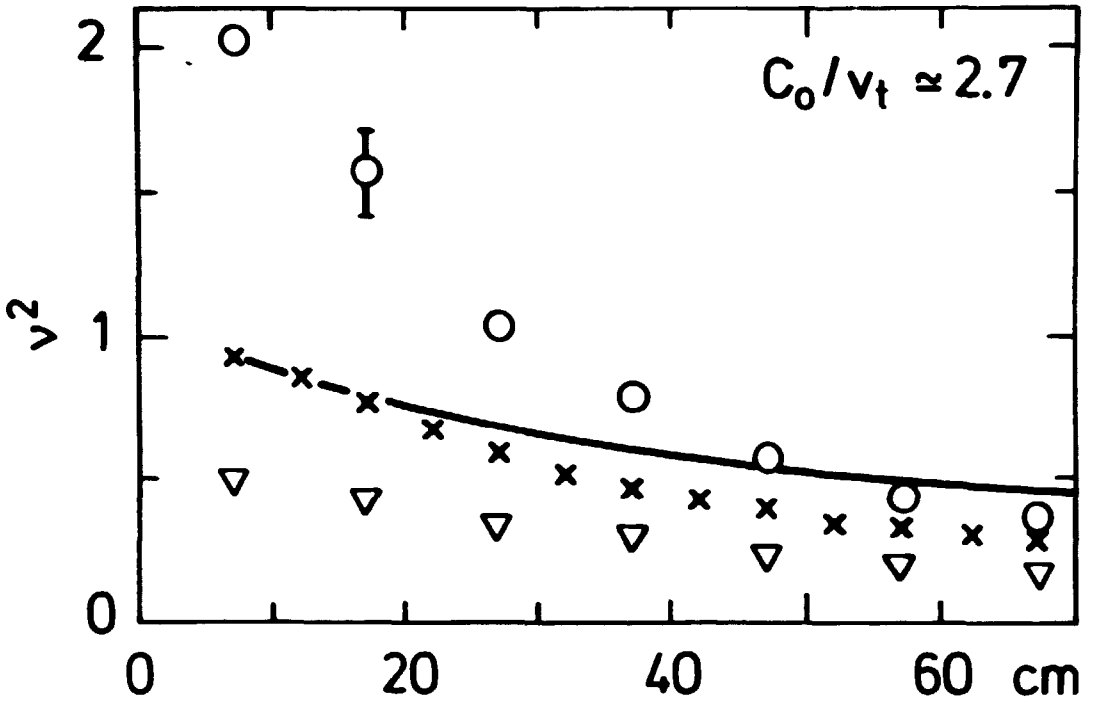

Fig. 19. Experimental results showing the soliton damping for different initial amplitudes. The solid line corresponds to the theoretical damping assuming a Maxwellian distribution.

ment is rather good, which is even more convincing considering that the theoretical line is based on absolute calculations. For the lowest radial mode considered here, deviations from a flat density profile (assumed in the theoretical analysis) do not seem to be important.

4.4. Simulation

In order to avoid some of the imperfections of the experiment for the application of the results obtained by the perturbation analysis, numerical simulations based on the scheme described in Sec. 3 were very useful, since the initial velocity distribution function, $f_0(v)$, was known to be a full Maxwellian and since the simulations could be performed in a parameter range where the theoretical assumptions were more accurately fulfilled.

The result of a simulation for the case of $C_o/v_t = 4.14$ ($\omega_p a/v_t = 3.96$) is shown in Fig. 20. The spatial potential variation shown in Fig. 20b is plotted in the frame of reference moving with the linear phase velocity, C_o. The soliton, when it is fully developed after the excitation at approximately $t\omega_p/2\pi = 3$, has an amplitude $U_o/(\omega_p a)^2 = 0.25$ so that the parameters in this case are only slightly larger ($\tau_s/\tau_p \sim 0.7$) than those in Fig. 13. Again we see a fine qualitative agreement between the perturbation analysis of the model equation and the actual development of the potential in a "physical" system, since the soliton is damped, while producing a tail consisting of a plateau, with length proportional to t, followed by an oscillatory part. In the phase space plot in Fig. 20a, corresponding to the potential at $t\omega_p/2\pi = 12$, we clearly see the electrons reflected by the soliton producing a precursor with velocity approximately twice the soliton velocity. Note, however, that the potential of the precursor in Fig. 20b scarcely can be distinguished from the background noise (inherent in a particle simulation with random initial distribution) while the plateau easily can be identified. This agrees with the discussion in Sec. 4.1.4. It should be mentioned that the electron hole was also excited in this simulation, but, for the sake of clarity, we have omitted the hole, which falls outside the area designated by the thick potential curves in Fig. 20b.

From several simulation runs we have measured the soliton velocity as a function of its amplitude, and since the absolute values of the potential naturally are known, it is possible to compare these measured velocities with the theoretical fluid velocity of a KdV soliton (16) without any form for fitting. The results for the Mach number, $M = v_{ph}/C_o$, versus soliton amplitude are shown in Fig. 21. We see that the agreement is very good, considering that the kinetic corrections from the resonant electrons cause an increase of the soliton velocity at high amplitudes due to the plateau and the even part of the number of resonant electrons, N_2 (see Eq. 44 and the figures of the directly calculated potentials from the model equation in Sec. 4.2). The ideal behaviour with soliton velocity proportional to soliton amplitude is, obviously, correct only for

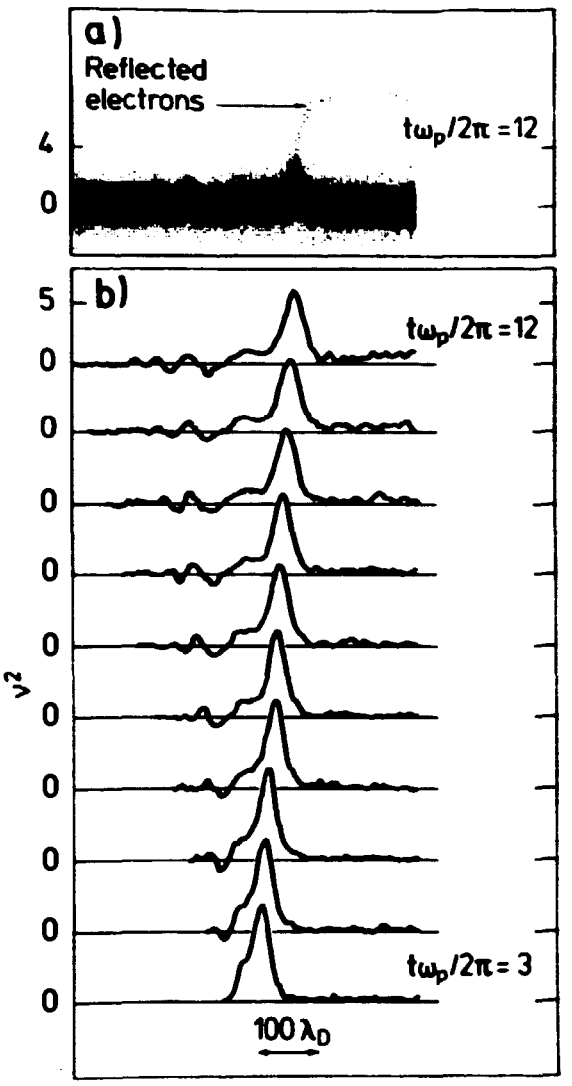

Fig. 20. Numerical simulation results showing the evolution of the perturbed soliton shown in a frame of reference moving with C_o, where $C_o/v_t = 4.14$; (a) phase space and (b) potential.

one fully developed soliton (Berezin and Karpman, 1966). Both experiment and simulation exhibit the dynamics of soliton formation, and as a general trend the high amplitude electron pulses reach the soliton form faster than the low amplitude ones. In the potential plots of the pulse evolution, corresponding to the lowest M value in Fig. 21, it can be seen that the transition to a fully developed soliton is not yet com-

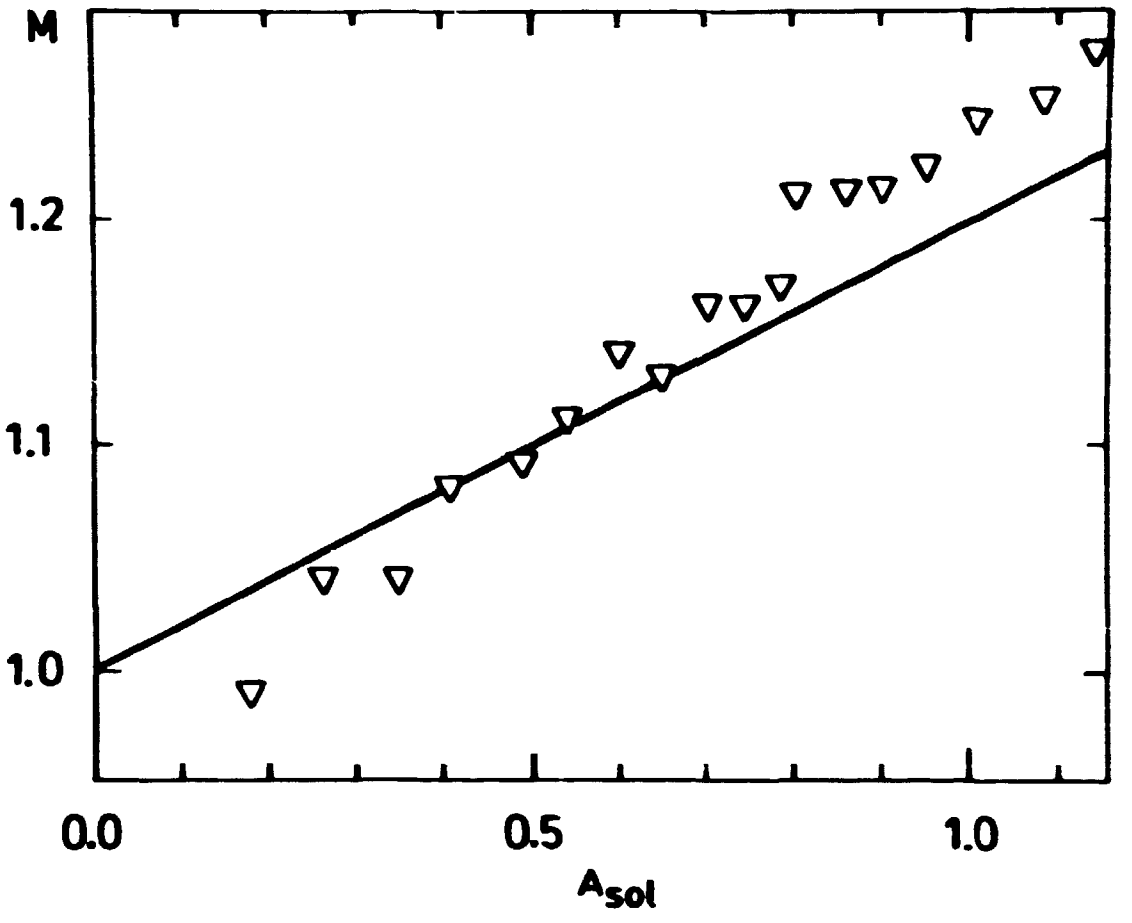

Fig. 21. Numerical simulation results for the soliton Mach number ($M = v/C_o$) versus the soliton amplitude, A_{sol}, which is normalized by $\frac{1}{2}m(\omega_p a)^2/e$. The solid line shows the theoretical relation (16).

pleted during the time of the simulation, giving rise to a poor agreement between the theoretical and measured Mach number (note that the pulse velocity is even smaller than C_o).

The temporal damping of the soliton was also measured for different amplitudes and linear phase velocities, and the results are shown in Fig. 22. The agreement between the simulation results for v(t) and the theoretical damping, shown by the solid lines, is very high, especially for the lower values of the initial amplitudes. The discrepancy between the measured and the theoretical damping at the highest amplitudes shown in Fig. 22

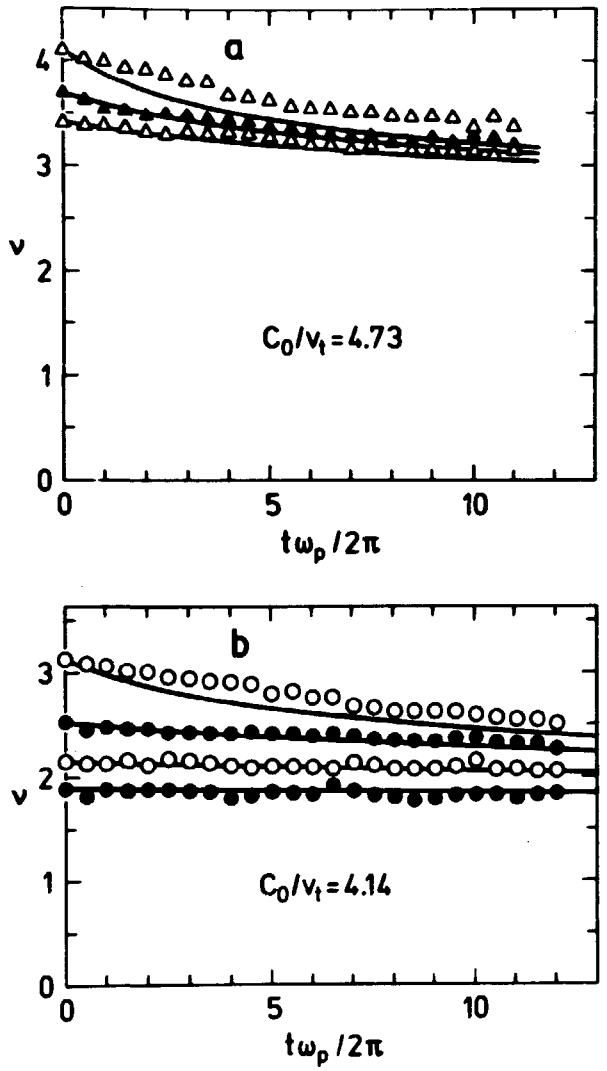

Fig. 22. Numerical simulation results of the soliton damping for different initial amplitudes with (a) C_o/v_t = 4.73 ($\omega_p a/v_t$ = 4.57) and (b) C_o/v_t = 4.14 ($\omega_p a/v_t$ = 3.96). The solid lines indicate the theoretical dependence.

is not surprising, since τ_s/τ_p, which as mentioned previously (Sec. 4.1.3) should be the basic small parameter in the perturbation analysis, takes the value 0.8 and 0.9 for the highest amplitude shown in Figs. 22a and 22b, respectively (see Fig. 11).

The measured ratio of plateau height to soliton amplitude is compared with perturbation theory in Fig. 23, and we observe

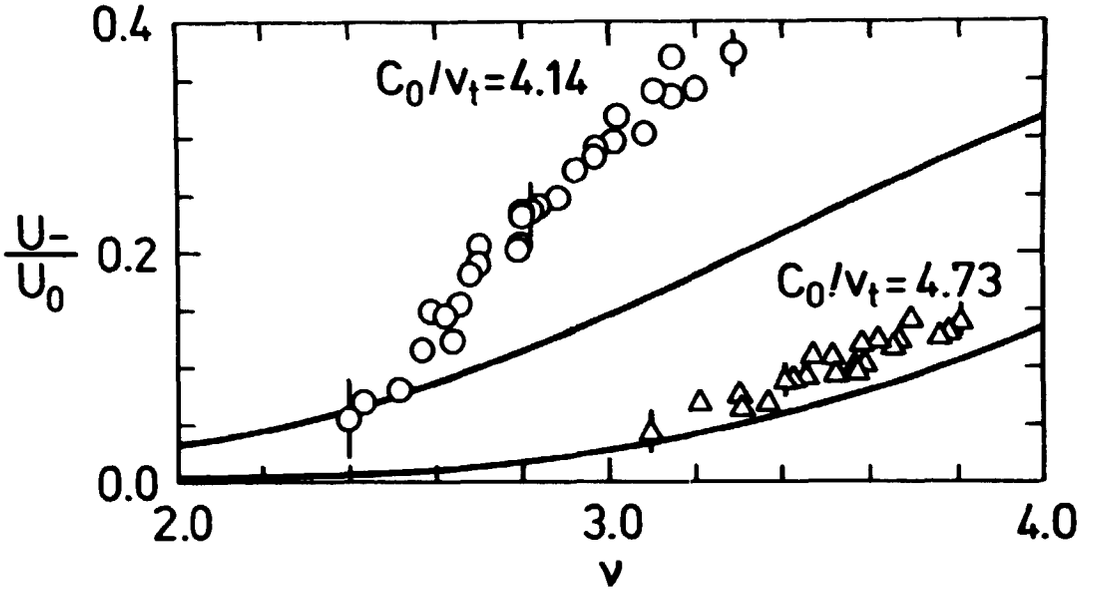

Fig. 23. Numerical simulation results of the relative plateau amplitude U_-/U_0 as a function of v. The solid line indicates the theoretical dependence.

the same behaviour as in the case of the direct numerical solutions of the model equation in Sec. 4.2, namely, that a close agreement between the measured values of U_-/U_0 and the theoretical predictions is achieved for only very low soliton amplitudes. As in Sec. 4.2, this discrepancy is not primarily caused by a high value of τ_p/τ_s, but rather due to the inability of the plateau amplitude to be measured until a time that is close to or even larger than the upper time limit, t_{max}, for applicability of the perturbation analysis (see Eq. 46). It should be mentioned that in the calculations of the theoretical curve, shown in the figures in this section, the value of the parameter α (see Sec. 4.1.1) was put equal to 1 in agreement with the "physics" of the simulation code (Turikov, 1978a,b).

5. THE ELECTRON HOLE

In the brief presentation of the general results from the numerical simulations (Sec. 3.2), we noted that the appearance of the electron hole in the phase space plots is a distinct vortex. This indicates that the electron hole is a purely kinetic phenomenon, containing a large number of trapped electrons, in clear contrast to the Trivelpiece-Gould soliton which is basically a fluid phenomenon.

Bernstein, Green and Kruskal (1957) have shown that stationary electrostatic waves or pulses of arbitrary shape can exist in a plasma, as long as the distributions of the trapped particles are taken into account. Such, more or less complete, Bernstein-Green-Kruskal (BGK) equilibria have been observed in computer simulations of the electron two-stream instability (Roberts and Berk, 1967; Morse and Nielsen, 1969a,b), where vortex structures in the phase space were also clearly seen. However, our investigations are to our knowledge the first experimental demonstration of the formation of single-pulse, or solitary, BGK equilibria.

5.1. Theory

The BGK approach to a close investigation of the electron hole is not very fruitful, since it provides a method for calculating the distribution of the trapped electrons, once the distribution of the untrapped electrons and shape of the potential is known, but it imposes no restrictions upon this potential, which can take any form whatsoever. A different approach can be used, by making assumptions concerning the dependence of the distribution functions of the trapped and untrapped electrons on the potential. Then, the shape of the potential can be calculated using the assumed relations. Such an approach has been made by Schamel (1979), who used special types of modified Max-

well distributions for the trapped and untrapped particles. (A different analysis has very recently been performed by Krapchev and Ram (1980)). Schamel's theory may provide a good description of the electron hole, but the results of the complete calculations are so complicated that a comparison with the results from the experiment and the simulation can be performed only by calculating the theoretical expressions on a large digital computer. To simplify his equations, Schamel made a small amplitude expansion of the complete solution and found, for instance, that the hole width decreases with increasing hole amplitude in contradiction with our results. However, the amplitudes of the electron hole in the experiment and the simulation were not at all small in Schamel's sense, since the values of $e\phi_h/T_e$ were larger than 1; ϕ_h being the amplitude of the hole.

Instead of performing the rather involved numerical computation of Schamel's complete solution, we will present some electron hole calculations based on a simple, single "waterbag" theory. Our analysis is similiar to the calculations by Berk, Nielsen, and Roberts (1970a) of the equilibrium of a one-dimensional electron hole in an unbounded plasma. We, naturally, take into account the finite radial geometry in our experiment, and we also derive some restrictions on the hole equilibrium as consequences of the single waterbag approach.

In the single waterbag model, the plasma is assumed to have an unperturbed distribution function, f(v), which is a constant, b, within the limits $-v_o < v < v_o$ and zero outside. The value of b is easily determined since $\int_{-\infty}^{\infty} f(v)dv = n_o$, so $b = n_o/2v_o$. Defining the thermal velocity, v_t, in the same way as for a Maxwellian distribution, we find

$$v_t^2 = 2 \int_{-\infty}^{\infty} v^2 f(v)dv / \int_{-\infty}^{\infty} f(v)dv = \frac{2}{3} v_o^2 . \qquad (53)$$

Since the collisionless Vlasov equation, which we use to describe the plasma, expresses that f(v) acts like an incompressible fluid in the phase space, the only possible values of $f(x,t,v)$ are 0 and $n_o/2v_o$. Furthermore, since regions in phase space that initially are close to one another will continue to

be close, the distribution function is fully described by the position of boundary curves of the initial distribution. It is, naturally, this behaviour which gave name to the "waterbag" model (de Packh, 1962; Berk and Roberts, 1970b).

For the determination of the hole equilibrium, we choose to work in a reference system where the hole is at rest and where $x = 0$ corresponds to the hole maximum (see Fig. 24, where we note that the potential as usual is drawn with positive values in the downwards direction). In order to model a hole, the boundary velocities v_i, $i = 1\text{-}4$, are introduced, as shown in Fig. 24a. Here v_1 and v_4 correspond to the outer boundaries of the untrapped particles ($v_1 > v_4$), while v_2 and v_3 correspond to the inner boundaries of the trapped particles ($v_2 > v_3$). In the chosen reference system, the velocity distribution must satisfy the time-independent Vlasov equation

$$v \frac{\partial f(x,v)}{\partial x} - \frac{\partial U}{\partial x} \frac{\partial f(x,v)}{\partial v} = 0 , \tag{54}$$

where f as usual is the "effective distribution function" $f(x,v) = \alpha(\bar{f}(x,v) + f_o(v)/\alpha)$, and $U = -\alpha e\phi/m$ (see Eqs. (4)-(7)). The general solution to Eq. (54) is

$$f(x,v) = f(E) , \tag{55}$$

where the total energy,

$$E = \frac{1}{2} v^2 + U . \tag{56}$$

The solution (55) may be checked by direct insertion into Eq. (54). Since Eq. (56) must be fulfilled for all v, it must also hold for the v-boundaries, so that

$$\frac{1}{2} v_i^2 + U = E_i , \qquad i = 1,2,3,4, \tag{57}$$

where E_i is a constant depending on i. With the choice of $U = 0$ at $|x| = \infty$ and $U < 0$ at $x = 0$, the values of E_i are negative for the trapped boundaries and positive for the untrapped. Since

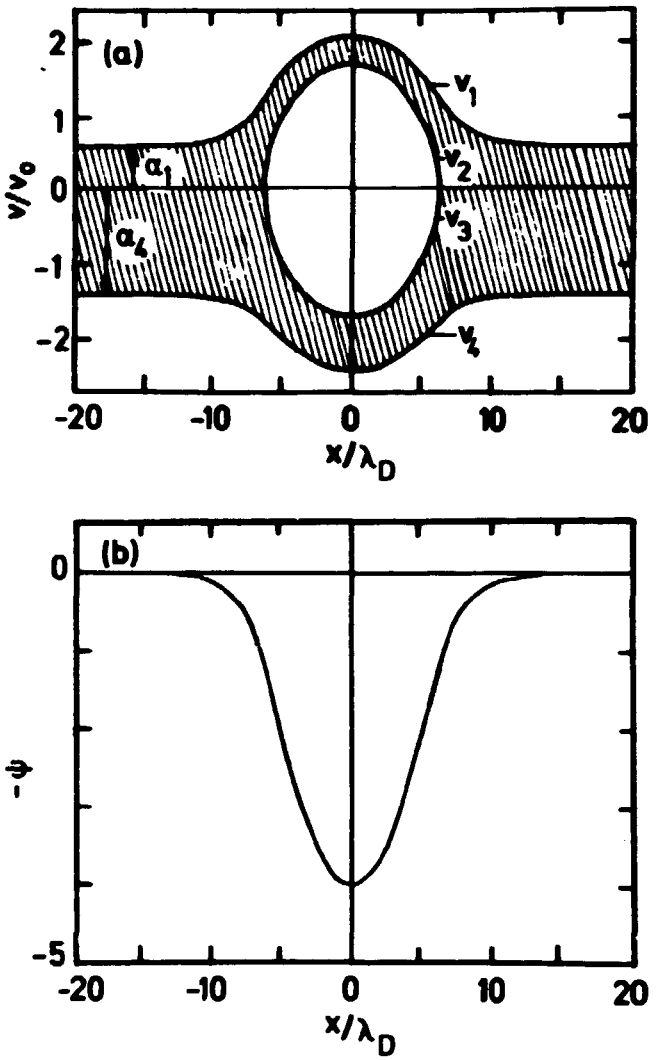

Fig. 24. Waterbag hole-equilibrium. (a) The phase space boundaries and (b) the corrsponding potential, for $\omega_p a/v_t = 4$, $\psi_o = 4$, and $M_h = 0.5$, where ψ is the normalized potential, see (64), and M_h the hole's Mach number, see (72).

the trapped boundaries must connect at $v = 0$, E_3 is equal to E_2, so $v_3 = -v_2$. Poisson's equation (8) takes the form

$$\frac{\partial^2 U}{\partial x^2} - k_\perp^2 U = -\omega_p^2 \left(\sum_{i=1}^{4} \frac{\Delta f_i v_i}{2v_o} - 1 \right), \tag{58}$$

where $\Delta f_1 = \Delta f_3 = +1$, $\Delta f_2 = \Delta f_4 = -1$, and $k_\perp = 1/a$ is the perpendicular wavenumber of the electric field in the waveguide.

Following Berk et al. (1970), we can estimate the behaviour of U outside the region of $v_{2,3}$, in which the space charge is positive. Assuming that

$$\frac{v_{1,4}^2}{2} >> |U(x)| ,$$

then

$$v_{1,4} = \pm(2E_{1,4})^{1/2}\left(1 - \frac{U(x)}{2E_{1,4}}\right), \tag{59}$$

where the upper sign corresponds to v_1 and the lower to v_4. Substitution of (59) into (58) and cancellation of the first term in (59) by the neutralizing background, yields

$$\frac{\partial^2 U}{\partial x^2} - k_{eff}^2 U = 0 , \tag{60}$$

where

$$k_{eff}^2 = k_\perp^2 + \frac{\omega_p^2}{2v_o}\left(\frac{1}{v_1} + \frac{1}{|v_4|}\right). \tag{61}$$

Equation (60) expresses the form of an exponentially shielded potential. We can estimate the last term in (61) by putting $v_1 = v_4 = v_o$. Then (61) becomes

$$k_{eff}^2 = k_\perp^2 + \frac{1}{12\pi^2} k_D^2 , \tag{62}$$

where $k_D^2 = (2\pi)^2/(v_t^2/2\omega_p^2)$ is the squared Debye wavenumber. We expect two electron holes to be effectively shielded from each other as long as their mutual distance, Δx, satisfies $\Delta x >> 1/k_{eff}$ (see Sec. 6.2).

By inserting (57) into (58), we obtain

$$\frac{\partial^2 U}{\partial x^2} \equiv \frac{1}{2}\frac{\partial}{\partial U}\left(\frac{\partial U}{\partial x}\right)^2 = -\frac{\omega_p^2}{2v_o}\left\{(2E_1-2U)^{\frac{1}{2}} + (2E_4-2U)^{\frac{1}{2}} - 2(2E_2-2U)^{\frac{1}{2}}\cdot\theta(2E_2-2U)-2v_o\right\} + k_I^2 U \ , \quad (63)$$

where $\theta(x) = 1$ for $x > 0$ and $\theta(x) = 0$ for $x < 0$. We now introduce the dimensionless variables

$$\psi = -\frac{2U}{v_o^2}\left(= \frac{2}{3}\alpha\frac{2e\phi}{mv_t^2}\right), \quad y = \frac{\omega_p x}{v_o} \ ,$$

$$K^2 = \frac{v_o^2 k_I^2}{\omega_p^2}\left(= \frac{3}{2}\left(\frac{v_t}{\omega_p a}\right)^2\right), \quad \alpha_1 = \left(\frac{2E_1}{v_o^2}\right)^{\frac{1}{2}} \ ,$$

$$\alpha_4 = -\left(\frac{2E_4}{v_o^2}\right)^{\frac{1}{2}} , \quad \alpha_2 = \left(\frac{-2E_2}{v_o^2}\right)^{\frac{1}{2}} . \quad (64)$$

Substitution of these variables into (63) and integration over ψ, yields

$$\left(\frac{d\psi}{dy}\right)^2 = -V(\psi) \ , \quad (65)$$

where

$$V(\psi) = -\frac{4}{3}\left\{(\alpha_1^2+\psi)^{3/2}-(\alpha_1^2+\psi_o)^{3/2}+(\alpha_4^2+\psi)^{3/2}-(\alpha_4^2+\psi_o)^{3/2}-2(\psi-\alpha_2^2)^{3/2}\theta(\psi-\alpha_2^2)+2(\psi_o-\alpha_2^2)^{3/2}-3(\psi-\psi_o)+\frac{3}{4}K^2(\psi^2-\psi_o^2)\right\} \ . \quad (66)$$

Here, ψ_o is the hole amplitude which lies in $y = 0$. The function $V(\psi)$ is often called the Sagdeev potential due to the resemblance of (65) to the equation of motion for a particle,

where ψ is equivalent to the position, y to the time and $V(\psi)$ to the potential in which the particle is moving (Sagdeev, 1963).

Equation (66) insures that $V(\psi) = 0$ for $\psi = \psi_o$, but it is also necessary that $V(\psi) = 0$ for $\psi = 0$. This requirement gives us an equation for α_2

$$\alpha_2^2 = \psi_o - (\tfrac{1}{2})^{2/3} \left[(\alpha_1^2+\psi_o)^{3/2} - |\alpha_1|^3 + (\alpha_4^2+\psi_o)^{3/2} - |\alpha_4|^3 - 3\psi_o + \tfrac{3}{4} K^2 \psi_o^2 \right]^{2/3} . \qquad (67)$$

Furthermore, since we wish to investigate only a single hole and not an infinite wave train, we must require $dV(\psi)/d\psi = 0$ for $\psi = 0$. This implies that

$$|\alpha_1| + |\alpha_4| = 2 . \qquad (68)$$

Now, for $y >> 1$ the potential $\psi << \psi_o$, so from (57) we find that

$$v_1 = (2E_1)^{\frac{1}{2}} , \; v_4 = -(2E_4)^{\frac{1}{2}} , \qquad \text{for } |y| >> 1 . \qquad (69)$$

In the unperturbed plasma, for $|y| >> 1$, we know that $v_1 - v_4 = 2v_o$, so (69) gives (see Fig. 24a)

$$\alpha_1 + \alpha_4 = 2 . \qquad (70)$$

Substitution of α_4 from (70) into (68) yields the restriction

$$0 \leq \alpha_1 \leq 2 . \qquad (71)$$

Introducing the hole Mach number, M_h, as the hole velocity, v_h, relative to the plasma divided by v_t,

$$M_h = v_h/v_t = (1-\alpha_1)\cdot(3/2)^{\frac{1}{2}} , \qquad (72)$$

Eq. (71) imposes upon M_h the restriction

$$-(3/2)^{\frac{1}{2}} \leq M_h \leq (3/2)^{\frac{1}{2}} . \qquad (73)$$

The Sagdeev potential can now be calculated by choosing three free parameters, which can be ψ_o, M_h and $\omega_p a/v_t$. K^2 can then be found from (64), α_1 from (72), α_4 from (70) and α_2 from (67). In Fig. 25, $V(\psi)$ is shown for $\psi_o = 4$, $M_h = 0.5$, and $\omega_p a/v_t = 4$. Once $V(\psi)$ is found, we can find $y(\psi)$ from (65) as

$$y(\psi) = \pm \int_{\psi_o}^{\psi} [-V(z)]^{-\frac{1}{2}} \, dz \, . \tag{74}$$

The boundaries of the waterbag in phase space can then be determined from Eq. (57), and Fig. 24 actually shows the results for the same parameters as in Fig. 25. The calculations were easily carried out on a desk computer (HP-9825) and the integration of (74) was performed by using the trapezoidal method on the 200 ψ-positions in which $V(\psi)$ was calculated. The first y position closest to y = 0 was determined by analytical expansion of the right-hand side of (74) for $(\psi_o - \psi) \ll 1$.

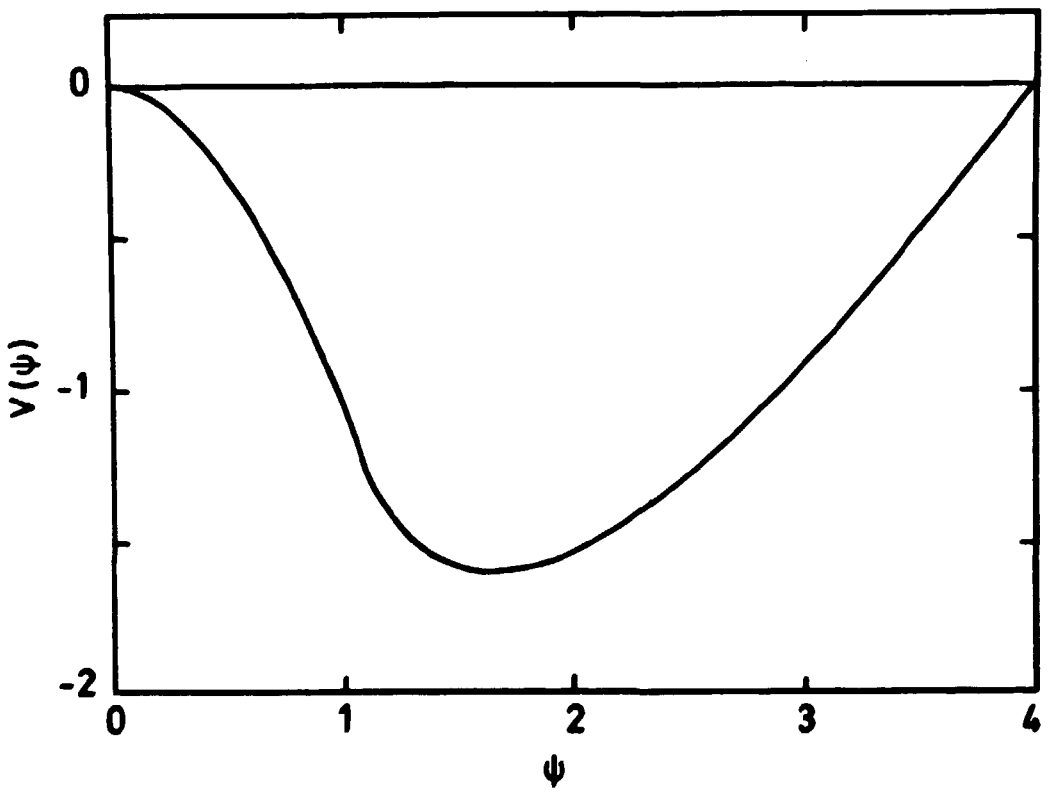

Fig. 25. The Sagdeev potential $V(\psi)$ for $\omega_p a/v_t = 4$, $\psi_o = 4$, and $M_h = 0.5$.

The three free parameters cannot be chosen completely arbitrarily. We have already seen that (73) imposes a restriction on M_h, but, furthermore, the parameters, naturally, must ensure that $dV(\psi)/d\psi > 0$ for $\psi = \psi_o$. This yields the requirement that

$$(\alpha_1^2+\psi_o)^{\frac{1}{2}}+(\alpha_4^2+\psi_o)^{\frac{1}{2}}-2(\psi_o-\alpha_2^2)^{\frac{1}{2}}-2+K^2\psi_o < 0. \qquad (75)$$

For given values of K^2 and M_h, Eq. (75) can be shown to imply $0 < \psi_o < \psi_{max}(K^2,M_h)$. The function $\psi_{max}(K^2,M_h)$ is shown in Fig. 26 for $M_h = 0$ and $\sqrt{3/2}$, and we see that the M_h-dependence is rather weak, whereas the K^2-dependence is significant, giving no restriction on ψ_{max} in the infinite plasma ($K^2 = 0$), but allowing only a continuously decreasing value of ψ_{max} as K^2 increases

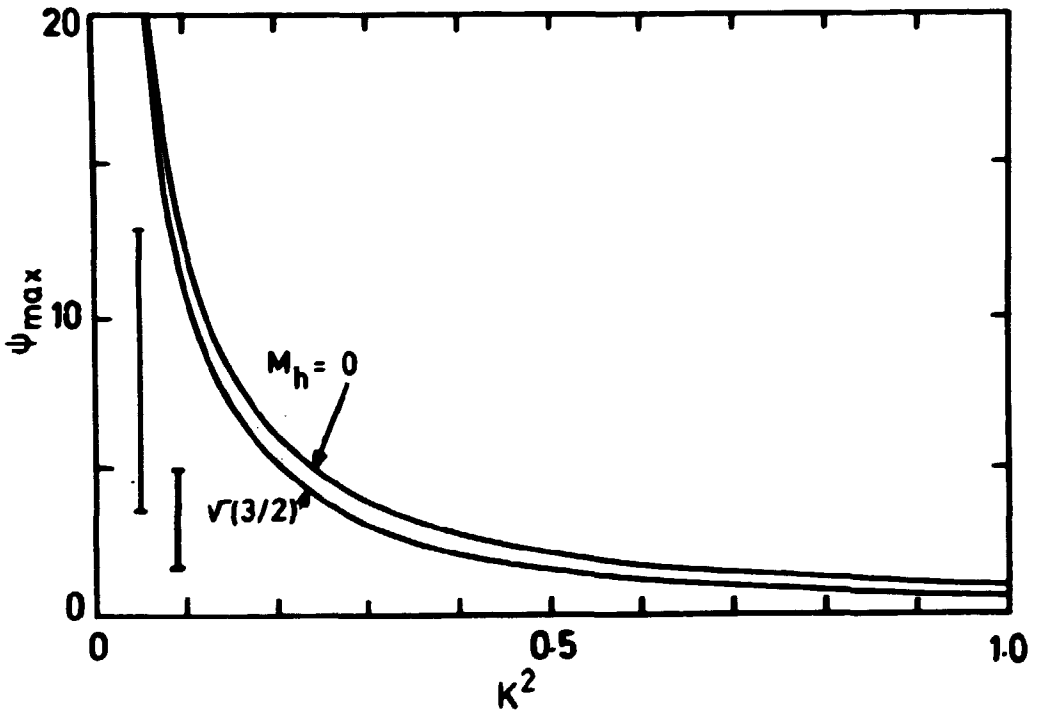

Fig. 26. The hole-equilibrium criterion $\psi_{max}(K^2,M_h)$. The two vertical bars indicate the observed values of ψ_o in the numerical simulations, Sec. 5.3. The bar at the lowest value of K^2 corresponds to $T_e = 0.4$ eV while the other corresponds to $T_e = 0.2$ eV.

(r_o/λ_D decreases). There is no lower bound, however, for the value of r_o/λ_D as long as the hole amplitude is small enough. On this point the waterbag equilibrium theory also contrasts Schamel's (1979) small amplitude limit of the "modified Maxwellian" hole theory, since Schamel arrives at $r_o/\lambda_D \sim 5$ as a lower bound of the waveguide radius in order to sustain electron holes.

So far, we have only considered the equilibrium of a fully developed electron hole. The question of stability of this equilibrium is, naturally, more complicated. Kako, Taniuti, and Watanabe (1971) have performed a stability analysis of the evolution of two cold, counterstreaming electrons beams into a train of holes, but their stability analysis is not well suited for discussing the stability of fully developed holes. A stability analysis of a periodic BGK wave consisting of complete electron holes has been performed by Schwarzmeier, Lewis, Abraham-Schrauner, and Symon (1979), and as a result they found that the BGK wave is stable against perturbations with wavelengths shorter than the wavelength of the BGK wave, thus indicating that the solitary electron hole is a stable structure. Naturally, the stability analysis was based on the collisionless Vlasov equation, and one should expect the hole to be extremely sensitive to collisions, which can scatter the trapped electrons out of their closed orbits in phase space, thereby disintegrating the structure of the hole. Schwarzmeier et al. (1979) also showed that perturbations of the BGK wave with wavelengths longer than the width of a single hole could cause neighbouring holes to coalesce, an effect to which we shall return in Sec. 6.

Morse and Nielsen (1969b) and Berk et al. (1970a) have shown that a one-dimensional system, which we virtually have in our case due to the strong magnetic field, is necessary for the stability of electron holes that hardly can exist in higher dimensions.

The properties of a fully developed electron hole observed in the experiment or the simulation shall, of course, be within any physical bounds that are imposed by the requirements for a nonlinear equilibrium. Approximations to such bounds have just been derived by use of the simple waterbag method. However, the range

of observed hole quantities can also be limited by the excitation mechanism. The determination of these limits is no simple task due to the complex nature of the hole excitation. In Fig. 27 results are shown from a waterbag simulation of our experiment (Saeki et al., 1979). The phase space plot marked I in Fig. 27b is shown at a time (t/τ_p = 0.8; τ_p being the plasma period) while the exciting potential (which lasted $1\tau_p$) was still applied. We note the complicated structure of the waterbag. The "arm" moving in the negative x-direction consists of electrons that are accelerated through the external potential and reflected from the "newborn soliton". As mentioned in Sec. 2.2, it was

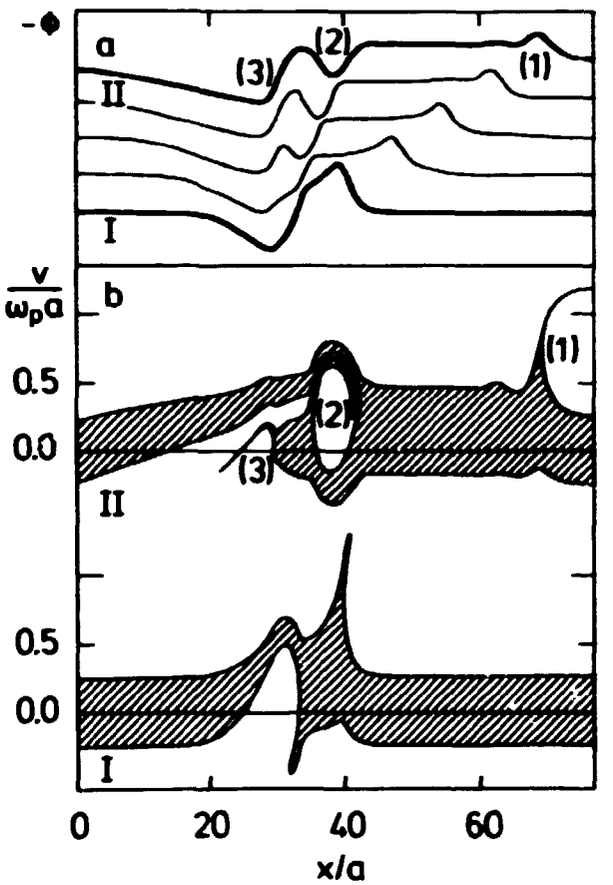

Fig. 27. Waterbag simulation (a) Potential versus position for increasing time (t/τ_p = 0.8, 1.6, 2.4, 3.2 and 4). (b) Waterbag distribution in phase space for times corresponding to the potentials marked I and II in (a).

observed experimentally and confirmed by the waterbag and cloud-in-cell simulations that no hole was created unless the applied potential exceeded a critical potential, ϕ_c, of the order of $\phi_c = \frac{1}{2}m(\omega_p a)^2/e$. Since the equilibrium equations impose no lower bound on the hole amplitude the critical potential must be an excitation effect. A handwaving argument for the existence of ϕ_c is found by presuming that the hole is formed by electron trapping in the rarefaction wave. Since this wave has a negative velocity, approximately equal to the linear phase velocity $\omega_p a$, one must require of its amplitude, ϕ_r, in order to trap a significant amount of electrons that

$$-\omega_p a + \left(\frac{2e\phi_r}{m}\right)^{\frac{1}{2}} > -v_t \ . \tag{76}$$

In our experiment we have approximately $\omega_p a >> v_t$, and equating ϕ_r to the applied potential in (76) yields a value of ϕ_c equal to $\frac{1}{2}m(\omega_p a)^2/e$. The generation of the electron hole may, on the other hand, be caused by other effects, e.g., a kind of two-stream instability between the main plasma and the "arm" with negative velocity. At least, the formation of the electron hole resembles the evolution in phase space of the electron two-stream instability found in numerical simulations (Roberts et al., 1967; Morse et al., 1969a,b). A thorough investigation of the dynamics of the hole formation is, however, outside the scope of this report.

5.2. Experiment

As already mentioned in the presentation of the basic experimental observations (Sec. 2.2), the electron hole was excited when the applied potential, ϕ_a, exceeded a critical potential, ϕ_c (see Fig. 3). The value of ϕ_c was close to 1 V corresponding to approximately $\frac{1}{2}m(\omega_p a)^2/e$ with the experimental data inserted. The electron hole, once fully developed, propagated virtually without change of shape (see Fig. 6). It was found that an increase of ϕ_a above ϕ_c first increased the amplitude and width of the hole up to a certain value of ϕ_a and then additional holes with varying amplitudes were excited. This behaviour re-

sembles the evolution of nonlinear, collisionless, electrostatic shocks. Strong electron shocks can be excited by maintaining the applied potential after it has been switched on and as a result, the trailing part of the shock breaks up into large-amplitude oscillations (Saeki, 1973). From computer simulations of ion-acoustic shocks (Sakanaka et al., 1971) such large amplitude oscillations are known to be associated with vortex-like structures in phase space. In our experiment, where the exciting potential is applied during one plasma period, the generation of more than one hole is enhanced by holding the exciting potential at a small negative level after the pulse. We found that almost any shape of the excitation potential developed one or more electron holes provided that ϕ_a exceeded ϕ_c.

No clear relation was observed between the hole amplitude and velocity. Neither in the simple waterbag theory is there a connection between these two quantities, which are free parameters. However, the hole velocity in general increased with the applied potential, but this is most likely an excitation effect. The observed hole velocities in the case of single hole excitation were in the range of v_t and were always smaller than the linear phase velocity, which in our experiments was $\omega_p a \sim 5\ v_t$. This indicates that there, indeed, may be an upper limit of the hole velocities as found by the waterbag theory in Eq. (73).

In Fig. 28 the observed relation between hole width and hole amplitude is shown. We see that the width increases with the amplitude in qualitative agreement with the simple waterbag theory. In the next section we will give a quantitative comparison between the amplitude-width relation found by the waterbag theory and the relation observed in the computer simulation for parameters similar to those in the experiment (see Fig. 33a).

The sensitivity of the hole equilibrium to electron-neutral collisions is demonstrated in Fig. 29. By slowly increasing the neutral pressure with helium, we could entirely destroy the hole structure at even moderate neutral pressures. The damping length for ordinary collisional damping (Franklin et al., 1974) of a Trivelpiece-Gould wave propagating at the hole velocity is ap-

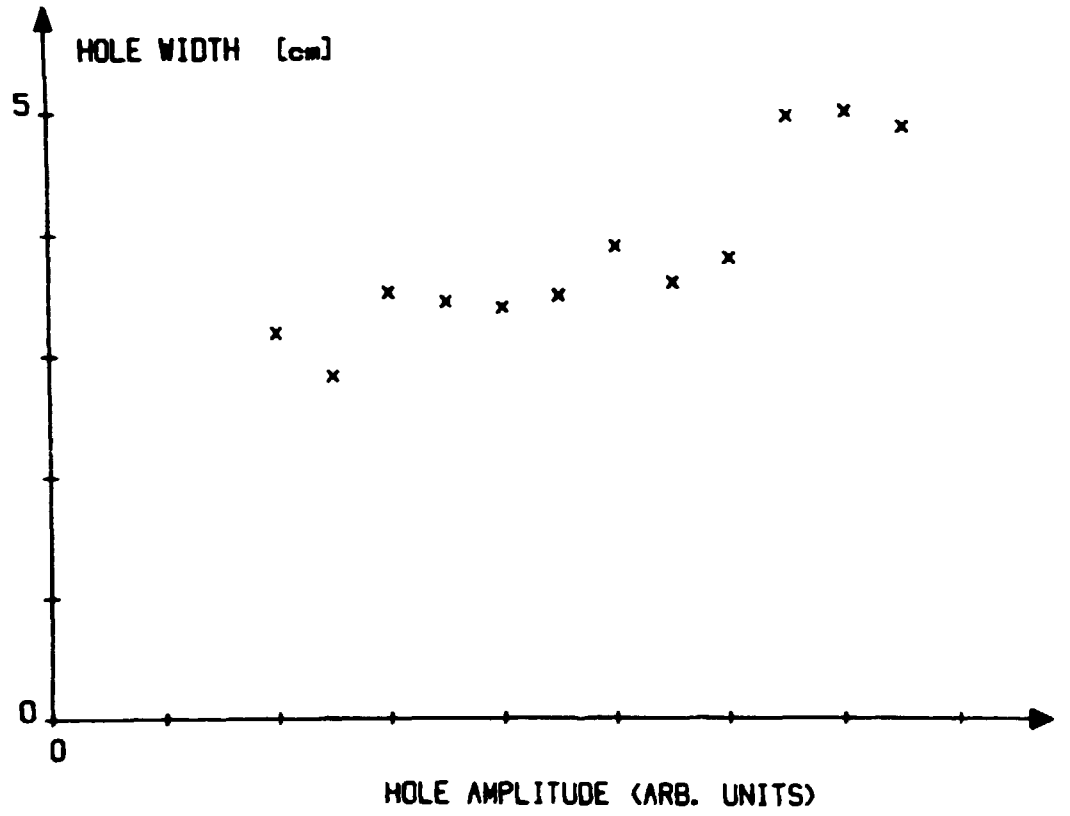

Fig. 28. Experimental hole width versus hole amplitude.

proximately 1.5 m at $5 \cdot 10^{-4}$ mm Hg, thus ruling out that the observed destruction of the hole can be explained by simple collisional damping. Note also that the front of the soliton is only weakly affected by the collisions, as expected.

As mentioned in Sec. 5.1, the high sensitivity of the hole upon electron-neutral collisions is not surprising, due to the importance of a delicate balance between trapped and untrapped particles for the existence of a BGK-equilibrium.

5.3. Simulation

The examples of the cloud-in-cell simulations shown in this section are performed for two different sets of parameters. Both of these have a plasma density, $n_o = 10^7$ cm^{-3}, and a waveguide ra-

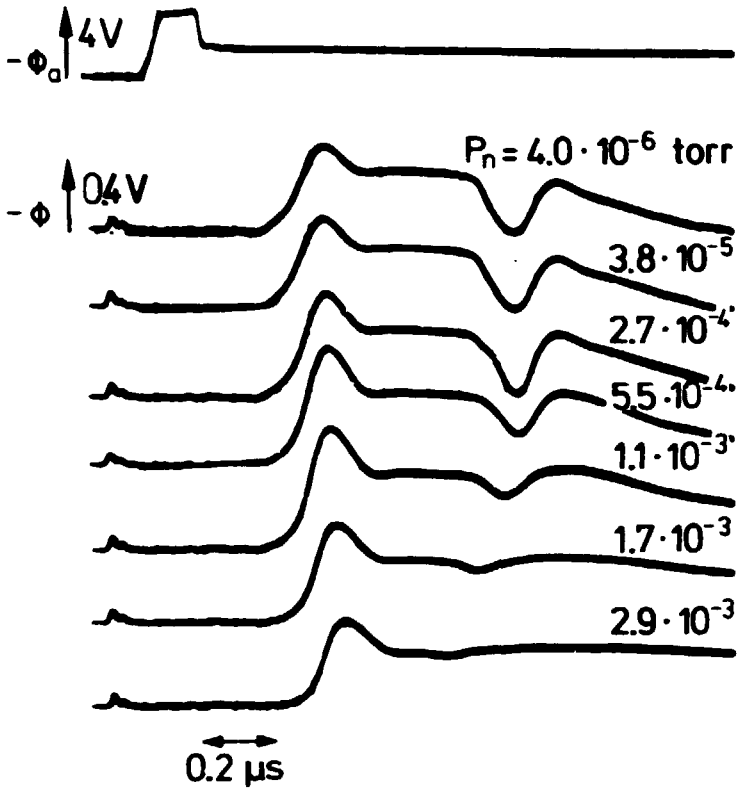

Fig. 29. Destruction of an electron hole by electron-neutral collisions. P_n is the pressure of neutral helium. The position is x = 0.7 m.

dius, r_o = 2 cm. Furthermore, one of the parameter sets has an electron temperature T_e = 0.2 eV, so that the simulations performed under these conditions closely corresponds to experiment, while the other parameter set has T_e = 0.4 eV. The values of $\omega_p a/v_t$ are 5.593 and 3.956 for the parameter set with T_e = 0.2 and 0.4, respectively. Figures 30-32 show some effects by varying the amplitude of the applied potential ϕ_a. In Fig. 30 we show the hole amplitude versus ϕ_a. The normalized amplitude of the electron hole, ψ_o, is defined in agreement with Eq. (64) as $\psi_o = (2/3)\ e\ \phi_h/(\frac{1}{2}mv_t^2)$, where ϕ_h is the maximum hole potential; the value of α is put equal to 1 (as in Sec. 4.4) according to the "physics" of the simulation code (Turikov, 1978a,b). We observe the same behaviour as in the experiment, since no holes are excited as long as ϕ_a is lower than $\phi_c = \frac{1}{2}m(\omega_p a)^2/e$

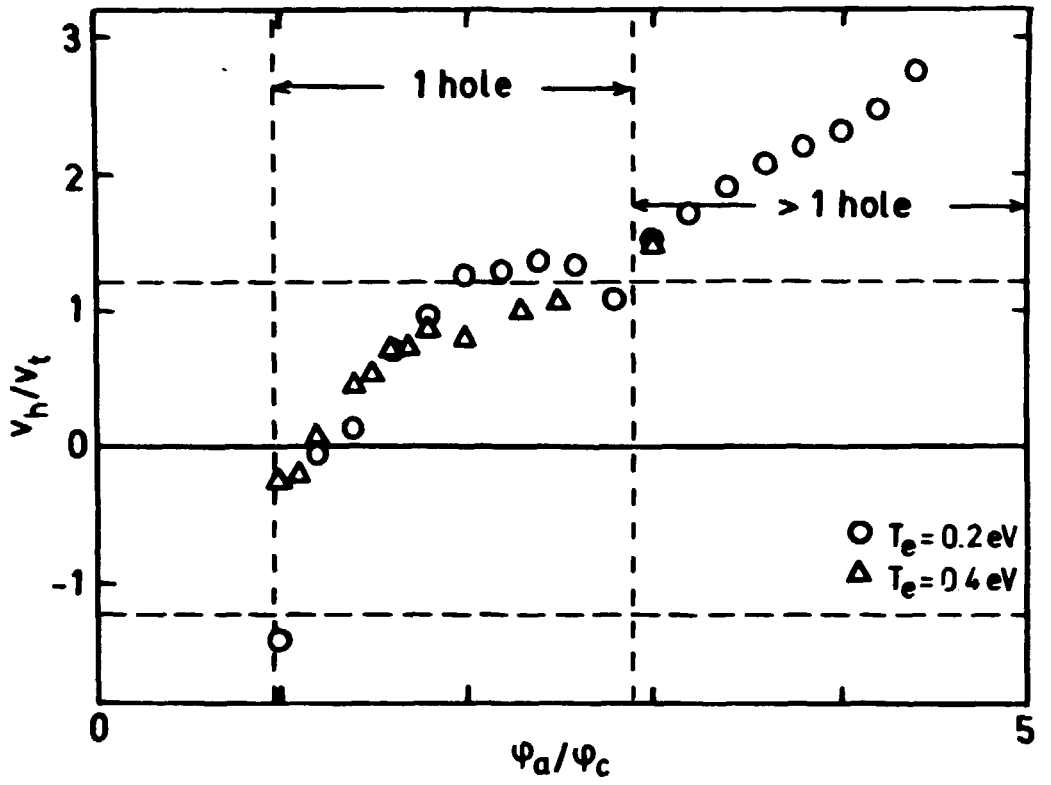

Fig. 30. Numerical simulation results for hole amplitude ψ_o versus the applied potential ϕ_a. The normalization potential, ϕ_c, is $\frac{1}{2}m(\omega_p a)^2/e$.

and since a single hole is produced with an increasing ψ_o as a function of ϕ_a upto a limit of $\phi_a \approx 3\ \phi_c$. Above this limit more than one hole is excited, starting with two holes at $\phi_a = 3\ \phi_c$, which is shown in Fig. 31. The apparent difference between the maximum hole potentials for different values of T_e at a fixed value of ϕ_a is due to the normalization applied in the definition of ψ_o. The total ranges of the observed values of ψ_o for the two different cases are indicated in Fig. 26, and we see that these regions are well within the limits of the area that is "allowed" by the restrictions imposed by the single waterbag equilibrium.

The hole velocity, v_h, is shown against ϕ_a in Fig. 32 and we see that as long as only one hole is excited, the observed velocities are almost limited to the region allowed by Eq. (73)

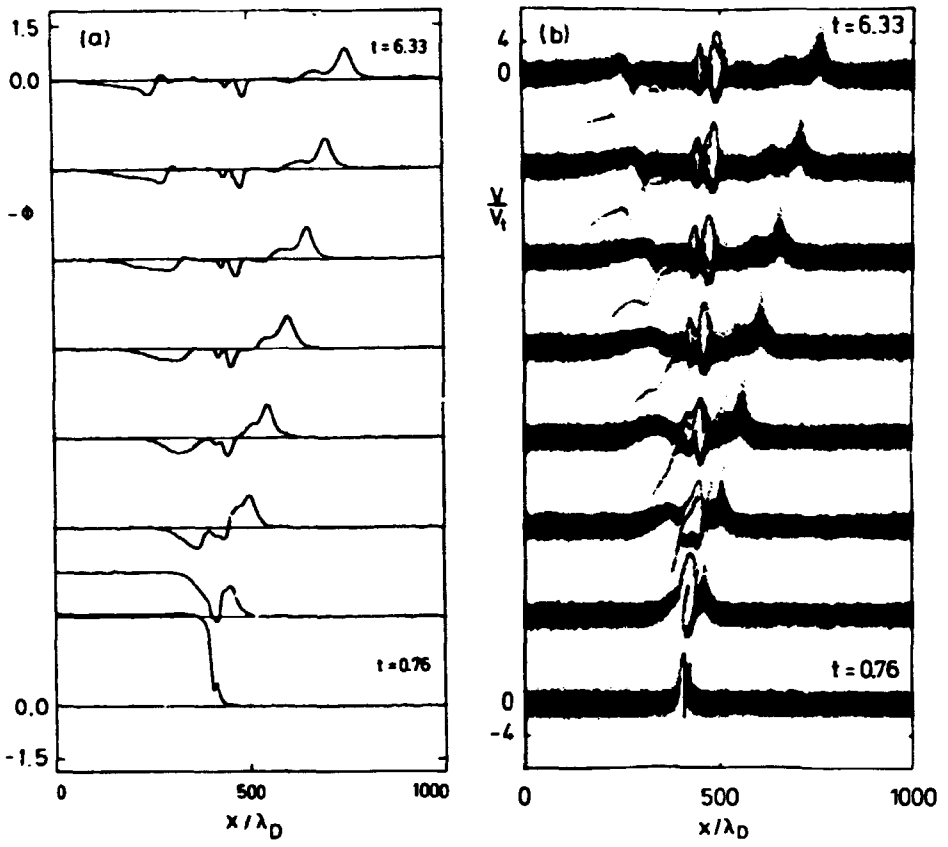

Fig. 31. Same as Fig. 8 for $\phi_a = 3\phi_c$, where $\phi_c = \frac{1}{2}m(\omega_p a)^2/e$.

and indicated by the dashed lines in the figure. When more than one hole exists, Eq. (73) is no longer valid (see the requirement leading to Eq. (68)). By combining Figs. 30 and 32, we see that v_h increases with increasing ψ_o, at least when only one hole is excited, but this behaviour is most likely inherent in the excitation mechanism.

The observed relations between the hole width, Δx_h, and ψ_o are shown in Figs. 33a and b for the two different values of T_e. In this context, the hole width is defined as the total width of the hole potential at $\psi = \psi_o/2$. The results from performances of the integration in Eq. (74) are also shown for the maximum hole velocity $M_h = \sqrt{(3/2)}$ and $M_h = 0$. The other hole velocities fall within the rather narrow region between these two curves. As

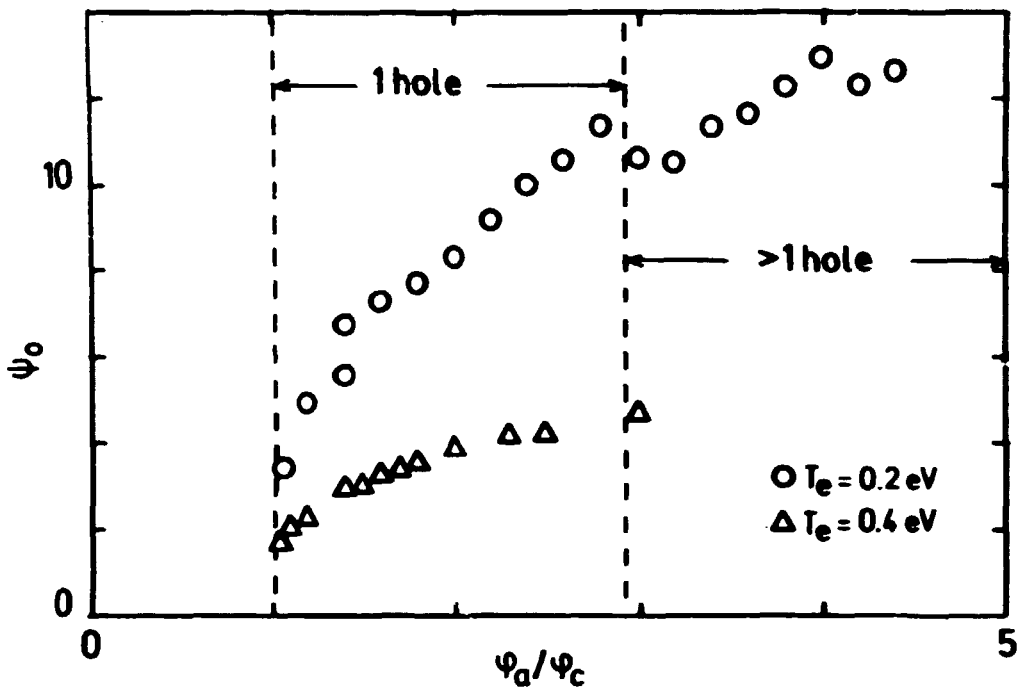

Fig. 32. Numerical simulation results for hole velocity v_h versus applied potential ϕ_a. The horizontal dashed lines indicate the limits on v_h from waterbag theory for a single hole.

a curious detail, we note that fast holes are broader than slow ones for large values of ψ_o, and vice versa for small values of ψ_o. The absolute agreement between the theoretical and the observed values of Δx_h for a given ψ_o is not exceedingly high, but this can, naturally be attributed to the simple theoretical model. However, the general trend is the same for the observed values of Δx_h and the theoretical estimates; thus, we see that the slope of the theoretical area fits nicely to the slope of the best straight line through the measured points.

The results presented in the last two sections indicate that the simple waterbag equilibrium model derived in Sec. 5.1 actually describes some of the fundamental features of the electron hole.

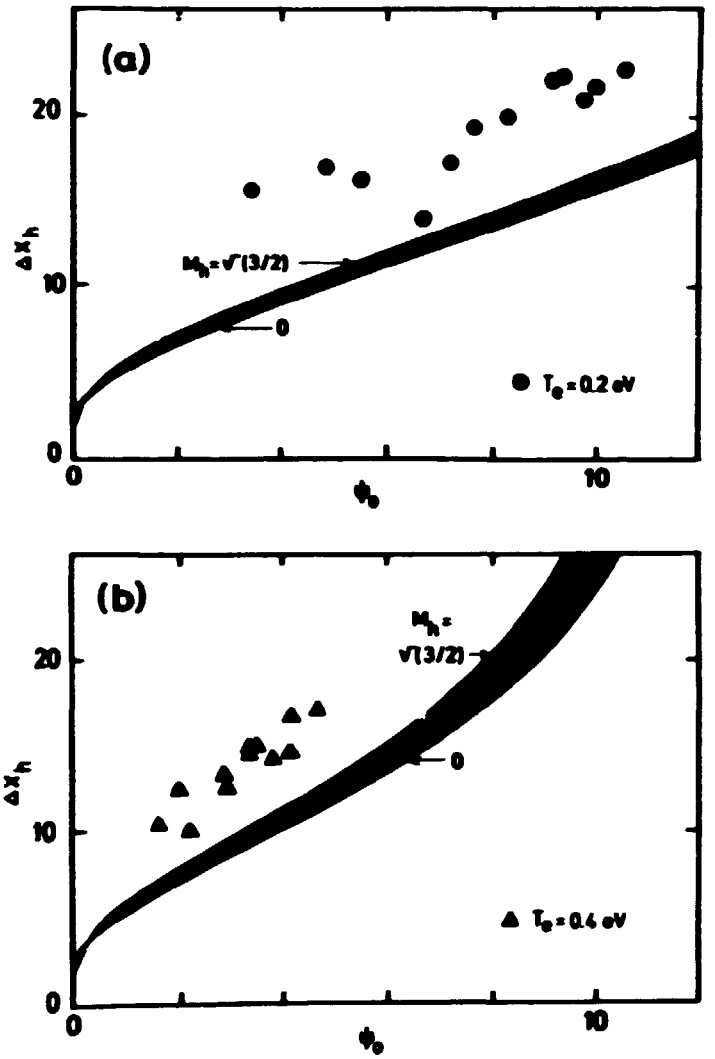

Fig. 33. Numerical simulation results for hole width Δx_h versus hole amplitude ψ_o for (a) T_e = 0.2 eV and (b) T_e = 0.4 eV.

6. INTERACTIONS BETWEEN THE SOLITARY WAVES

Up to this point, we have seen that the two different types of electron density pulses excited in the experiment and the numerical simulation are solitary waves. At least, they are solitary waves in the sense described in the introduction that they both are localized waves in which nonlinear effects are essential, and which propagate with an almost fixed velocity and with a shape that is almost unchanged.

Unfortunately, the mutual interaction between Trivelpiece-Gould solitons moving in the same direction was impossible to investigate in the experiment and the simulation. This was due to the approximately 0.2 C_o maximum soliton velocity difference (otherwise the solitons were strongly distorted, as mentioned in Sec. 4.3) and since the solitons had to have an initial separation larger than the sum of the soliton widths they could not pass each other within the limited length of the plasma column. Furthermore, the theoretical expressions for N_r in Sec. 4.1.3 explicitly require only one soliton, so that the direct numerical solution of the model equation (20) could not be used to investigate soliton collisions either.

We did, however, briefly investigate the head-on collision of Trivelpiece-Gould solitons moving in opposite directions in the laboratory system in the experiment and the numerical simulation (Lynov et al., 1979a), and we found that the solitons emerged from the collision without any noticeable change of shape. We note that this situation of solitons moving in opposite directions in the laboratory frame cannot be described by the KdV equation, which is inherently unidirectional, but, instead, the complete system of Boussinesq equations (Karpman et al., 1980) must be employed. It should be mentioned that collisions of KdV solitons in dispersive media with much simpler model equations than Eq. (20) have been investigated by Watanabe (1978). Watanabe found that a little dissipation did not destroy the ability

of the solitons to preserve their identity upon mutual collisions, even though the dissipation, naturally, perturbed the solitons.

A different effect of soliton-soliton interactions is the recurrence phenomenon of initially sinusoidal waves. This phenomenon, which also is known as the Fermi-Pasta-Ulam problem (Fermi, Pasta, Ulam, and Tsingou, 1955), was acutally the object of the initial soliton work by Zabusky and Kruskal (1965). We have also, investigated the recurrence of long wavelength Trivelpiece-Gould waves (Lynov, Rasmussen, and Thomsen, 1980b), partly by means of a plasma simulation code (Thomsen, 1980) based on the hybrid simulation model (Denavit, 1972), and partly by means of the direct numerical soliton method (Appendix C) applied to the unperturbed KdV equation. Our main result is that a state of perfect recurrence, i.e., the 100% return of the total wave energy to the initial, single Fourier-mode, hardly exists. However, since these recurrence investigations had nothing to do with the experiments that were actually performed in the laboratory, they are outside the scope of this report, and will not be further described here.

Instead we will turn our attention to the cases of interaction between a Trivelpiece-Gould soliton and a hole, and between two electron holes (Saeki et al., 1979; Lynov et al., 1979a,c, and 1980a). Since no detailed theory is available for these investigations, only a qualitative description will be given of the observations in the experiment and the simulation.

6.1. Experiment

By applying two pulses, ϕ_1 and ϕ_2, of appropriate size to the exciter, we were able to produce two pairs of pulses, each consisting of a soliton and a hole. If the time interval between ϕ_1 and ϕ_2 is not too large, the soliton, S_2, from the second pulse could catch up with the hole, H_1, from the first pulse within the length of the experiment. An example is shown in Fig. 34, and we

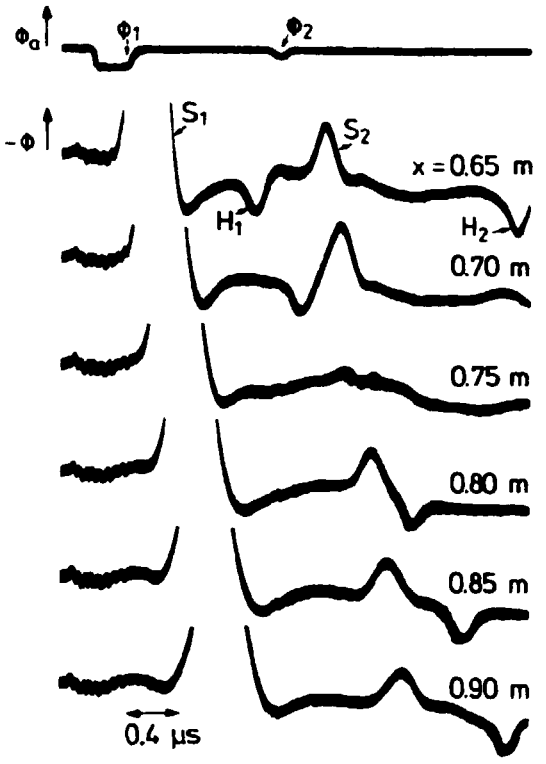

Fig. 34. Experimental results of soliton-hole collision.

see that S_2 passes right through H_1 causing only a phase jump, i.e., a time-limited, spatial displacement, of H_1.

The method of application of two pulses to the exciter cannot be used for investigations of hole-hole collisions, since the time interval between ϕ_1 and ϕ_2 must be large enough to allow the complete development of H_1. This implies that even with the largest possible velocity difference betwen H_1 and H_2, the two holes will never reach each other within the experimental region. Two holes with different velocities can, however, be excited by keeping the applied potenmtial at a small negative level after the pulse, as shown in Fig. 35. The two holes produced in this way have only a small velocity difference, but since they initially are located close to each other, they may collide after propagating a short distance. In the case shown in Fig. 35, collision takes place at x = 0.6 m (we recall that the exciter gap is located at x = 0.3 m, as shown in Fig. 1). Following the tra-

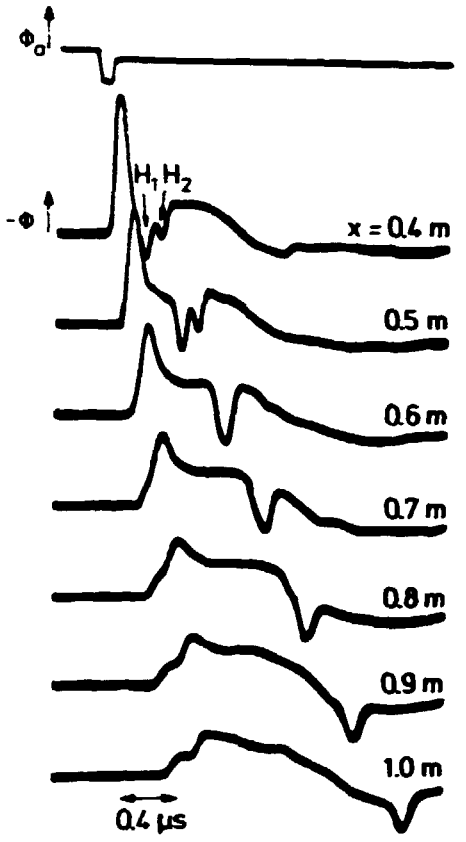

Fig. 35. Experimental results of hole-hole collision.

jectories of the holes, we observed an attraction and subsequently a coalescence of the holes that lasted throughout the transition of the entire plasma column (see Fig. 35). Since the two holes in this case do not emerge from the region of collision, they cannot be "solitons" in the sense of Scott, Chu and McLaughlin (1973), as described in Sec. 1. The coalescence of electron holes has already been observed in the previously mentioned, numerical simulations of the two-stream instability (e.g., Roberts et al., 1967; Morse et al., 1969a,b) and in the stability analysis of a train of BGK equilibrium by Schwarzmeier et al. (1979). More detailed investigations of the mutual interaction of the electron holes are presented in the following section.

6.2. Simulation

The necessity of a relatively large time delay between the two excitation pulses required to produce two completely independent electron holes, which was a problem in the experiment, was effectively avoided in the numerical simulation. This was accomplished by introducing two regions of excitation in the external potential, which could be operated at different positions and times with different potential jumps. In this way, it was possible to start the generation of a second set of solitary waves simultaneously, or shortly after, the application of the external field across the first exciter gap (located at a higher x-value than the second). This method was reliable as long as the distance between the regions of excitation was large enough to prevent the generation of the last solitary waves to be disturbed by the generation of the first. Once fully developed, the solitary waves from the second exciter propagated without any perceptible interaction through the rarefaction wave from the first exciter. By careful adjustment of the excitation mechanism, the electron holes from the second exciter could interact with the holes from the first within the length of the plasma column. However, since the solitons propagate with velocities that are, at least, four times larger than the hole velocities, we were not able to study the soliton-soliton interactions.

The values of the input parameters to the simulation in the examples in this section are comparable to their values in the experiment, i.e., $T_e = 0.2$ eV, $n_o = 10^7$ cm^{-3}, and $r_o = 2$ cm.

The interaction between a Trivelpiece-Gould soliton and an electron hole is shown in Fig. 36, in which the trajectories of the soliton and the hole are plotted in an (x-t) diagram. Figure 36a illustrates a case where the soliton amplitude is comparable to that of the hole. In this case only a small change in the trajectories of the two solitary waves is observed. If, however, the soliton amplitude is comparatively larger (as in Fig. 36b) we can observe a slight acceleration of the hole, while the soliton velocity is practically unchanged. Since the changes are relatively small even in this case, we may conclude that the in-

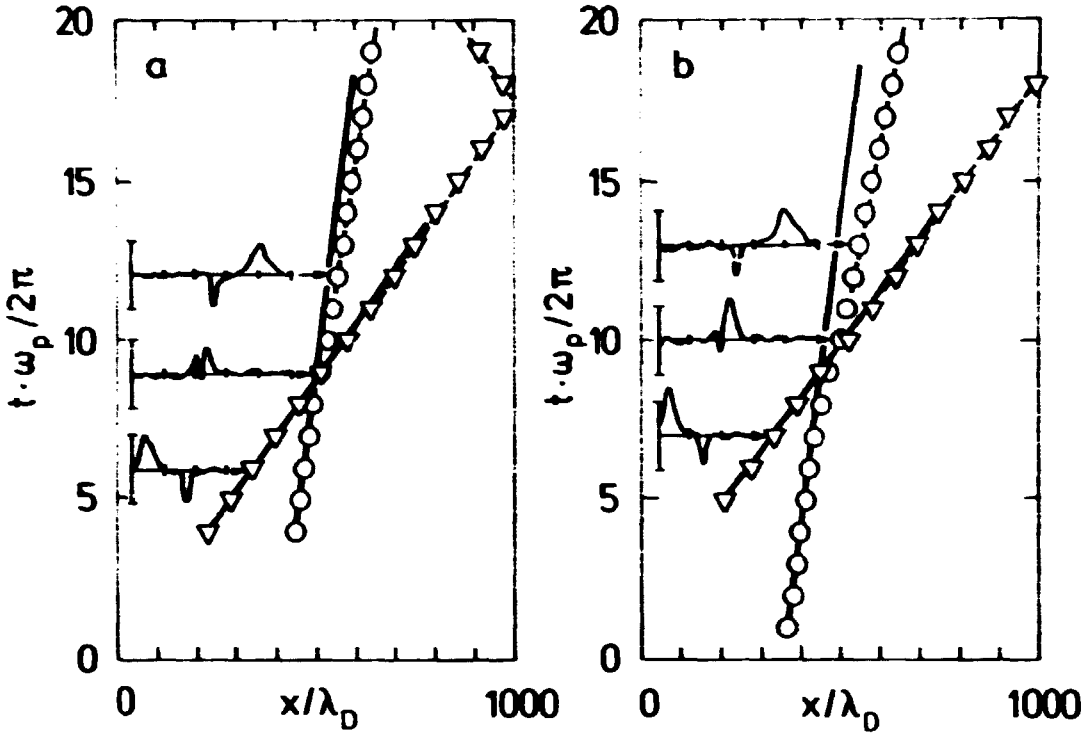

Fig. 36. (x-t)-diagram showing hole-soliton interactions for (a) comparable amplitudes and (b) large soliton. Inserts show typical potential variations (negative potentials are drawn upward, as usual) in the region $300 < x/\lambda_D < 800$. The marked ϕ-division is $(1/4)m(\omega_p a)^2/e$.

teraction between the electron hole and the Trivelpiece-Gould soliton is very weak. This result is probably caused by the much larger soliton velocity than hole velocity.

Some typical examples of hole-hole interactions are given in Figs. 37-39, which show the evolution in the phase space, the trajectory of the individual hole, and a few typical spatial potential variations associated with the holes. Since our excitation mechanism resulted in hole velocities (and hole amplitudes) that increased with increasing exciting potentials (see Figs. 30 and 32), we were able to choose the velocity difference between the two holes before running the simulation. Figure 37 shows the case of a relatively small velocity difference and, as

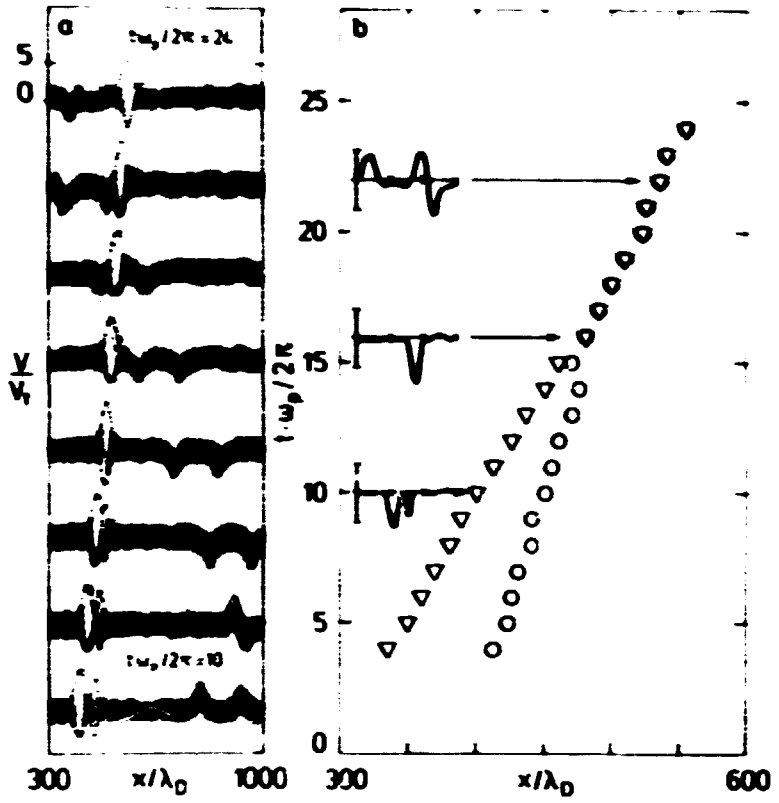

Fig. 37. Hole-hole coalescence, (a) phase space and (b) (x-t)-diagram, where inserts show typical spatial potential variations in the region $300 < x/\lambda_D < 600$. The ϕ-division is the same as in Fig. 36.

in the experiment (Fig. 35), the two holes coalesce. We note the violent rotational motion of the former individual holes in the phase space at the beginning of the coalescence, indicating a highly nonlinear process, and strongly resembling the evolution of a hole coalescence in the electron two-stream instability (see, e.g., Roberts et al., 1967).

If, on the other hand, the two holes have a large velocity difference, we obtain the result shown in Fig. 38, where the two holes pass through each other undergoing phase jumps only. Finally, if the hole velocity difference has a value somewhere between those shown in Figs. 37 and 38, we may obtain the case of "marginal" coalescence. This is shown in Fig. 39, and we see that the holes pass through each other at first, but then seem

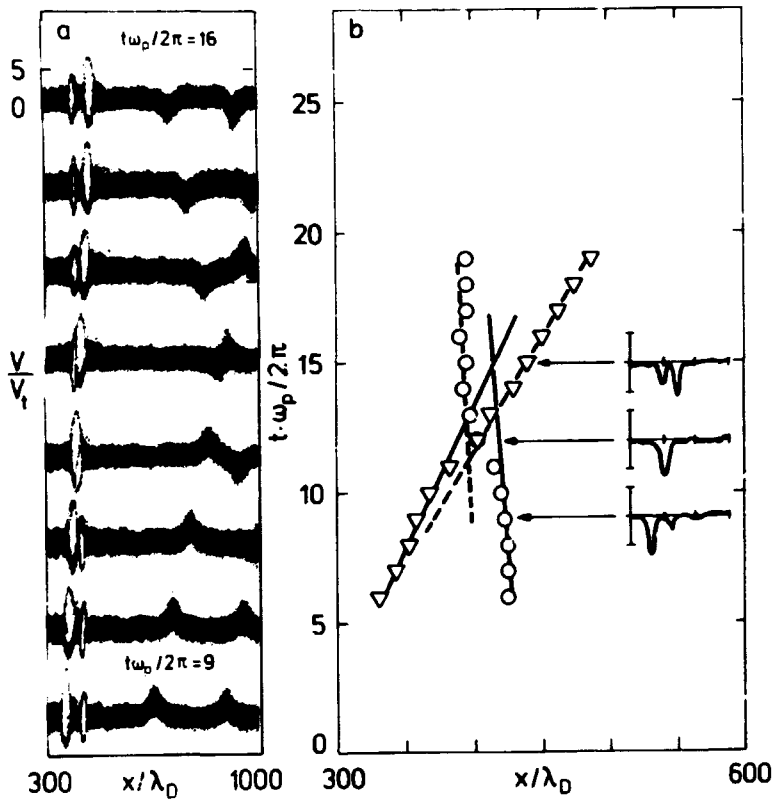

Fig. 38. Two holes passing through each other; (a) and (b) as in Fig. 37.

to "regret" that they did not coalesce, which they subsequently do.

In all three cases of hole-hole interaction (Figs. 37-39) we see that the two holes propagate completely independent of each other until their separation is relatively small, i.e., 20-50 λ_D. This observation clearly supports the concept of electrostatic shielding of the positive charge associated with the hole, which was derived in Sec. 5.1 based on the analysis of Berk et al. (1970). We can estimate the distance, δx_i, at which the hole-hole interaction begins. First, we note that the expression for k_{eff} in Eq. (62) can be even further simplified in the usual case of λ_D smaller than the waveguide radius:

$$(k_{eff})^{-1} \approx \sqrt{3}\,\lambda_D \,, \quad \text{for} \quad (\lambda_D/a)^2 << 1 \,. \tag{77}$$

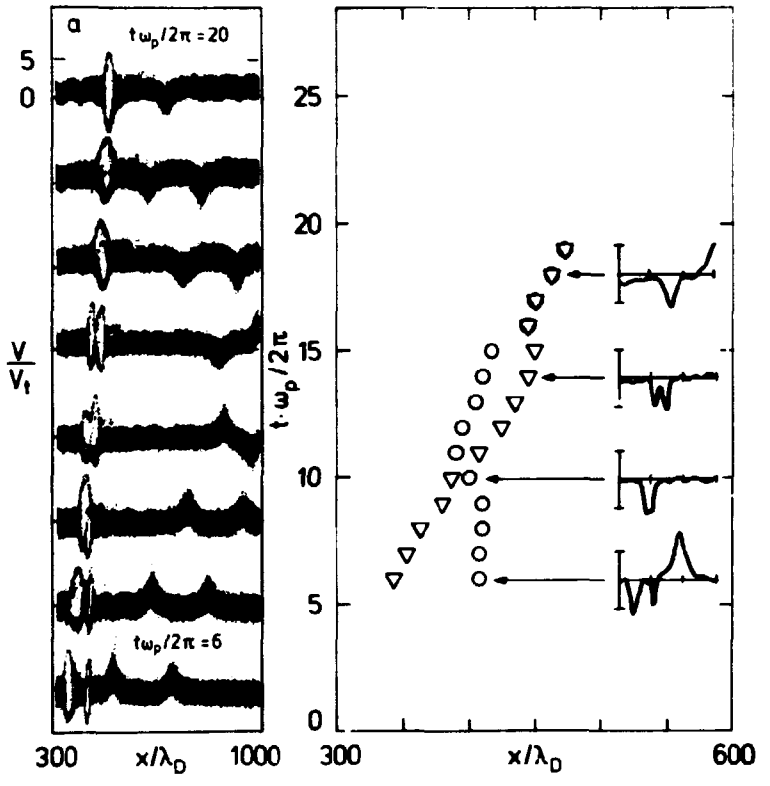

Fig. 39. "Marginal" coalescence of two holes; (a) and (b) as in Fig. 37.

This value of $(k_{eff})^{-1}$ is in fine agreement with the e-folding length of the hole potential found in Fig. 24 outside the region of v_2 and v_3. In Fig. 24 we also see that the hole potential falls from maximum to essentially zero (due to the exponential shielding) within a distance comparable to the total halfvalue width Δx_h of the hole. This means that the maximum distance of interaction

$$\Delta x_i \approx \Delta x_{h1} + \Delta x_{h2} \ , \tag{78}$$

where $\Delta x_{h1,2}$ are the values of Δx_h for the two holes, respectively. Using typical values for $\Delta x_{h1,2}$ from Fig. 33a, we find $\Delta x_i \sim 40\lambda_D$ in good agreement with the interaction distances seen in Figs. 37-39.

In order to estimate when two colliding electron holes coalesce or pass through each other, we can make the following rough picture: coalescence takes place if the time, t_i, during which the holes interact, is larger than the time, t_c, that is necessary for the two holes to complete the "mechanism of coalescence". It is fairly easy to estimate t_i, which we may equate with the time two holes of a total width Δx_t and with velocities v_1 and v_2 take to pass each other, i.e., $t_i = \Delta x_t/(v_2-v_1)$, where v_2 is chosen as the largest velocity. Let us now imagine that coalescence occurs when all the electrons trapped in the total potential of the two holes perform approximately a full closed orbit in phase space in order to "synchronize" their motion. Then t_c can be estimated as the reciprocal of the bounce frequency in this total hole, which appears during the interaction. Now, if we crudely assume that the potential of this resulting hole is proportional to the sum of the potentials of the individual hole, $\phi_{1,2}$, and that the width is proportional to Δx_t, we find that $t_c \propto \Delta x_t/(\phi_1 + \phi_2)^{\frac{1}{2}}$. The simple condition $t_i > t_c$ then yields

$$(\phi_2 + \phi_1)^{\frac{1}{2}} > \text{const}\cdot(v_2-v_1) \ , \quad \text{for coalescence.} \qquad (79)$$

In order to test this hypothesis we show, in Fig. 40, a diagram where the symbol • denotes coalescing holes and o holes passing through each other. The abscissa is $(\phi_2+\phi_1)^{\frac{1}{2}}$ and the ordinate (v_2-v_1). We see that the regions of coalescence/no coalescence, indeed are well separated by a straight line through the origin, thus confirming the criterion (79) and demonstrating that the important parameters are the hole amplitude and velocity. Actually, the cases of "marginal" coalescence (Fig. 39) are located very close to the dashed borderline.

In this section, we have seen that colliding electron holes either melt entirely together or preserve their original identity. Since we have also seen that a single electron hole is a stable structure (in a collisionless plasma) propagating with a fixed velocity and shape, it is natural to consider the solitary electron hole as a quasi-particle just like the soliton has been (see, e.g., Kaup and Newell, 1978). Doing this in a consistent way involves assigning to the solitary hole a positive charge and

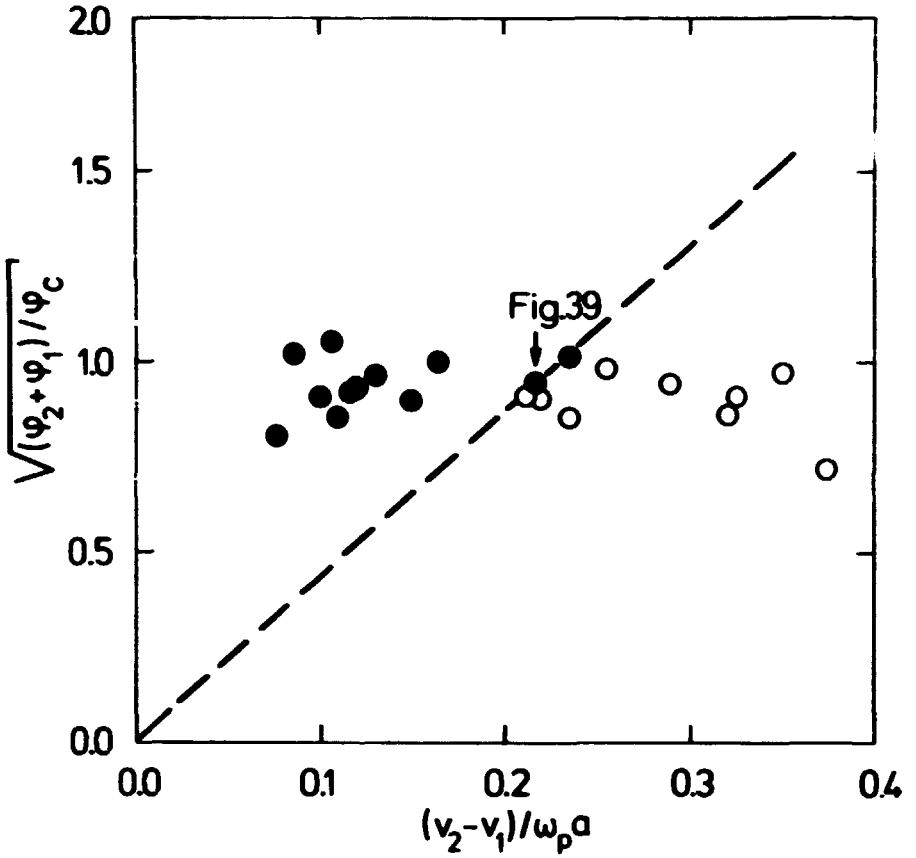

Fig. 40. Diagram for coalescence/no-coalescence of two holes. The symbol • denotes coalescing holes and o holes passing through each other. The point corresponding to Fig. 39 is marked with an arrow. $\phi_c = \frac{1}{2}m(\omega_p a)^2/e$.

a negative effective mass (see also the "Duality Principle" by Berk et al. (1970a). This in turn implies that the Coulomb interaction between two holes gives rise to an attraction, a feature that clearly has been seen in this section. To stay in the particle picture, these attractive forces, which are effective only in the nearest vicinity of the hole, may be characterized as "strong interactions".

7. CONCLUSION

In this work we have investigated the generation and propagation of two different types of electron density waves in an essentially one-dimensional system, i.e., a strongly magnetized, plasma-loaded waveguide. Both of the wavetypes demonstrated clear nonlinear behaviour, acting as almost complete solitary waves. However, they are basically of a completely different nature. In this way, the compressional wave, identified as a Trivelpiece-Gould soliton, is fundamentally a fluid phenomenon, while the electron hole is a purely kinetic phenomenon having no fluid counterpart.

After a short description of the experiment and the simulation code, and a brief introduction to the basic observations, in Sec. 4 we turned to a detailed investigation of kinetic effects of the resonant particles on the propagation of the Trivelpiece-Gould soliton. In Sec. 4.1, we showed how a perturbed KdV equation can be derived in order to model the soliton-particle interaction, and by use of the perturbation theory by Karpman and Maslov (1977, 1978) an analytical description of the soliton evolution was presented. As a result of the perturbation, the soliton was shown to either damp or grow, depending on the zeroth-order electron velocity distribution function, while generating a tail which consists of a plateau, nearest to the soliton, plus an oscillatory part. Explicit expressions for the soliton damping or growth, the height of the plateau, and the perturbed soliton velocity were given. It was also mentioned that the model equation could be used, in an almost unaltered form, for the description of the interaction between ion-acoustic solitons and resonant particles (Karpman, 1979b).

In Sec. 4.2, an investigation of the validity of the results from the perturbation analysis was performed by direct numerical integration of the model equation. The investigation showed that the analytical expressions from the perturbation analysis

are in close agreement with the actual development of the complete model equation, as long as the perturbing term is small enough to ensure that the theoretical region of validity was unexceeded. This validity region was, however, shown to be rather restrictive, so that most of the interesting situations from an experimental point of view would fall outside its limits. Although the agreement between the perturbation expressions and the actual behaviour of the model equation was somewhat smaller in the "experimentally interesting" cases, the analytical expressions for the soliton damping/growth and, to some extent, also the plateau height and soliton velocity were shown to be good estimates of their actual values found from the equation.

In the experiment (Sec. 4.3) and the simulation (Sec. 4.4) the "physical" soliton was demonstrated to develop in complete qualitative agreement with the perturbation results of Sec. 4.1. Furthermore, the quantitative soliton evolution in the simulation, which had better controlled "plasma" parameters than the experiment, was in very good agreement with the perturbation theory, the deviations going to the same side as the results, in Sec. 4.2, from the direct solution of the full model equation, e.g., the analytical underestimation of the actual plateau height. This fine description of the actual physical system by the perturbed KdV equation is far from being trivial, since we must bear in mind that the linear dispersion relation derived from a KdV equation gives only a poor approximation to the full dispersion relation (1) for short wavelengths. Even if the scale length of the initial perturbation was chosen large enough to allow an overall description by a KdV equation, one could, in principle, expect that the fine details of the soliton evolution could be influenced by this discrepancy at small wavelengths.

As for the electron hole, we have found (Sec. 5) that it can be described as a fully developed BGK equilibrium. By means of a simple waterbag model (Sec. 5.1) we showed that a single hole had a maximum velocity of the order of the electron thermal velocity and that, for a given waveguide radius, there existed a maximum permissible hole amplitude which, however, is not found in the infinite plasma. An expression was also found for the shape of

the hole as a function of hole amplitude, hole velocity, and the ratio r_o/λ_D; for typical parameters it was shown that the hole width increased with increasing hole amplitude.

The investigations of the electron hole in the experiment (Sec. 5.2) and the simulation (Sec. 5.3) showed that, due to the excitation mechanism, there existed a critical potential of the order of $\frac{1}{2}m(\omega_p a)^2/e$ which the applied, negative potential numerically had to exceed in order to produce a hole. Almost any shape of the applied potential was found to produce one or more electron holes as long as the critical potential was passed. The observations in the experiment and simulation of the single hole behaviour demonstrated that the simple waterbag model is useful as an approximate description of the solitary electron hole.

In Sec. 6 we investigated the interaction between a Trivelpiece-Gould soliton and an electron hole, and between two electron holes. The soliton-hole interaction was demonstrated to be weak. It should be mentioned that Saeki et al. (1979) showed that the interaction between an electron hole and an ion-acoustic soliton may be rather strong. In the case of a hole-hole collision, the electron hole demonstrated a quasi-particle behaviour, since the two holes either preserved their identity upon collision or coalesced completely. It was found empirically, and explained by simple arguments, that collisions between large amplitude holes with a small velocity difference favours the case of coalescence. It should be pointed out that the electron hole may play an important role in the description of strong, one-dimensional Langmuir turbulence (Dupree, 1978).

In conclusion, it may be emphasized that the results reported in the preceding pages have demonstrated that detailed experiments of even highly nonlinear plasma phenomena, which from the fusion-technology point of view are the most interesting, can be performed in a controlled manner in a relatively simple plasma device, such as the Q-machine, and by use of a simulation scheme based on fundamental plasma theory.

ACKNOWLEDGEMENTS

The author wishes to thank the Association EURATOM-Risø National Laboratory for the scholarship which has made the studies described in this report possible. I thank the entire Group of Fundamental Plasma Physics for their great help and patient support during my studies, and I am, also, in great debt to Professor V.I. Karpman, Dr. K. Saeki, and Dr. V.A. Turikov, who have made major contributions to the basis of my work.

REFERENCES

ANDERSEN, H.K. (1970). Fys. Tidskr. 68, 7-38.

BEREZIN, Yu.A. and KARPMAN, V.I. (1966). Zh. Eksp. Teor. Fiz. 51, 1557-1568 [1967, Sov. Phys.-JETP Engl. Transl. 24, 1049-1056].

BERK, H.L., NIELSEN, C.E., and ROBERTS, K.V. (1970a). Phys. Fluids 13. 980-995.

BERK, H.L. and ROBERTS, K.V. (1970b). In: Methods in Computational Physics 9. Plasma physics. Edited by B. Alder, S. Fernbach and M. Rotenberg (Academic Press, London) 78-134.

BERNSTEIN, I.B., GREEN, J.M., and KRUSKAL, M.D. (1957). Phys. Rev. 108, 546-550.

BIRDSALL, C.K. and FUSS, D. (1969). J. Comput. Phys. 3, 494-511.

DEPACKH, D.C. (1962). J. Electron. Control 13, 417-424 (as cited in Berk et al., 1970).

DENAVIT, J. (1972). J. Comput. Phys. 9, 75-98.

DUPREE, T.H. (1978). Bull. Am. Phys. Soc. 23, 869.

FAINBERG, Ya.B. (1961). At. Energ. 11, 313-335 [1962, Sov. J. At. Energy 11, 958-979] (as cited in Krivoruchko et al., 1974).

FERMI, E., PASTA, J., ULAM, S., and TSINGOU, M. (1955). Studies of Nonlinear Problems. I. LA-1940, 20 p.

FERNANDEZ, J.C., REINISCH, G., BONDESON, A., and WEILAND, J. (1978). Phys. Lett. 66A, 175-178.

FRANKLIN, R.N., HAMBERGER, S.M., LAMPIS, G. and SMITH, G.J. (1974). The Propagation og Small Amplitude Coherent Electron Plasma Waves in Q-Machine Plasma. Culham Laboratory Report, CLM-R 131, 39 p.

FRANKLIN, R.N., HAMBERGER, S.M., LAMPIS, G., and SMITH, G.J. (1975). Proc. R. Soc. London Ser. A 347, 25-46.

GARDNER, C.S., GREEN, J.M., KRUSKAL, M.D., and MIURA, R.M. (1967). Phys. Rev. Lett. 19, 1095-1097.

GAZDAG, J. (1976). J. Comput. Phys. 20, 196-207.

IKEZI, H., TAYLOR, R.J., and BAKER, D.R. (1970). Phys. Rev. Lett. 25. 11-14.

IKEZI, H., BARRET, P.J., WHITE, R.B., and WONG, A.Y. (1971). Phys. Fluids 14, 1997-2005.

IKEZI, H. (1973). Phys. Fluids 16, 1668-1675.

KAKO, M., TANIUTI, T., and WATANABE, T. (1971). J. Phys. Soc. Jon. 31, 1820-1829.

KARPMAN, V.I. (1975). Nonlinear Waves in Dispersive Media (Pergamon, Oxford) (International Series of Monographs in Natural Philosophy; 71) 186 p.

KARPMAN, V.I. (1979a). Physica Scr. 20, 462-478.

KARPMAN, V.I. (1979b). Zh. Eksp. Teor. Fiz. 77, 1382-1395 [1979, Sov. Phys.-JETP Engl. Transl. 50, 695-701].

KARPMAN, V.I., LYNOV, J.P., MICHELSEN, P., PECSELI, H.L., JUUL RASMUSEN, J., and TURIKOV, V.A. (1979). Phys. Rev. Lett. 43, 210-214.

KARPMAN, V.I., LYNOV, J.P., MICHELSEN, P., PECSELI, H.L., JUUL RASMUSSEN, J., and TURIKOV, V.A. (1980). Phys. Fluids 23, 1782-1794.

KARPMAN, V.I. and MASLOV, E.M. (1977). Zh. Eksp. Teor. Fiz. 73, 537-559 [1977, Sov. Phys.-JETP Engl. Trans. 46, 281-291].

KARPMAN, V.I. and MASLOV, E.M. (1978). Zh. Eksp. Teor. Fiz. 75, 504-517 [1979, Sov. Phys.-JETP Engl. Transl. 48, 252-259].

KATO, Y., TAJIRI, M., and TANIUTI, T. (1972). Phys. Fluids 15, 865-870.

KAUP, D.J. and NEWELL, A.C. (1978). Proc. R. Soc. Lond. A 361, 413-446.

KORTEWEG, D.J. and DE VRIES, G. (1895). Phil. Mag. 39, 422-443.

KO, K. and KUEHL, H.H. (1980). Phys. Fluids 23, 834-836.

KRAPCHEV, V.B. and RAM, A.K. (1980). Phys. Rev. A, in press.

KRIVORUCHKO, S.M., FAINBERG, Ya.B., SHAPIRO, V.D., and SHEVCHENKO, V.I. (1974). Zh. Eksp. Teor. Fiz. 67, 2092-2103 [1975, Sov. Phys.-JETP Engl. Transl. 40, 1039-1043].

LAVAL, G., PELLAT, R., and PERULLI, M. (1969). Plasma Phys. 11, 579-588.

LYNOV, J.P. (1980). Modification of KdV Solitons by Reflected Particles. In: Proceedings of International Conference on Plasma Physics 1, Nagoya, Japan, April 7-11, 1980 (Fusion Research Association of Japan) p. 400.

LYNOV, J.P., MICHELSEN, P., PÉCSELI, H.L., JUUL RASMUSSEN, J., SAÉKI, K., and TURIKOV, V.A. (1979a). Phys. Scr. 20, 328-335.

LYNOV, J.P., MICHELSEN, P., PÉCSELI, H.L., and JUUL RASMUSSEN, J. (1979b). Damping of solitons by reflected particles. Risø-M-2168, 18 pp.

LYNOV, J.P., MICHELSEN, P., PÉCSELI, H.L., and JUUL RASMUSSEN, J. (1979c), J. Phys. Colloq. C7, 1, 567-568.

LYNOV, J.P., MICHELSEN, P., PÉCSELI, H.L., and JUUL RASMUSSEN, J. (1980a). Phys. Lett. 80A, 23-25.

LYNOV, J.P., JUUL RASMUSSEN, J., and THOMSEN, K. (1980b). Recurrence of Long Wavelength Electron Plasma Waves. In: Proceedings of International Conference on Plasma Physics 1, Nagoya, Japan, April 7-11 1980 (Fusion Research Association of Japan) p. 401.

MAXON, S. and VIECELLI, J. (1974a). Phys. Rev. Lett. 32, 4-6.

MAXON, S. and VIECELLI, J. (1974b). Phys. Fluids 17, 1614-1616.

MORSE, R.L. and NIELSON, C.W. (1969a). Phys. Fluids 12, 2418-2425.

MORSE, R.L. and NIELSON, C.W. (1969b). Phys. Rev. Lett. 23, 1087-1090.

MOTLEY, R.W. (1975). Q-Machines (Academic Press, New York) 190 p.

OKUTSU, E., NAKAMURA, M., NAKAMURA, Y., and ITOH, T. (1978). Plasma Phys. 20, 561-568.

O'NIEL, T.M. and MALMBERG, J.H. (1968). Phys. Fluids 11, 1754-1760.

OSTROVSKY, L.A., PETRUKHINA, V.I., and FAINSHTEIN, S.M. (1975). Zh. Eksp. Teor. Fiz. 69, 2051-2055 [1976, Sov. Phys.-JETP Engl. Transl. 42, 1041-1043].

OTT, E. and SUDAN, R.N. (1969). Phys. Fluids 12, 2388-2394.

JUUL RASMUSSEN, J. (1977). Nonlinear electron plasma waves in a cylindrical waveguide. Risø-M-1911. 40 pp. and Finite amplitude electron plasma waves in a cylindrical waveguide. Plasma Phys. 20, 997-1010.

ROBERTS, K.V. and BERK, H.L. (1967). Phys. Rev. Lett. 19, 297-300.

SAEKI, K. (1973). J. Phys. Soc. Jpn. 35, 251-257.

SAEKI, K., IIZUKA, S., SATO, N., JUUL RASMUSSEN, J., and SEKIMOTO, S. (1979a). Annual Review 1978-1979, Institute of Plasma Physics, Nagoya, p. 126.

SAEKI, K., MICHELSEN, P., PECSELI, H.L., and JUUL RASMUSSEN, J. (1979b). Phys. Rev. Lett. 42, 501-504.

SAGDEEV, R.Z. (1963). Kollektivnye Protsessy i Ydarne Volny v Razrezhennoi Plasma (Institute of Nuclear Physics, Siberian Branch, Academy of Sciences, Novosibirsk, SSSR), 52 p. [1965, Coliective Processes and Shock Waves in Rarefied Plasma. AEC-tr-6509, 74 p.].

SAKANAKA, P.H., CHU, C.K., and MARSHALL, T.C. (1971). Phys. Fluids 14, 611-614.

SCHAMEL, H. (1979). Phys. Scr. 20, 336-342.

SCHWARZMEIER, J.L., LEWIS, H.R., ABRAHAM-SHRAUNER, B., and SYMON, K.R. (1979). Phys. Fluids 22, 1747-1760.

SCOTT, A.C., CHU, F.Y.F., and MCLAUGHLIN, D.W. (1973), Proc. IEEE 61, 1443-1483.

TANIUTI, T. (1974). Prog. Theor. Phys. Supl. 55, 191-211.

THOMSEN, K. (1980). Hybrid simulation af elektronbølger. Dissertation (M.Sc.), The Technical University of Denmark, Dept. for Electrophysics, 104 pp.

TRIVELPIECE, A.W. and GOULD, R.W. (1959). J. Appl. Phys. 30, 1784-1793.

TURIKOV, V.A. (1978a). A particle simulation code for analysis of nonlinear electron oscillations in a magnetized plasma waveguide. Risø-M-2116. 26 pp.

TURIKOV, V.A. (1978b). Computer simulation of the formation of Langmuir solitons and holes in a cylindrical magnetized plasma column. Risø-R-380. 28 pp.

VANDAM, J.W. and TANIUTI, T. (1973). J. Phys. Soc. Jpn. 35, 897-906.

VLIEGENHART, A.C. (1971). J. Eng. Math. 5, 137-155.

WASHIMI, H. and TANIUTI, T. (1966). Phys. Rev. Lett. 17, 996-998.

WATANABE, S. (1978). J. Phys. Soc. Jpn. 45, 276-282.

ZABUSKY, N.J. and KRUSKAL, M.D. (1965). Phys. Rev. Lett. 15, 240-243.

APPENDIX A

Temporal change of area, energy and soliton amplitude

By integrating the model equation (20) from $x = -\infty$ to $x = +\infty$ and assuming that $U = \partial^2 U/\partial x^2 = 0$ for $x = \pm\infty$, we find

$$\frac{\partial Q_1}{\partial t} = - C_o^3 \, N_1(x=+\infty)$$

or

$$Q_1(t') = Q_1(t=0) - C_o^3 \int_o^{t'} N_1(x=+\infty,t) \, dt \, , \qquad (A1)$$

where the area, $Q_1 = \int_{-\infty}^{\infty} U dx$. In a similar way, by multiplying both sides of (20) by U and integrating from $x = -\infty$ to $x = +\infty$ and assuming that $U = \partial U/\partial x = 0$ for $x = \pm\infty$, we obtain

$$\frac{\partial Q_2}{\partial t} = \frac{C_o^3}{2} \int_{-\infty}^{\infty} N_r(x) \frac{\partial U}{\partial x} \, dx \, ,$$

or

$$Q_2(t') = Q_2(t=0) + \frac{C_o^3}{2} \int_o^{t'} \int_{-\infty}^{\infty} N_r(x,t) \frac{\partial U}{\partial x} \, dx \, dt \, , \qquad (A2)$$

where the "energy" is defined by $Q_2 = \frac{1}{2} \int_{-\infty}^{\infty} U^2 dx$.

It should be stressed that the expressions (A1) and (A2) do not make any assumption on the form of U(x,t), besides the very unrestrictable boundary conditions for $x = \pm\infty$. This means that these expressions may serve as good checks of the accuracy of the program used for the direct numerical solution of (20) (see Sec. 4.2 and App. C). In the case of the numerical solution, the x-integration must run from $x = 0$ to L, and the boundary values $U = \partial U/\partial x = 0$ for $x = 0,L$ must be assumed, since the program does not automatically assure this (see App. C). How-

ever, for the parameters used in the examples in Sec. 4.2, the values of U and $\partial U/\partial x$ at x = 0,L are negligible. The x-integration of (A2) in the program is performed by Simpson's method, while the time integration is performed by the trapezoidal method.

Assuming the time-dependent soliton solution

$$U(x,t) = U_o(t)\,\mathrm{sech}^2[(x-x_o)/\delta(t)] \ ,$$

$$\delta(t) = 2C_o^2/\omega_p[U_o(t)]^{\frac{1}{2}} \ ,$$

direct insertion in the energy evolution expression (A2) results in exactly the same equation for the soliton growth rate as obtained by the inverse scattering method in Eq. (23) (where the evolution of $v(t) = [2U_o(t)/v_t^2]^{\frac{1}{2}}$ is expressed). This means that the energy loss from the soliton originating from the generation of the tail is not included in the perturbation scheme based on the inverse scattering method.

The soliton growth rate can also be derived from a simple physical model as described by Lynov, Michelsen, Pécseli, and Rasmussen (1979b). As a summary of this work, the total (kinetic plus potential) energy of a soliton, W_s, can be expressed by

$$W_s = \frac{8}{3}\varepsilon_o\, C_o\, \phi_o^{3/2}\, (m/\alpha e)^{\frac{1}{2}}/a \ , \qquad \text{(A3)}$$

where ϕ_o is the maximum amplitude of the negative potential of the soliton. Regarding the electrons, those with velocities, v, in the range $v_1 < v < v_2$ (where $v_1 = v_{ph} - (2e\phi_o/m)^{\frac{1}{2}}$ and $v_2 = v_{ph} + (2e\phi_o/m)^{\frac{1}{2}}$) are reflected by the soliton moving with velocity v_{ph}, and will thus receive, or give up, energy. The net energy gain by such electrons is $2mv_{ph}\cdot(v_{ph}-v)$ and their flux towards the soliton is $|v-v_{ph}|n_o f_o(v)dv$. This means that the electrons receive an amount of energy per unit time, dW_e/dt, given by

$$\frac{dW_e}{dt} = 2\, m\, v_{ph}\, n_o \int_{v_1}^{v_2} v - v_{ph}\, (v_{ph} - v)\, f_o(v)dv \ . \qquad (A4)$$

Energy conservation is maintained by equating $-dW_s/dt$ from (A3) to dW_e/dt from (A4), and it is readily verified that we obtain an expression for the soliton growth rate, $d\phi_o(t)/dt$, which is essentially the same as Eq. (23). Again it is seen that the assumption that the generation of the tail is negligible for the soliton damping is inherent in the perturbation analysis.

APPENDIX B

Single- and double-humped Maxwellian distribution functions

The case of the unperturbed velocity distribution function, $f_o(v)$, consisting of a main, non-drifting Maxwellian and a small, drifting Maxwellian called the beam, is expressed by

$$f_o(v) = \frac{n_o}{\sqrt{\pi}} \frac{1}{v_t} \left\{(1-\Delta n)\exp[-(v/v_t)^2] + \Delta n \Delta v_t \exp\left[-\left(\frac{v-v_{db}}{v_t}\right)^2 \Delta v_t^2\right]\right\} , \qquad (B1)$$

where $\Delta n = n_b/n_o$ and $\Delta v_t = v_t/v_{tb}$; n_b, v_{tb} and v_{db} are the density, thermal velocity and drift velocity of the beam, respectively. In order to make use of the theoretical results in Sec. 4.1, the requirement $\Delta n << 1$ must be fulfilled, so that the basic fluid behaviour is described in terms of the parameters of the main Maxwellian. Of course, the case of f_o consisting only of the main Maxwellian is described by putting $\Delta n = 0$. We mention that for the double-humped Maxwellian case used in this paper and listed in Table 1, the scaled beam thermal spread, $s = v_{tb}/v_{db}(2n_o/n_b)^{1/3}$, is 1.03, so that the second Maxwellian is rather a "beam" than a gentle "bump" (see O'Niel and Malmberg, 1968).

Inserting (B1) in Eq. (39) we obtain

$$N_1(\nu,\chi) = \frac{\nu}{\sqrt{\pi}} \sum_{i=1}^{2} n_i \int_0^{(1-\chi)^{\frac{1}{2}}} \left(\exp\left\{-[\mu_i - \nu_i(\omega^2+\chi)^{\frac{1}{2}}]^2\right\} - \exp\left\{-[\mu_i + \nu_i(\omega^2+\chi)^{\frac{1}{2}}]^2\right\}\right) d\omega \cdot \mathrm{sgn}(x-x_o) , \qquad (B2)$$

where $n_1 = (1-\Delta n)$, $n_2 = \Delta n \cdot \Delta v_t$, $\mu_1 = \mu = [2u_o/v_t^2]^{\frac{1}{2}}$, $\mu_2 = (\mu - v_{db})\Delta v_t$, $\nu_1 = \nu$, and $\nu_2 = \nu \cdot \Delta v_t$. For $1 << \mu << v_{tb}/v_t$ and $\nu >> 0$, we can neglect the first term under the integration

sign for i = 1 and the second term for i = 2. This has been done in all the numerical examples shown in this paper, where the relative total error by doing this in all cases was smaller than 10^{-3}.

Similarly, by inserting (B1) in Eq. (40), we obtain

$$N_2(\nu,\chi) = \frac{\nu}{\sqrt{\pi}} \sum_{i=1}^{2} n_i \int^{(1-\chi)^{\frac{1}{2}}} \left(\exp\left\{-[\mu_i - \nu_i(\omega^2+\chi)^{\frac{1}{2}}]^2\right\} + \exp\left\{-[\mu_i + \nu_i(\omega^2+\chi)^{\frac{1}{2}}]^2\right\}\right) d\omega + \frac{1}{2} \sum_{j=1}^{2} n_j \left\{ \mathrm{erf}[\mu_j - \nu_j(1-\chi)^{\frac{1}{2}}] - \mathrm{erf}[\mu_j + \nu_j(1-\chi)^2] \right\}, \quad (B3)$$

where all quantities $\sigma_j = \sigma_i$, except $n_{j=2} = \Delta n$. The considerations on the magnitudes of the terms under the integration sign are, of course, the same for (B3) as for (B2).

By use of(B2) we can express the soliton growth rate (42) as

$$\frac{d\nu}{dt} = \frac{\omega_p}{\sqrt{\pi}} \frac{C_o}{v_t} \sum_{i=2}^{2} n_i \frac{1}{\nu_i} \left\{ G(\mu_i+\nu_i) + G(\mu_i-\nu_i) - 2G(\mu_i) \right\} , \quad (B4)$$

where the quantities σ_i are the same as in (B2) and the function

$$G(y) = \exp(-y^2)\cdot(\mu - \tfrac{1}{2}y) + \frac{\sqrt{\pi}}{2}\mathrm{erf}(y)\cdot(\tfrac{1}{2} + \mu^2) . \quad (B5)$$

It can be seen from (B4) that $d\nu/dt$ is an explicit function of ν and not t, so instead of calculating $\nu(t)$ one can calculate "$t(\nu)$" straightforwardly. In doing so, one should remember that $\mu = \mu(\nu)$ (see (38)).

Insertion of (B2) in (43) yields

$$\frac{U_-}{U_o} = 4\left(\frac{C_o}{v_t}\right)^4 \sum_{j=1}^{2} n_j \left\{ \mathrm{erf}(\mu_j+\nu_j)+\mathrm{erf}(\mu_j-\nu_j)-2\mathrm{erf}(\mu_j) - \right.$$

$$\left. \frac{4}{\sqrt{\pi}} \frac{1}{\nu_j^2} \left[G(\mu_j+\nu_j)+G(\mu_j-\nu_j)-2G(\mu_j) \right] \right\} , \qquad \text{(B6)}$$

where all σ_j have the same meaning as in (B3). In the numerical solution of (B3)-(B6) it is beneficial to calculate the value of the error function, erf(y), as 1-erfc(y), since y usually is larger than 2 in our calculations and the numerical algorithm for calculating the complementary error function, erfc(y), is far more accurate than the algorithm for erf(y) for these large y-values.

APPENDIX C

Numerical methods for solution of the model equation

In this appendix a description will be given of the numerical methods employed by the program SOLITAIL in order to solve the model equation (20) for the modification of Trivelpiece-Gould solitons by resonant particles, and in order to compare these direct solutions with those of the perturbation analysis in Sec. 4.1. No detailed description of the entire program will be given, but the notation throughout this appendix will be the same as in SOLITAIL, so it should be fairly easy to read and understand the program, which is written in ALGOL.

The first step in order to put the model equation on the computer is to write the equation in dimensionless variables, which are

$$X = \xi/a^2 \ , \quad T = \omega_p t \ , \quad U = U/(\omega_p a)^2 \ ,$$
$$B = \omega_p a/v_t \ , \quad A = C_o/\omega_p a = (1+3/(2B^2))^{\frac{1}{2}} \ . \tag{C1}$$

Then, equation (20) in the ξ-reference system (see (49)) becomes

$$\frac{\partial U}{\partial T} + \frac{3}{2A}\left[U - \frac{U\emptyset}{3} \right]\frac{\partial U}{\partial x} + \frac{A^3}{2}\frac{\partial^3 U}{\partial X^3} = -\frac{A^3}{2}\frac{\partial NR}{\partial x} \ , \tag{C2}$$

where $U\emptyset = U_o(0)/(\omega_p a)^2$ is the soliton amplitude and $NR = N_r$.

The next step for the numerical solution of (20) is to introduce finite boundaries on X and T and to discretize the variables inside these boundaries. In this way, we put

$$0 \leq X \leq XMAX \ (= L/a) \ , \quad 0 \leq T \leq TMAX \ ,$$
$$h = XMAX/M \ , \quad k = TMAX/N \ , \tag{C3}$$

where M and N are integers. We then choose to approximate (C2) by the explicit, time-centered, finite-difference equation

$$U_i^{j+1} = U_i^{j-1} + (D\cdot(U_{i-1}^j + U_i^j + U_{i+1}^j) + E)\cdot(U_{i+1}^j - U_{i-1}^j) +$$

$$F\cdot(U_{i+2}^j - 2U_{i+1}^j + 2U_{i-1}^j - U_{i-2}^j) +$$

$$G\cdot(NR_{i+1}^j - NR_{i-1}^j) , \quad 0 \leq i \leq M, \ 1 \leq j \leq N \qquad (C4)$$

where $U_i^j = U(ih, jk) = U(X,T)$, $D = -k/2A$, $E = kU0/2hA$, $F = -kA^3/2h^3$, and $G = -kA^3/2h$. U_i^1 is found by performing an uncentered Euler step from U_i^0 to $U_i^{\frac{1}{2}}$ followed by a step equivalent to (C4) centered in $U_i^{\frac{1}{2}}$ and with a time step equal to k/2.

The difference scheme (C4) has a truncation error of the order $O(k^3) + O(k\cdot h^2)$, and is equivalent to the scheme used by Zabusky and Kruskal (1965) for investigations of the unperturbed KdV equation. Vliegenhart (1971) has performed a linear stability analysis of the Zabusky-Kruskal scheme, and translating his results, so that they apply to the unperturbed KdV equation corresponding to (C2), we find the stability condition

$$\frac{k}{h}\left(\frac{1}{A}U0 + 2A\frac{1}{h^2}\right) < 1 . \qquad (C5)$$

Test runs with SOLITAIL have shown that (C5) is very close to the stability condition for the total equation (C4) as long as $U0 < 0.3$ and $B = \omega_p a/v_t > 3.6$.

We have tried another differencing scheme which in principle should be better than (C4), namely, the "Partially Corrected Second-order Adams-Bashford Scheme" (PCABS) described by Gazdag (1976). However, the most difficult part of performing a numerical solution of (C2) is to find NR(X,T) (corresponding to NR_i^j in the finite difference scheme) so most of the CPU-time (i.e., the Central Processor Unit time which is almost proportional to the price of the computer job) is used to calculate NR_i^j. Since it is necessary to calculate the "fully corrected" value of NR_i^j in order to perform the accuracy checks of Q_1 and Q_2 (see App. A), the PCABS took about twice the CPU-time of (C4) for the same

h and k. Gazdag (1976) showed that a smaller differencing error is obtained by using half the time step k in the usual time-centered (or leap-frog) scheme than by using the PCABS, and since the first alternative is not more time consuming in our case than the second, we chose to continue with the scheme (C4). It should, however, be stressed that for problems that are "less nonlinear" than (C2) the PCABS improves the differencing accuracy appreciably while only slightly increasing the CPU-time as compared to the leap-frog method.

In order to calculate NR_1^j it is first necessary to find the soliton maximum, $UMAX^j$, and the position of this maximum, $MAXPOS^j$. It turned out that the numerical solution was very sensitive to the accuracy of the determination of $UMAX^j$ and $MAXPOS^j$ which is not surprising since N_1 and N_2 depend strongly on $v = 3(2UMAX^j)^{\frac{1}{2}}$ (see Fig. 9) and since N_1 changes sign at $X = MAXPOS^j \cdot h$. By introducing the equivalent of the initial soliton width, $XFIT = 2A^2/(U0)^{\frac{1}{2}}h$, $MAXPOS^j$ is found as the area-weighted centre of U_i^j from $i = MAXPOS^{j-1} - XFIT$ to $MAXPOS^{j-1} + XFIT$. $UMAX^j$ is determined from the best-fitted parabola for $i = MAXPOS^j - XFIT/3$ to $MAXPOS^j + XFIT/3$. The maximum of U determined in this way is within 0.1% of the real U0 if $U(X) = U0\ \mathrm{sech}^2((x-x_0)/\delta)$. The difference between the best-fitted parabola and the pure sech^2-form increases if the interval of the fitted point is increased, while the uncertainty of the determination increases for the case of a "noisy" sech^2 if the interval of points is decreased. In the examples in Sec. 4.2 XFIT was close to 10.

Even though this procedure for finding $MAXPOS^j$ and $UMAX^j$ is very accurate, test runs of SOLITAIL in some cases were numerically unstable, due to a sudden growth of oscillations in UMAX(T) with a frequency corresponding to a half-period equal to k. This instability was effectively quenched by assigning to $UMAX^j$ and $MAXPOS^j$ the mean value of their estimated size described above and their size at the previous time step. This smoothing has a negligible effect on the "true" solution since the value of k is always very much smaller than the characteristic time scale τ_s.

Once $UMAX^j$ and $MAXPOS^j$ are determined, it is a straightforward task to calculate NR_i^j from equation (B1) and (B2). However, these calculations are rather time consuming and since we must determine both N_1 and N_2 in all the M·N grid points (typical numbers are of the order of 1 Million) we make use of tables of $N_1(v,\chi)$ and $N_2(v,\chi)$ calculated at the beginning of the program instead of solving (B1) and (B2) at each grid point. These tables typically consist of 200 χ-points from 0 to 1, and 80 v-points from v_{min} to v_{max}. The values of v_{min} and v_{max} have to be estimated before running SOLITAIL, and for this purpose a program for the calculation of the theoretical v(T) by integration of Eq. (84) is written for our H.P 9825A desk calculator. The tables of N_1 and N_2 are used by linearly interpolating the values at the four nearest table points to the actual point (v^j,χ_i^j). These table interpolations gave good results for $0 \leq \chi < .9$ since $N_1(v,\chi)$ and $N_2(v,\chi)$ do not change rapidly in this region (see Fig. 9), but for $\chi > 0.9$, the table procedure is not sufficiently accurate, so for the relatively few grid points (i,j) with $\chi_i^j > 0.9$ direct solution of (B1) and (B2) is performed. Since the finite difference scheme (C4) involves the points from i-2 to i+2 for the determination of U_i^{j+1} in the range i = 0 to M, it is necessary to prescribe boundary conditions at i = 0 and M that can be used to determine U_i^j at i = -2,-1,M+1, and M+2. We have tested the following conditions at i = 0 and M: 1) $U = \partial U/\partial X = 0$, 2) $\partial U/\partial X = \partial^2 U/\partial X^2 = 0$, 3) $\partial U/\partial X = \partial^3 U/\partial X^3 = 0$, and 4) $\partial^2 U/\partial^2 X = \partial^3 U/\partial X^3 = 0$. Of these conditions Number 4 proved the best since the other alternatives caused generation of noise originating at the boundaries and propagating inwards.

Now, the procedure for advancing the solution one time step is to apply (C4) for the determination of U_i^{j+1} for i = 0 to M, then to apply the boundary conditions and, finally, to determine NR_i^{j+1} for i = -2 to M+2. Before a new time step is taken, we make use of the new values of NR_i^{j+1} to calculate the theoretical area and "energy" of U_i^{j+1} by use of Eqs. (A1) and (A2), and to calculate the theoretical soliton velocity by use of the actual $UMAX^{j+1}$ and NR_i^{j+1} in Eq. (25). Also, the upper and lower values of U_-/U_0 are found by searching the predicted plateau region, which has a lower limit corresponding to a point moving

with the linear phase velocity (see the dashed line in the figures of U(X,T) in Sec. 4.2) and originating at the middle of U(X,T = 0), and an upper limit corresponding to the position where a soliton, located at $MAXPOS^{j+1}$, would have the value of $\frac{1}{2}UMAX^{j+1}$ on the trailing edge. U_- is then found as the difference between this imaginary soliton and the actual value of U_1^{j+1}.

After performing the N time steps SOLITAIL calculates the theoretical values of $v(T)$ and $U_-/U_0(T)$ by use of the equations in App. B. An empirical formula for the approximate CPU-time on the Rise B6700 computer of SOLITAIL is $N \cdot M \cdot 2 \cdot 10^{-3} + NNY \cdot NCHI \cdot 5 \cdot 10^{-2}$ sec, where NNY is the number of v-values and NCHI is the number of χ-values in the tables of N_1 and N_2. In this way, a typical CPU-time is of the order of 5 hours.

Sales distributors:
Jul. Gjellerup, Sølvgade 87,
DK-1307 Copenhagen K, Denmark

Available on exchange from:
Risø Library, Risø National Laboratory,
P. O. Box 49, DK-4000 Roskilde, Denmark

ISBN 87-550-0733-3
ISSN 0106-2840